ABSTRACT

Title of Document: DEVELOPMENT OF ELECTRONIC DNA HYBRIDIZATION DETECTION USING CARBON NANOTUBE FIELD EFFECT TRANSISTOR ARRAYS

Herman Pandana, PhD., 2007

Directed By: Professor Romel D. Gomez, Department of Electrical and Computer Engineering

Spurred by the Human Genome Project, deoxyribonucleic acid (DNA) microarrays are indispensable tools in molecular biology. In particular, they are used in the genetic profiling of human diseases, which includes identifying genes that are expressed in certain cancers. Genotyping allows more accurate identification and consequently, improved treatment. This technique has the potential to revolutionize the diagnosis of many other human ailments and be an important tool in the arsenal of modern medicine. At present however, microarray experiments involve complex protocols, often employing fluorescent labeling as well as sophisticated detection instruments. These systems are thus only affordable by very few large laboratories and pharmaceutical companies. In this work, we propose and demonstrate the feasibility of using a low-cost and improved alternative. We designed and fabricated biochips based on carbon nanotube field effect transistor arrays to detect the presence of specific DNA sequences, e.g. expressed genes, in a solution of DNA or RNA in the

same manner as microarrays. The ultimate goal is to optimize the system to make it suitable for point-of-care applications. Our design utilizes CVD-grown carbon nanotube mats on a substrate of silicon oxide and metal contacts patterned using conventional microlithography. The carbon nanotube mats are covered by a thin oxide upon which single stranded DNA 'probe' molecules are immobilized. When exposed to a solution containing the complementary sequence, Watson-Crick hybridization leads to the binding of the complementary 'target' strands. Since DNA's are electrically charged through the excess electron of the phosphate backbone, this process results in the incorporation of additional negative charges at the transistor gate. This effectively causes a change in the conductance of the nanotube channel and a shift in the device threshold voltage. The voltage shift reflects the amount of extra charges deposited on the gate and based on this, the amount of captured target DNA can be precisely quantified.

We demonstrated electronic label-free detection of specific DNA binding or hybridization at the sensitivity level of 10−100 nM, and specificity limited by chemical protocols. Comparing other label-free schemes, we believe our approach is advantageous in terms of simplicity and compatibility with current microarray protocols.

DEVELOPMENT OF ELECTRONIC DNA HYBRIDIZATION DETECTION USING CARBON NANOTUBE FIELD EFFECT TRANSISTOR ARRAYS

By

Herman Pandana

Dissertation submitted to the Faculty of the Graduate School of the
University of Maryland, College Park, in partial fulfillment
of the requirements for the degree of
Doctor of Philosophy
2007

Advisory Committee:
Professor Romel D. Gomez, Chair
Professor Christopher C. Davis
Professor Robert W. Newcomb
Professor Neil Goldsman
Associate Professor Michael S. Fuhrer

Dedication

To

my mom, Suzy

and dad, Anwar Pandana

for the love and support

Acknowledgements

First I am very grateful to my advisor, Prof. Gomez, for his guidance and support during my study at the University of Maryland. He has always been very helpful in solving technical difficulties I encountered in completing my projects, and also very supportive in advising me even on personal issues. My graduate study experience would not have been as wonderful without him. His inspiring and motivating encouragements as well as constructive criticism are vital to my professional and personal development.

I would also like to thank the dissertation committee members Prof. Davis, Prof. Newcomb, Prof. Goldsman, and Prof. Fuhrer for their time and effort to evaluate and improve my dissertation.

I am very fortunate to have the opportunity to work with many amazing people at the Laboratory for Physical Sciences. Special thanks go to Dr. Michael Dreyer, Dr. Charles Krafft, and Dr. D.B. Romero for their support and advice. I am also indebted to my colleague Konrad H. Aschenbach, with whom I worked closely, Jookyung Lee, and Daniel R. Lenski in Physics department who provided carbon nanotube samples, Kristine-Ann Buela for teaching me molecular biology, and also my former group members Dr. Hyuncheol Koo, Dr. Seokhwan Chung, Dr. Li Gan, Dr. Sylvia Florez, and Marcia Golub. I would also like to extend my gratitude to the technical staffs of the Laboratory for Physical Sciences Toby Olver, Russell Fritzell, Lisa Lucas, Steve Brown, Leslie Lorenz, and J. B. Dottelis.

Finally I would like to thank my brother, Charles, and friends that have accompanied my stay in Maryland.

Table of Contents

Dedication ii
Acknowledgements iii
Table of Contents v
List of Tables vii
List of Figures viii
Chapter 1: Introduction 1
Chapter 2: Bioassays at the molecular level 5
2.1. A brief history on the study of genes [1] 5
2.2. Fractionation of cell components 8
2.2.1. Electrophoresis 9
2.2.2. Chromatography 10
2.3. Recombinant nucleic acid techniques [2] 12
2.3.1. Nucleic acid hybridization 13
2.3.2. Blotting 15
2.3.3. Sample multiplication: polymerase chain reaction 16
2.4. Gene identification and gene expression: Microarray 18
Chapter 3: Comparison of current available DNA detection schemes 22
3.1. Direct and sandwich assay 22
3.2. Labeled technique (1): Fluorescent detection 24
3.3. Labeled technique (2): Electrochemical detection 26
3.3.1. Randles equivalent circuit in electrochemical modeling 26
3.3.2. Measurement techniques and detection schemes 29
3.4. Label-free direct assays 32
3.5. Label-free (1): dielectric constant 33
3.5.1. Refractive index measurement: Surface plasmon resonance 33
3.5.2. Refractive index and thickness: Ellipsometry 40
3.5.3. Vibrational mode resonance: THz-transmission analysis 40
3.5.4. Dielectric constant: Capacitance measurement 41
3.6. Label-free (2): gravimetric 42
3.7. Label-free (3): field-effect 44
3.8. Summary of comparisons 48
Chapter 4: Carbon nanotube basics 50
4.1. Structure of a graphene sheet 50
4.2. Electronic properties of carbon nanotube 56
4.3. Synthesis and growth 58
4.4. Carbon nanotube as field effect transistors 59
Chapter 5: Electronic detection of DNA hybridization using carbon nanotube field effect transsistors 64
5.1. Device fabrication 65
5.1.1. Step 1: Bonding pad alignment marks 65
5.1.2. Step 2: Unwanted CNT removal 67
5.1.3. Step 3: Actual metal electrodes patterning 68

5.1.4. Step 4: Al_2O_3 atomic layer deposition 69
5.1.5. Step 5: Bonding pad oxide etch and gold film build-up 70
5.2. Theory 72
5.2.1. Electrode-electrolyte interface 72
5.2.2. Voltage shift upon hybridization 78
5.3. Measurements 81
5.4. DNA attachment chemistry 83
5.5. Results 88
5.6. Analyses and discussions 94
5.6.1. Effective field effect mobility 94
5.6.2. Scanning gate microscopy 95
5.6.3. Measurement: datapoint acquisition 96
5.6.4. Gate dielectric consideration 97
5.6.5. DNA surface coverage 98
5.7. Future work 99
Chapter 6: Other works on biosensors: gold nanoparticle colorimetry 101
6.1. Experiments 103
6.2. Results 105
6.2.1. Mechanism of resonance extinction 107
6.2.2. Number of binding sites on thrombin for the specific aptamer 109
6.2.3. Secondary structure of BOCK aptamer 110
6.2.4. Thrombin titration 114
6.3. Conclusions and future work 116
Chapter 7: Main conclusions 118
List of Publications 120
Bibliography 121

List of Tables

Table 1 Sensitivity comparison among field effect devices for biosensing application. 47
Table 2 Comparison among available label-free techniques. 49
Table 3 DNA oligonucleotide names and sequences. All oligonucleotides were ordered from Integrated DNA Technology, Inc. 86
Table 4 Summary of all of the chemical protocols encountered in the experiment. . 87
Table 5 Oligonucleotide names and sequences. The underlined base is one base mistake away from otherwise correct BOCK sequence. 104

List of Figures

Figure 1 An example of agarose gel electrophoresis. The left lane is DNA ladder serving as size calibrator. Smaller DNA travels further down the lane. The other four lanes are various samples that are being fragmented. (Source: wikipedia.org)..... 10

Figure 2 Atomic force microscope (AFM) image of linearized plasmid DNA (pGem7zft) on mica surface. The color map on the right indicates the height. (Data taken on Feb 2005, H. Pandana) 12

Figure 3 Denaturation curve of 15-mer DNA oligonucleotides (5'-AAT ATT GAT AAG GAT-3') hybridized in 10 mM PBS ph 7, 0.3 M NaCl buffer. As temperature is raised, the absorbance at 260 nm increases, contributed by denatured or separated DNA bases. The melting temperature T_m at 38.6 °C is indicated in the plot as the temperature at which 50% of the DNA is denatured. (Data taken on August 2005, H Pandana, D. B. Romero) 14

Figure 4 Schematics of blotting apparatus. As the buffer wicks up the sponge to the paper towel stack, it brings the DNA/RNA/protein in the gel to the nitrocellulose membrane..... 16

Figure 5 PCR steps: (1a) Start of cycle 1. Primers are chosen to multiply the DNA sequence in the flanked area. (1b) Denaturation step of cycle 1 to denature the double stranded DNA, each strand will serve as a template in the polymeration step. (1c) Primers hybridization. (1d) DNA synthesis activated by DNA polymerase. Monomers extend each primer to form two new daughter strands. (2) Repeat of the thermal cycling in cycle 2 yields 2^2 DNA. (2) Repeat of the thermal cycling in cycle 3 yields 2^3 DNA. One can recognize immediately the PCR cycles yield multiplication of the flank only. 17

Figure 6 Affymetrix uses a unique combination of photolithography and combinatorial chemistry to manufacture GeneChip® Arrays. (source: www.affymetrix.com) 21

Figure 7 Comparison of direct assay and sandwich assay 23

Figure 8 Randles equivalent circuit to model electrode-electrolyte interface. 28

Figure 9 A Bode plot of the Randles equivalent circuit..... 28

Figure 10 A Nyquist plot of the Randles equivalent circuit, showing both regimes of reaction limited at high frequency and mass transfer limited at low frequency. 29

Figure 11 Nyquist plot of a polypyrrole-DNA films after hybridization with its complementary target: 0 μM (+), 0.5 μM (□), 2μM (○), 3.5 μM (∇), 5.5 μM (◊). Reprinted from [19].Copyright (2005) Elsevier. 31

Figure 12 Dispersion relations of radiative plasmon wave and surface plasmon wave, also shown in dash are the light line in air and in glass prism medium having refractive index of $\sqrt{\varepsilon_1}$..... 36

Figure 13 SPW excitation configuration: Kretschmann (left) and Otto (right) configurations. 38

Figure 14 Illustration of electric field enhancement in 1D channel transistor as opposed to 2D planar transistor. The electric field is represented by the density of the field lines, shown in blue arrows. 46

Figure 15 Illustration of sp^2 orbitals in the carbon bonds of graphene sheets. 51

Figure 16 Hexagonal lattice structure of the carbon atoms in a graphene sheet. The Bravais unit cell is shown in a dashed rectangular box, which contains two atoms. The lattice points circled in blue show the periodicity of the unit cells. The primitive vectors are: $\hat{a}_1 = 3a_0/2\hat{x} + \sqrt{3}a_0/2\hat{y}$, and $\hat{a}_1 = 3a_0/2\hat{x} - \sqrt{3}a_0/2\hat{y}$ 52

Figure 17 (left) Contour plot of the band structure in the reciprocal space. The area within the dashed hexagonal is the first Brillouin zone. $\hat{A}_1$ and $\hat{A}_2$ are the primitive vectors in the reciprocal lattice. (right) Tightbinding band structure of a graphene sheet. The two groups of six wavevector, at which the conduction and valence bands coincide are shown in green and purple boxes, with respective colors marked on the left figure as well. 55

Figure 18 Scanning electron micrograph of the resulting carbon nanotube mats grown by catalytic chemical vapor deposition..... 58

Figure 19 Back-gated transfer characteristic of Al_2O_3 passivated CNTFET (V_{DS} = 0.1 V). Two salient features are ambipolar characteristic, and much smaller hysteresis, compared to unprotected CNTFET characteristic..... 61

Figure 20 I_{DS}-V_{DS} characteristic of unprotected CNTFET for various back-gated voltages V_{BS}, shown in the legend in volts. 61

Figure 21 Back-gated transfer characteristic of unprotected CNTFET (V_{DS} = 0.1 V). It exhibits *p*-type conduction and large hysteresis. 63

Figure 22 Mask for bonding pads. 66

Figure 23 Mask for CNT removal. 67

Figure 24 Mask for source drain electrodes..... 68

Figure 25 Layout of the CNTFET array. The center bar denoted by "S" is the common source electrode, shared by other drain electrodes, denoted by "D_2", "D_3", etc. Each source and drain pair comprise one transistor 71

Figure 26 (a) *I-V* characteristics of an ideal polarizable electrode, (b) *I-V* characteristics of an ideal non-polarizable electrode, the voltage ϕ is well-defined, and given by the Nernst equation. 72

Figure 27 Illustration of the concentration profile at an electrode-electrolyte interface. The interface is at $x = 0$. x_S indicates the Stern layer or inner Helmholtz layer, within which only specific adsorbed ions can reach. x_D indicates the Debye length, within which most of the concentration change happens. x_B indicates a distance from the electrode where the concentration reaches the bulk concentration of the ions. 75

Figure 28 The model of the electrical double layer. 76

Figure 29 Illustration of how extra charges induce a voltage shift in the transistor: (a) field lines before charge addition. (b) the equivalent circuit, Z_f is the Faradaic impedance, R_Ω is the solution resistance, C_d is the double layer capacitance. ΔV_{GS} comes mainly from the voltage drop change across the double layer capacitance. (c) field lines after charge addition..... 80

Figure 30 Schematics of the electrical measurement for (a) top-gated, (b) back-gated I_{DS}-V_{GS} transfer characteristics. 82

Figure 31 Steps for Acrydyte™ modified probe-DNA immobilization: (1) surface hydroxylation, (2) MPTMS exposure, (3) probe-DNA spotting. 84

Figure 32 Top-gated transfer characteristic through Ag/AgCl reference electrode and electrolyte buffer. The plot shows very good repeatability of device behavior upon

washing, blow-drying and buffer change. There are indeed 2 sweeps (forward and reverse) for both solid and dashed lines, but they are indistinguishable, therefore the hysteresis is negligible. 88

Figure 33 Transfer characteristic of CNTFET for probe-DNA only, 1 μM complementary target DNA hybridization, and subsequent dehybridization wash to remove the target DNA. The plot shows clear rightward (positive) shift in threshold voltage upon hybridization due to added negative surface charges from the target DNA, and a subsequent leftward shift after target DNA removal. 90

Figure 34 Fluorescent image taken after transfer characteristic measurement in Figure 33(*left*) fluorescent image of 1 μM complementary target hybridization, (*right*) fluorescent image after dehybridization wash to remove target DNA. 90

Figure 35 Threshold voltages of the transistors in the array upon DNA hybridization treatments. The plot shows universal positive shift in threshold voltage of all transistors upon complementary target hybridization, and recovery after target DNA removal through dehybridization wash. The bottom plot shows the spread of the voltage threshold shifts from the blue to the green curves. 91

Figure 36 Titration curve shows sensitivity and specificity of the sensor. The sensitivity level is somewhere between 10 to 100 nM. The signal difference between 1 μM hybridization of complementary (blue) and that of non-complementary target (red) clearly shows the specificity of the sensor. 93

Figure 37 Scanning gate microscopy of unprotected carbon nanotube transistor. The top images are topography images. The contrast in the bottom images represents the I_{DS} as a function of the tip position. The tip, which functions as the gate, was biased with the coresponding indicated voltages. 96

Figure 38 Transfer curve before (blue) and after (green) overnight salt exposure to aluminum oxide covered CNTFET. The threshold voltage positions indicated by the blue and green arrow clearly shifted to the left after positive ion penetration. Moreover the ions seem to either reach the channel to induce more scattering or screen the applied gate voltage. 98

Figure 39 UV-Vis absorption spectrum of BOCK conjugated gold nanoparticle solutions. The peak around 520 nm is due to plasmon resonance absorption of the 10 nm gold nanoparticles, the peak around 260 nm is due to the absorption by the conjugated nucleic acid aptamers. The dashed line is a fitted curve to determine the 260 nm absorbance contributed by the nucleic acid aptamers. 106

Figure 40 The color of BOCK conjugated gold nanoparticles with incremental addition of thrombin. The thrombin concentration is indicated by the label beneath each picture. The concentration of the gold nanoparticle is 20x more than that used in the rest of the aggregation assay, in order to emphasize the reddish color. The rightmost picture shows clear precipitation due to gold aggregation. 107

Figure 41 UV-Vis spectra of BOCK conjugated gold nanoparticles upon addition of thrombin. The added thrombin concentration is denoted in the legend. We observed that the 520 nm peak is gradually suppressed as more thrombin is added, without significant red shift in peak position. 108

Figure 42 UV-Vis spectrum of TASSET conjugated gold nanoparticles and that with added thrombin. The 520 nm peak is not suppressed upon thrombin addition, indicating that gold particles do not aggregate. 109

Figure 43 UV-Vis spectra of one base mistake sequences from BOCK, and those with added thrombin. Sequences with mistake located close to the gold nanoparticle behave as if they were correct BOCK sequence. 113

Figure 44 Absorbance at 520 nm of BOCK conjugated gold nanoparticle as a function of titrated thrombin concentration. An apparent K_d is extracted by looking up the needed thrombin concentration to suppress the absorbance half way between zero suppression and total suppression. 114

Chapter 1: Introduction

This dissertation focuses on the work I have done in the last three years of my PhD study on the development of carbon nanotube transistor arrays for electronic label-free DNA hybridization detection. My main goal is to lay the groundwork for establishing the feasibility of an electronic based system that can someday be used as a diagnostic tool for point of care application. Fluorescent-labeled DNA microarray technique is the current workhorse in gene identification, gene typing, gene expression analysis, and it is making wonderful progress in medicine and biology, including understanding the root cause of many genetic diseases, diagnosis, prognosis, and toward finding the correct treatments for genetic diseases. Genetic diseases are not restricted to those inherited from parents to offspring, but also those whose root-cause is genetic in nature, such as cancers, Alzheimer, diabetes, chronic cardiovascular diseases. We believe that microarray technology can significantly impact the health care delivery if it is made available in point of care facilities, so that every clinic can perform diagnosis of genetic markers for its patients quickly and affordably. The main impediments to widespread deployment of current DNA microarray are the laborious protocols and expensive detection instrumentation needed to perform it. In this work, we propose and demonstrate a prototype of an electronic label-free DNA detection device, which significantly cuts down the complexity of the protocols. In addition, our electronic device is simple, scalable, and does not require expensive instrumentation for read-out. To reduce system

complexity, we limit the number of genes which will be inspected at any given time, in contrast to current DNA microarray system, such as the one commercially available from Affymetrix, Inc, which is capable for searching hundred thousands of genome-wide genes in one experiment. We realized that a system which detects only dozens to hundreds of overly expressed or under expressed genes often suffices to characterize the specific stage of a certain cancer. After surveying other viable schemes, we believe our technique has the greatest potential for realizing our vision of having an affordable and widespread deployable system that allows for genetic testing for diagnosis and prognosis in clinics. Furthermore, it is very motivating to imagine such an affordable device being deployed to countries that are too poor to afford building sophisticated laboratory facilities, which undoubtedly would significantly improve the quality of healthcare in developing nations.

In this ongoing project, we ultimately envision our device to be capable for testing dozens of genes with the sensitivity level and specificity relevant to clinical requirements. In the work described in this dissertation, we have demonstrated detection of specific DNA binding in the 10-100 nM range. Based on the results of this work, we believe we have achieved a milestone and laid down the foundation for the development and optimization for electronic label-free DNA hybridization using carbon nanotube field effect transistors.

The organization of this dissertation is as follows: We begin with chapter 2 by introducing the historical progress in molecular biology up to the well-known central dogma, and describing relevant bioassays in gene analysis. Other viable DNA detection schemes are reviewed in chapter 3, and by doing so, we justify that our

scheme is worth the pursuit. Chapter 4 describes the properties of carbon nanotubes, the building block of our transistors. Chapter 5 describes how the carbon nanotube field effect transistor arrays are used for label-free DNA detection. Experiments, results, as well as simple models describing what to expect from the experiments are presented. We realized that the application of our device can be extended beyond DNA detection to other charged biomolecules, including antigens, antibodies, and proteins. Aptamers, nucleic acids with unique sequences and folding structures that exhibit specific affinity toward other biomolecules: antibodies, viruses, drugs, emerge to enable our device to detect other biomolecules if the corresponding aptamers are used in place of the probe DNA in DNA hybridization detection. Probe DNAs are single-stranded DNAs tethered on the device and serve as bait to capture the target DNAs. In chapter 6, we describe our systematic study to understand thrombin aptamer binding using gold particle surface plasmon resonant absorption, and from which we draw our conclusion on the versatility of electronic detection for biomolecules.

My specific contributions contained in this thesis and in my other publications to the advancement of science and technology are as follow:

- Demonstrated a new approach of making carbon nanotube field effect transistors for bio-sensing applications with an oxide overlayer,
- Fabricated and implemented reproducible carbon nanotube field effect transistors having intrinsic ambipolar transport characteristics,
- Decreased the amount of hysteresis in the device characteristics compared to those of unprotected carbon nanotube transistor,

- Developed protocols for attachment of probe DNA onto the carbon nanotube field effect transistor devices,
- Demonstrated detection of the specific nucleic acid hybridization in the range of 10 – 100 nM using carbon nanotube field effect transistors,
- Elucidated the binding mechanism between thrombin and the novel aptamers using the gold nanoparticle aggregation assays,
- Demonstrated the veracity of the ballistic magnetoresistance in magnetic point junctions (not discussed in the dissertation) [3],
- Demonstrated the use of scanning tunneling spectroscopy to distinguish iron atoms in a permalloy (nickel-iron) film (not discussed in the dissertation) [4].

Chapter 2: Bioassays at the molecular level

2.1. A brief history on the study of genes [1]

Inheritance of traits from parents to offspring has always been a marvel and of great interest to mankind. It was believed that each trait of the parents blended and got inherited by the offspring, until Gregor Mendel in 1865 published his findings on inheritance. Known as Mendel's laws of inheritance, which was derived from Mendel's systematic observations of the phenotype in garden peas, it concluded that instead of blending, inheritance was *particulate*. Each parent contributed particles, or genetic units, to the offspring. These particles are nowadays known as genes. According to Mendel, each plant carried two copies (diploid) of the genetic particles. A genetic unit or particle existed in several different forms, or alleles. One allele can be dominant over another. The daughter plant would exhibit traits dictated by the dominant allele. But the recessive allele was not lost, and may reappear in the traits of the granddaughter plant if it was paired with another recessive allele. However, the notion of the particulate nature of inheritance was not accepted and largely ignored by mainstream scientists at the time, until after 1900s, when the concepts of cell cycle, cell division, cellular reproduction and the nature of chromosomes were better understood. Mendel had predicted that gametes (sex cells) were haploid, and contained only one allele of each gene, instead of two. Mendel's law was later

accepted, since the number of chromosomes in gametes was then found to be one-half of that in other cells.

It was then accepted that inheritance was carried by chromosomes, but the building blocks for chromosomes were still unknown. The choices were deoxyribonucleic acid (DNA), ribonucleic acid (RNA) or protein. Frederick Griffith in 1928 showed that an avirulent (non-lethal) strain of bacteria can transform to become lethal after mixing them with dead virulent (lethal) bacteria. The transformation was not transient, but somehow the descendants of avirulent bacteria inherited or gained the virulent trait from the dead cells. Based on this, Osvald Avery proposed that DNA was responsible for the inheritance. Archibald Garrod, a physician, studied symptoms of a genetic disease that were believed to arise from abnormal build-up of an intermediate compound in a biochemical pathway. It had been widely accepted that enzymes in living things regulate biochemical pathways, and therefore Garrod concluded that a defective gene must give rise to a defective enzyme. The notion that genes should somehow direct the production of polypeptides, building blocks for proteins and enzymes, emerged. But scientists were still puzzled by how genes are replicated or reproduced, and how genes direct the production of polypeptides.

In 1953, James Watson and Francis Crick proposed a model for DNA. Watson and Crick did not perform the experiments themselves. They built their model upon data from others. In 1950 Erwin Chargaff studied the chemical composition of DNA and found that the content of purines (adenines + guanines) was always roughly equal to the content of pyrimidines (cytosines + thymines). Furthermore, the amounts of

adenine and thymine were roughly equal, so were the amounts of guanine and cytosine. This was known as Chargaff's rule. The other important piece of data came from the x-ray diffraction pattern performed by Maurice Wilkins and Rosalind Franklin in 1952. The pattern showed very simple spots, suggesting that DNA structure must be very regular and periodic. Wilkins and Franklin concluded that DNA was a helix. However the dilemma was if DNA contains genetic information, it must have an irregular sequence of bases, then how a regular periodic structure is possible to achieve that function. Watson and Crick's double helix model resolves the contradiction, and satisfies Chargaff's rule at the same time: DNA must be a periodic double-helix with its sugar-phosphate backbone in the outside and its bases on the inside. Moreover, the bases must be paired with a purine in one side and a pyrimidine in the other side. Watson and Crick further postulated from Chargaff's rule that adenines must always pair with thymines, and guanines must always pair with cytosines. Watson and Crick's model also suggests a mechanism for DNA replication. Since DNA is a double helix, with two strands complementing each other, the two strands can be separated, and each can then serve as the template to build two new daughter strands, which are exactly the same as the parent's, preserving the genes as cells divide. This mechanism was later confirmed by Matthew Meselson and Franklin Stahl in 1958.

The mechanism for protein production has now been established, and is known as the central dogma of molecular biology. The DNA in genomes does not direct protein synthesis itself, but instead uses RNA as an intermediary molecule. When the cell needs a particular protein, the sequence of DNA bases from the

appropriate portion or portions of the extremely long DNA molecule in the chromosome is transcribed into RNA (the process is called transcription). The resulting RNAs are used directly as templates for protein synthesis (the process is called translation). The flow of genetic information in cells is therefore from DNA to RNA to protein.

2.2. Fractionation of cell components

In order to study DNA, RNA and protein that determine the physiology of a cell, scientists have utilized methods to study components within the cell, which will be discussed in this section. Advances in microscopy have an important role in the progress of molecular biology. The first step is to extract the components inside a cell by breaking open the cell membrane, called lysis. One of the methods is osmotic shock. By putting cells in a saline solution, cells will take up water to balance the osmotic pressure, and as a result, they will swell and eventually rupture. The situation is much like brain swelling, causing death to dehydrated athletes. In practice, biologists carefully follow protocols, such that the disruption procedures leave cell components, e.g. cell nuclei, mitochondria, the Golgi apparatus, lysosomes, etc. largely intact. The result is a thick slurry suspension containing a variety of cell components, each with a distinctive, size, charge, and density. This suspension is then treated with repeated centrifugation at progressively higher speeds to fractionate homogenates of cells by weight or correspondingly size. Heavier or larger components sediment at lower speed; and the supernatant consisting of lighter or smaller components are separated and subjected to the next stage of higher speed

centrifugation. Eventually biologists can extract the tiny sub-cellular components such as DNAs, RNAs and proteins. In the following, we will describe the methods used to fractionate these nucleic acids and proteins.

2.2.1. Electrophoresis

Gel electrophoresis is a method to separate DNA or protein by size. Agarose gel is often used for DNA electrophoresis, while polyacrylamide gel is used for protein electrophoresis. The basic principle relies on different friction according to the size of DNA/protein while the charged-DNA/protein travels in the gel under an applied electric field. In the most simplified model, we can think of the driving force is being balanced by the frictional drag force:

$$\vec{F} = e\vec{E} = b\dot{x}\ ,\ \ \dot{x} = eE / b \qquad (1)$$

Therefore DNA/proteins of different sizes would travel for different distance after some time. After staining steps for visualization purposes, one would see bands of DNA/protein fragments in the gel. Smaller molecules, experiencing smaller frictional drag force, travel with higher speed and a longer distance in the gel. As a result, the band is located further from the start line.

Since DNA is ionized to carry one negative charge for every base or nucleotide, the driving force is proportional to the size of the DNA molecule, which is desired. Unlike DNA, proteins are not ionized to carry intrinsic charges. Instead, the native charges of proteins depend on pH and the type of peptides. Protein electrophoresis is often pretreated with SDS (sodium dodecyl sufate), a detergent. The SDS would denature the polypeptide folding so that the subunits do not bind to each other, and coat each subunit to carry negative charge from the ionized SDS. The

situation is then much like the DNA, because the amount of charges is now proportional to the size of the polypeptide. The proteins would electrophorese into

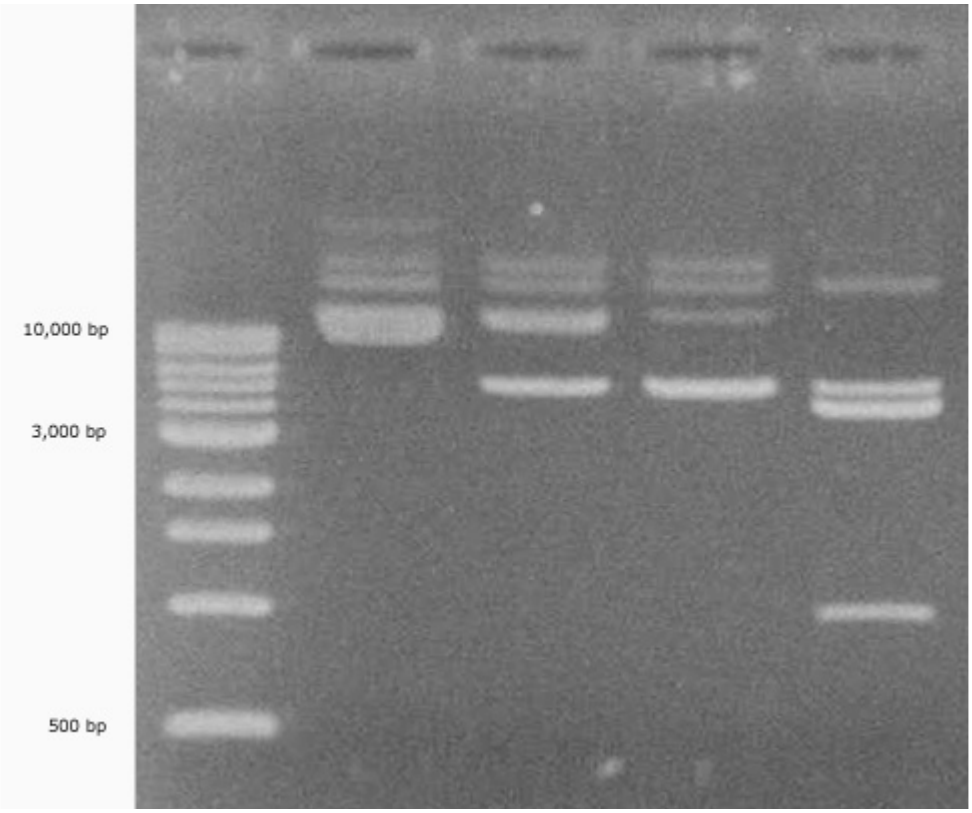

Figure 1 An example of agarose gel electrophoresis. The left lane is DNA ladder serving as size calibrator. Smaller DNA travels further down the lane. The other four lanes are various samples that are being fragmented. (Source: wikipedia.org)

bands, due to difference in frictional drag force, which is size-dependent.

2.2.2. Chromatography

Chromatography is an old term, originally refers to a technique to separate an ink into patterns of bands, as the ink creeps up a filter paper. Two major types of chromatography pertinent to molecular biology are ion-exchange chromatography, and gel filtration chromatography.

Ion exchange chromatography uses a charged resin to separate substances according to their charges, for example, DEAE-Sephadex® resin contains positively charged diethylaminoethyl (DEAE). These positive charges attract negatively charged substance, including proteins. The greater the negative charge, the tighter the binding. First, the substance is loaded to pre-packed DEAE-Sephadex slurry in a chromatography column, followed by elution steps of solutions of gradually increasing ionic strength through the column. As the ionic strength of the elution buffer increases, fractions of charged-separated substance are collected. The purpose of increasing ionic strength elution buffer is to enhance the charge screening, such that the negatively charged substances would get loose from the positively charged resin.

The chromatography column in gel filtration chromatography is pre-packed with porous beads, like hollow balls with holes in them. When a solution containing different size of molecules is passed to the column, the small molecules would easily enter the holes in the porous beads and are slowed in their journey down the column, but larger molecules would not be able to enter those holes, and would flow quicker through the column. Opposite to the situation in gel electrophoresis, where larger molecules travel slower due to higher friction, larger molecules in gel filtration chromatography are less impeded and travel faster. In general, a conventional column chromatography relies on gravity, and its resolution is limited by inhomogeneities in the matrices (i.e gel, resin). Newer chromatography, called high-performance liquid chromatography (HPLC) utilizes tiny spheres of diameter around $3 - 10$ μm, that are packed very tightly to form a uniform column bed. Since they are so tightly packed,

liquid in a HPLC column has negligible flow rate under gravity. These columns, usually packed in steel cylinders, require high pressure to drive the liquid down, and involve elaborate systems of pumps and valves.

2.3. Recombinant nucleic acid techniques [2]

Recombinant DNA is any DNA molecule formed by combining or attaching different sequences together. Before 1961, it was not known that DNA denaturation

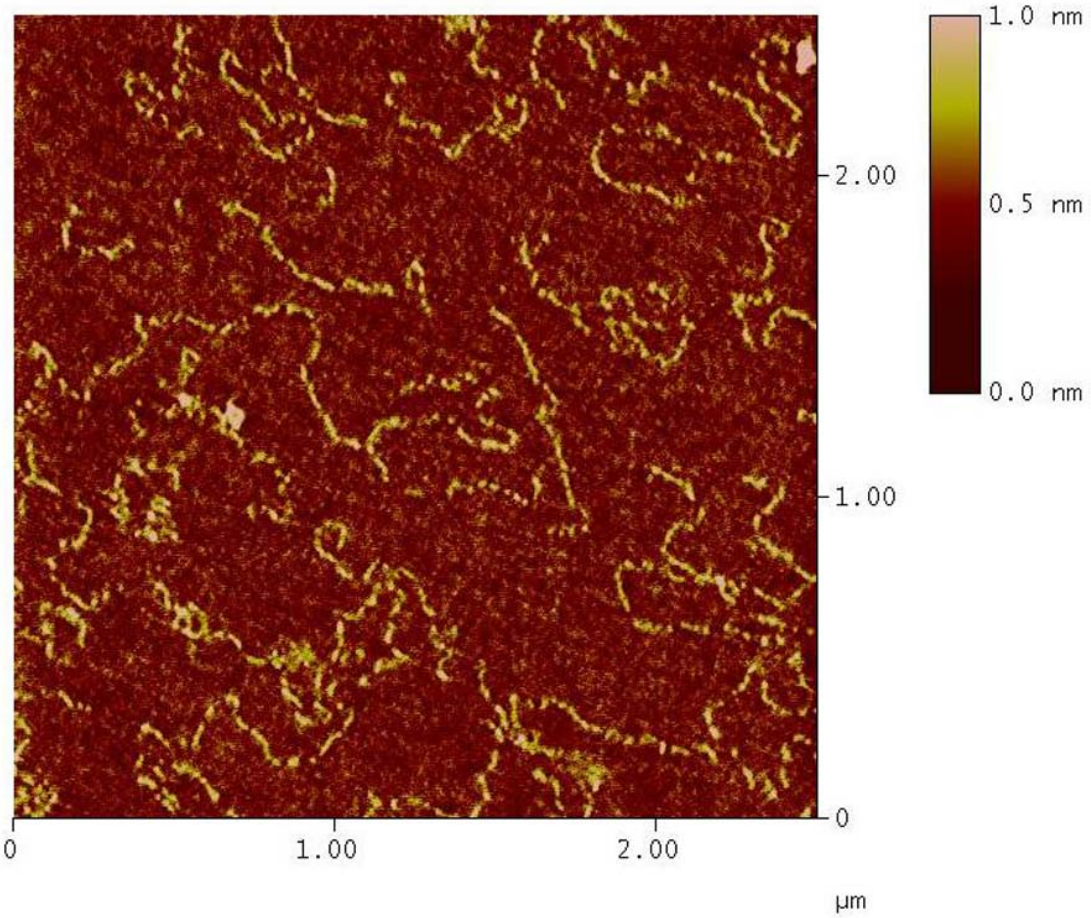

Figure 2 Atomic force microscope (AFM) image of linearized plasmid DNA (pGem7zft) on mica surface. The color map on the right indicates the height. (Data taken on Feb 2005, H. Pandana)

was reversible. Later it was discovered that matched single-strands of DNAs may re-form double-helices. Hybridization, the ability of one single-stranded nucleic acid to form a double-helix with another single strand of complementary base sequence, has been the underlying principle for several recombinant techniques These techniques are capable to identify DNA, called DNA typing and DNA fingerprinting. It was found that in several places in human genome there are DNA fragments that contain mini-satellites, sequences of bases repeated several times. Moreover, the pattern of repeats differs from one individual to another. The pattern then may serve as fingerprint, which is unique for every individual. The impact is far-reaching: DNA fingerprinting finds forensic uses; DNA identification can identify markers that are unique to certain diseases; Evolution lines can be traced genetically. One can utilize hybridization to search for related but nonidentical genes. DNA can also be hybridized to RNA. One utilizes known sequence of DNA probes to analyze RNA samples to find out whether a cell is expressing a given gene.

2.3.1. Nucleic acid hybridization

The DNA is a double helix with specific base-pairings between purines and pyrimidines as described by Watson and Crick. There are several factors that determine the energetics of DNA binding: hydrogen bonding, electrostatic screening, base stacking, and configurational entropy.

Hydrogen bonds between the base-pairings favor binding. There are two hydrogen bonds between A and T, and there are three bonds between G and C.

As DNA is ionized in buffer solution, its phosphate group in each strand will carry negative charges. The like-charges between the two strands tend to repel each

other. To induce binding, DNA has to be dissolved in high salt or ionic solution to screen this like-charge repulsion, such that the bases can be brought close enough together to form hydrogen bonds.

In the double helix structure, the paired-bases are stacked on top of each other forming π-bonds. The π-bonds favor binding, and are responsible for the decrease in UV absorption, which is used to measure melting temperature of DNAs. Melting temperature is the temperature at which 50% of the DNA is hybridized (bounded), and 50% of which is separated (single-stranded). (Figure 3).

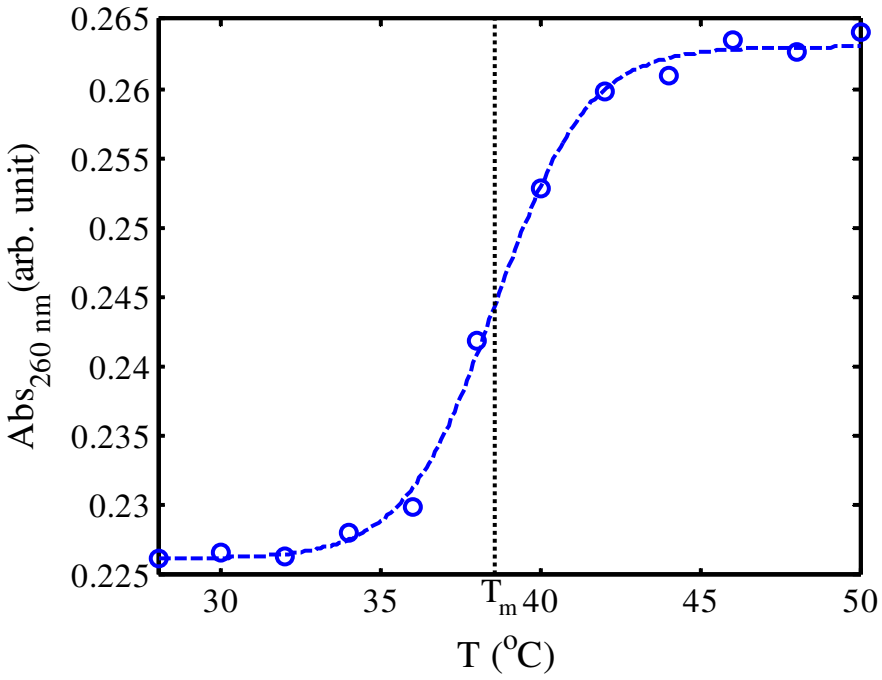

Figure 3 Denaturation curve of 15-mer DNA oligonucleotides (5'-AAT ATT GAT AAG GAT-3') hybridized in 10 mM PBS ph 7, 0.3 M NaCl buffer. As temperature is raised, the absorbance at 260 nm increases, contributed by denatured or separated DNA bases. The melting temperature T_m at 38.6 °C is indicated in the plot as the temperature at which 50% of the DNA is denatured. (Data taken on August 2005, H Pandana, D. B. Romero)

Double-helix is an ordered, regular structure. The entropy of this structure is less than that in separated, unordered DNA. As we know the change in free energy is the negative of the change in entropy times the temperature, i.e. $\Delta F = -T\Delta S$. As the change in entropy (ΔS) from single stranded to double stranded is always negative, therefore the double-stranded formation always costs energy. But we can reduce this energy cost by reducing the temperature. This energy cost is paid by the gain in energy from the hydrogen bonds, which is more than this energy cost. So the total energy is actually lowered upon double-stranded formation.

From these considerations, we can conclude simple but important implications: To induce hybridization or binding, we would like to have high salt (to reduce electrostatic screening), and low temperature (to reduce entropic cost). Long DNA has higher melting temperature, as it is being stabilized by a larger number of hydrogen bonds.

2.3.2. Blotting

As described above, a biologist would extract subcellular components, DNAs, RNAs, proteins through repeated steps of fractionation and sorting them according to size through electrophoresis and chromatography. Once the biologist size-separates the DNAs or RNAs in the gel electrophoresis, he/she would like to be able to recover the genetic materials out of the gel for subsequent hybridization analysis. The gel containing DNA fragments to be analyzed is removed to a blotting apparatus (Figure 4). A sheet of nitrocellulose membrane is laid over the gel. Through capillary, the DNA fragments will move and get stuck to the nitrocellulose membrane. The membrane can be subsequently hybridized with fluorescently labeled DNA probes.

The sequence in DNA probes are known beforehand. By looking at the fluorescent signal, the biologist will be able to identify the genes in the unknown DNA fragments. Customarily a standard size marker was run in the gel electrophroresis in parallel with the DNA samples. Therefore in the end, the biologist can identify both the size and sequence of the DNA fragments of interest. The DNA blotting is called Southern blot, named after Edwin Mellor Southern. If the gel contains RNA instead of DNA, then the RNA transfer to membrane is called a Northern blot.

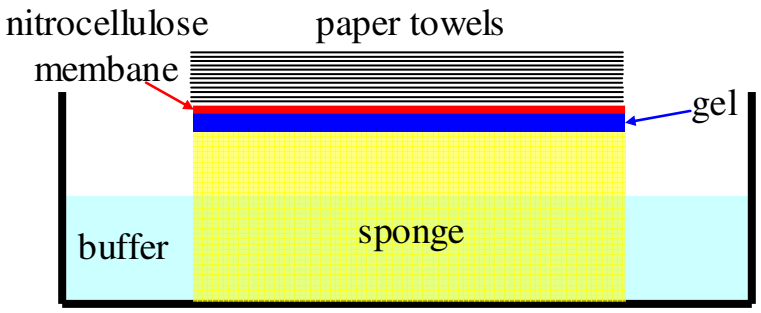

Figure 4 Schematics of blotting apparatus. As the buffer wicks up the sponge to the paper towel stack, it brings the DNA/RNA/protein in the gel to the nitrocellulose membrane.

2.3.3. Sample multiplication: polymerase chain reaction

Often times the sample extracted from tissue is too little for gene analysis, and therefore requires amplification. Kary Mullis was awarded the Nobel Prize in Chemistry in 1993 for his invention of polymerase chain reaction (PCR). PCR allows the DNA from a selected region of the sample to be amplified a billionfold, effectively purifying this region from the remainder of the sample.

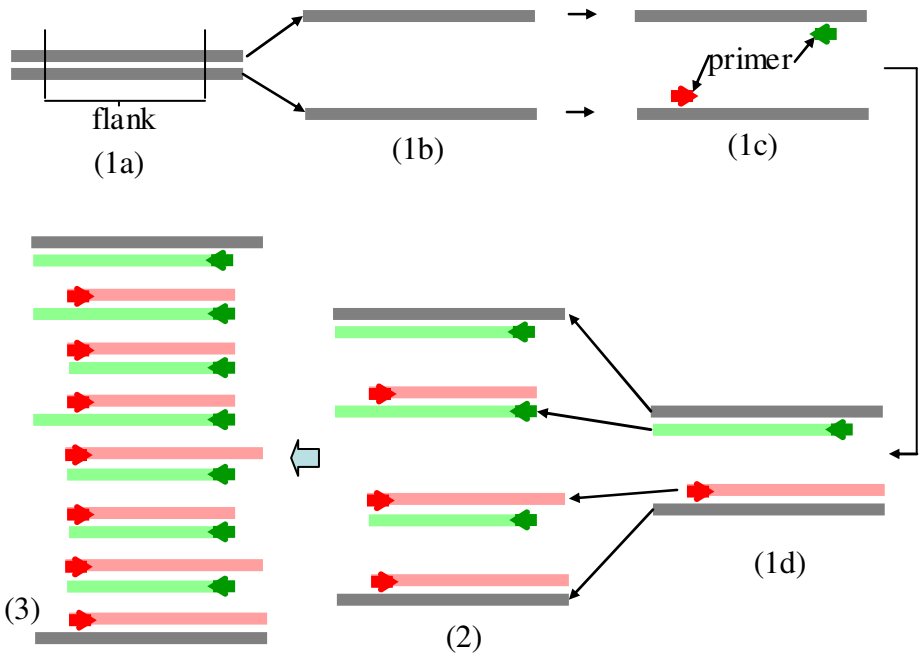

Figure 5 PCR steps: (1a) Start of cycle 1. Primers are chosen to multiply the DNA sequence in the flanked area. (1b) Denaturation step of cycle 1 to denature the double stranded DNA, each strand will serve as a template in the polymeration step. (1c) Primers hybridization. (1d) DNA synthesis activated by DNA polymerase. Monomers extend each primer to form two new daughter strands. (2) Repeat of the thermal cycling in cycle 2 yields 2^2 DNA. (2) Repeat of the thermal cycling in cycle 3 yields 2^3 DNA. One can recognize immediately the PCR cycles yield multiplication of the flank only.

Two sets of DNA primers, chosen to flank the desired region in the gene, are chemically synthesized. PCR runs in cycles of heating and cooling. Every cycle doubles the amount of DNA synthesized in the previous cycle. In practice, 20 to 30 cycles are required for effective DNA amplification, which generates 2^{20} to 2^{30} – fold of multiplication. In each cycle, the sample is first heated to denature the DNA, each DNA strand would serve as a template for the next cooling step, in which the primers are hybridized to the templates. In the third step, DNA polymerase, an enzyme that

occurs naturally in living organism, along with the monomers (dATP, dTTP, dGTP, dCTP) will synthesize two new strands from each primer according to the template. So the starting one double strand now yields two double strands. The thermal cycle is then repeated until enough amount of DNA is desired.

2.4. Gene identification and gene expression: Microarray

The recombinant nucleic acid techniques that we have briefly discussed in the previous section have enormous impacts toward the progress in medicine and biology. Upon the completion of human genome sequencing, there is a need for a technique that can perform gene hybridization in parallel for the massive amount of genes. Beside gene identification, which is to identify the sequence of a gene associated to a certain trait and its location within the genome, gene expression study is also desired to understand the functions of the gene. As described before, the central dogma suggests that a gene is useful only when the corresponding protein is produced to run the cell's metabolism. In a gene expression study, the level of expression of mRNA which will lead to protein production at different stages of the cell's development is of particular interest. By expression level, we mean the amount of mRNA generated upon the transcription process (DNA → RNA). DNA microarray has revolutionized the genomic study by having hundred thousands of genes spotted on a piece of glass slide. Rather than searching for the gene one at a time, a biologist is able to search for hundred thousands of genes in one experiment. Undoubtedly the DNA microarray also generates formidable amount of data to handle, and thereby spawning the field of bioinformatics.

In a DNA microarray, known sequences of DNAs, called probe DNAs are spotted and tethered to a glass-slide through an attachment chemistry. Each DNA spot in the microarray contains one specific sequence corresponding to a specific gene. The goal is to use the DNA microarray to identify and hopefully quantify the unknown genes in an analyte solution. The most common way is to label the unknown genes or DNAs, called target DNAs with fluorescent dye, and to hybridize the analyte solution to the microarray. Owing to specific base-pairing, certain genes in the analyte will bind to the matching probe DNA on the microarray. Upon washing, designed to remove excess and non-specific binding, the microarray is scanned for the fluorescent signals. Since the sequence on each spot in the array is known, one can straightforwardly identify what genes contained in the unknown analyte by looking at which spots fluoresce. Fluorescent DNA microarray may achieve semi-quantitative analysis by comparing the relative brightness of the spots, which is an indication of the amount of target-DNA present in the analyte solution.

One can also do comparative assay on DNA microarray. In this case, two samples are extracted from two different types of cells, for example from healthy cells and tumor cells and compare the amount of genes expressed in the two cells. The samples are labeled with different dyes. Healthy cells are often labeled with green fluorescent dyes, and tumor cells are labeled with red. The two samples are then mixed together and hybridized simultaneously to the DNA microarray. The target genes from the two cells would compete for the same probe-DNA. By comparing the hue, i.e., greenish or reddish tint, the relative abundance of the genes form the cells can be inferred. If the spot appears red, the tumor cells have expressed

more of the genes in that corresponding spot than the healthy cells. If the spot appears yellowish, then both healthy and tumor cells have very similar expression levels. The color determination utilizes sophisticated signal processing schemes. Systematic errors, i.e., unequal amounts of cells, can lead to unintended color bias. Thankfully there are genes that are expressed the same way in both healthy and tumor cells, and these are used to calibrate the baseline.

One of the most successful microarray developers is Affymetrix, Inc. Instead of robotic spotting, the probe DNAs or spots on a Affymetrix® chip are built-up one nucleotide at a time. The photolithographic process begins by coating of a light-sensitive chemical compound that prevents coupling between the quartz wafer and the first nucleotide of the DNA probe being created. Lithographic masks are used to either block or transmit light onto specific locations of the wafer surface. The surface is then flooded with a solution containing either adenine, thymine, cytosine, or guanine, and coupling occurs only in those regions on the glass that have been deprotected through illumination. The coupled nucleotide also bears a light-sensitive protecting group, so the cycle can be repeated. In this way, the microarray is built as the probes are synthesized through repeated cycles of deprotection and coupling. The process is repeated until the probes reach their full length, usually 25 nucleotides (Figure 6). Using the benefit of photolithography, they can make very dense array. Each spot size is only several microns, as opposed to several hundred microns in robotic spotted microarray. The spot size in robotic spotted microarray is limited by how small a pin can be machined.

In the next chapter, different read-out schemes to detect DNA hybridization will be discussed.

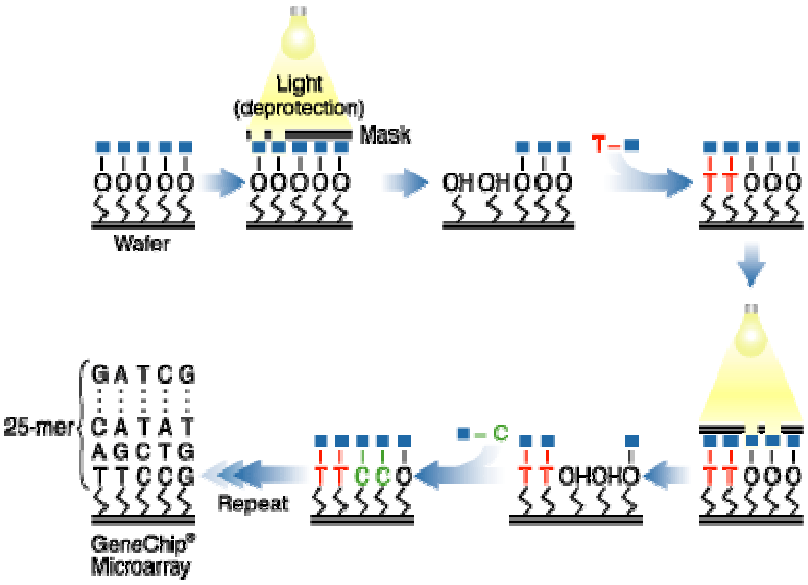

Figure 6 Affymetrix uses a unique combination of photolithography and combinatorial chemistry to manufacture GeneChip® Arrays. (source: www.affymetrix.com)

Chapter 3: Comparison of current available DNA detection schemes

3.1. Direct and sandwich assay

'Label-free' is an important buzzword in biomolecular detection, and hence the word is worth some detailed explanation. Generally it means that the target samples do not need reporter-molecules such as fluorescent or radioactive dyes to reveal their locations. Label-free assays are highly desirable, since the considerably labor-intensive step of attaching labels can be bypassed. However probe DNAs, which are the known sequences, may contain labels and the assays can still qualify as 'label-free'. Given this, even originally labeled assays, such as detections by fluorescence and electrochemical redox potential can be made label-free by introducing sandwich assays. In a sandwich assay, there are three strands involved: a surface tethered short capture probe, whose sequence is general enough such that part of most target sequences is complementary to the capture sequence; a labeled signaling-probe with a specific sequence to interrogate the unknown target; and the unknown label-free target that is longer than both the capture-probe and the signaling-probe. The sandwich assay is generally performed by first hybridizing the unknown target samples to the surface tethered capture probes, then the target sequences are revealed by the existence of the labeled signaling-probes, subsequently hybridized to the targets.

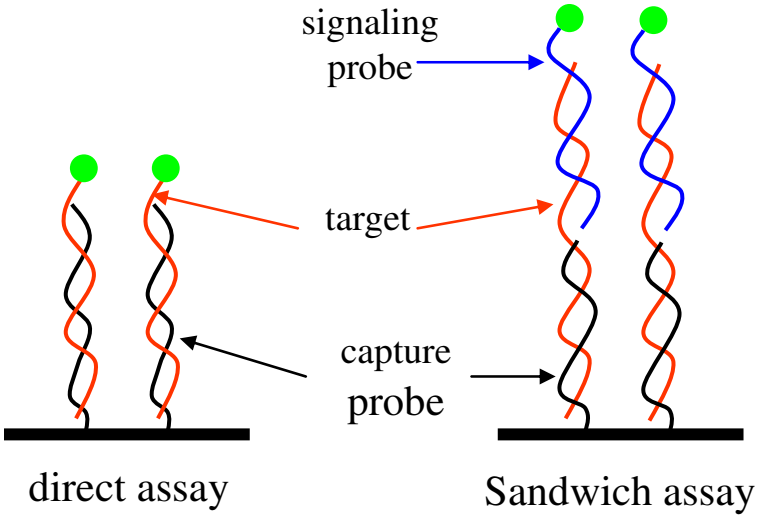

Figure 7 Comparison of direct assay and sandwich assay

While using sandwich assays, one can avoid labeling the target samples and transform the conventional non-label-free assays to 'label-free'. There are, however, drawbacks in introducing sandwich assays, which underscores the need for label-free assays. This is why a burgeoning amount of publication on developing label-free assays has recently mushroomed in the literature. Hybridization efficiency is never 100 %, and non-specific binding is never totally eliminated. Hence, it is of crucial importance to keep the assays simple. Adding an extra hybridization step as in the sandwich assays often reduces sensitivity and specificity. In fact, it was shown that the sensitivity and specificity of sandwich assays can at best only be in the same order with those of direct assays [5].

In the remaining sections, we define label-free only in the strict context of label-free in direct assays. Fluorescent detection and electrochemical redox detection

are grouped under non-label-free assays. We will examine the pros and cons of other label-free assays and evaluate the position of our electronic DNA detection scheme within the figure of merits of other label free assays.

3.2. Labeled technique (1): Fluorescent detection

Fluorescence is an electronic transition process, wherein light of a longer wavelength is emitted subsequently after absorption or excitation by a shorter wavelength of light. Fluorescent-based detection is by-far the most widely accepted method for both DNA hybridization detection and protein (antigen/antibody) immuno-sensing in the molecular biology community, owing to the availability of a large variety of dyes with defined emission spectra and their compatibility with conjugation techniques, and established microscopy detection techniques [6]. Arrays containing hundred thousands of different probe sequences or genes have been constructed [7]. The fluorescent dye labels can be applied through direct conjugation to the target DNA or random insertion into the nucleotide sequence by enzymatic reaction. The former is used in labeling signaling probes in sandwich assays, while the latter is used to label c-DNAs in direct assays.

There are several methods known to improve the detection of fluorescent dyes. 3-D polymer coating such as hydrogel, which provides larger surface area, is used as the microarray substrate rather than a 2-D monolayer coated surface, in order to increase the probe-DNA density or loading. Although hydrogel coating provides higher probe-DNA loading, and higher signal, it also increases the background noise due to nonspecific binding. Moreover the hydrogel may restrict the diffusion of target

molecules to reach the probes. A scheme using multilayers of optical thin films deposited on top of the microarray substrate has been demonstrated [8]. The multilayer stacks serve as interference layers to reflect the fluorescent signal, which would otherwise be absorbed by the substrate. However, the multilayer is only effective for enhancing one particular band of wavelengths, thereby reducing its utility in assays where multiple fluorophores are desired. The use of intense laser beam to excite the fluorophores has also been used. However it is only good up to a certain point, since the emission of fluorophores would saturate, and leads to photobleaching and non-linear emission response. Microarray read-out using a confocal microscope, which collects light only from a certain focal plane, improves sensitivity, but it requires very flat surface on the microarray spots which is difficult to meet in practice [9]. The long scanning time required for confocal imaging is a disadvantage, as fluorophores may photobleach before the acquisition is finished.

To reduce background noise, new strategies have been elaborated recently. Among the most promising are total internal reflection fluorescence (TIRF) [10], and fluorescence lifetime imaging microscopy (FLIM) [11]. The concept of TIRF is to excite only fluorophores bound to the surface by an evanescent wave generated by total internal reflection. In this manner unbound molecules in the bulk solution which are regarded as noise are not excited and hence do not fluoresce. In FLIM, the light source is pulsed and synchronized with a gated detector. The fluorescence is detected after a certain time delay from the pulsed excitation. Lifetimes of typical organic fluorescent dyes are between 0.5 to 5 ns, whereas autofluorescence from microarray

substrate and most biological samples decay within picoseconds range. Therefore, introduction of a correct time delay can greatly eliminate these autofluorescent noises.

A fluorescent signal only tells us that the fluorophores or reporter molecules exist at those particular locations. But their existence can be due to partial matching to the probe-DNA or even non-specific bindings. If the probe DNA's were attached using laser sensitive linkers, they can later be released by laser illumination for further analysis by mass spectrometers.

Fluorescence DNA detection systems often involve high level of redundancy in probe DNA sequence design to guard against false positives and false negatives. Fluorescent-based systems, as a consequence, require expensive detection instrumentation and sophisticated numerical algorithms that only large research laboratories can afford. Fluorescent-based biosensors have been shown to achieve sensitivity of 10 picomolar with very sophisticated photomultiplier detectors [12], and down to 3 zeptomolar (10^{-21} moles/liter) after signal amplification [13]. Affymetrix, Inc., the major DNA microarry vendor, claims that the sensitivity of its product, GeneChip®, is 1.5 pM [14].

3.3. Labeled technique (2): Electrochemical detection

3.3.1. Randles equivalent circuit in electrochemical modeling

Electrode processes and electrochemical systems are very complicated systems. A widely used simple model to describe the processes at an electrode-electrolyte interface is the Randles equivalent circuit, shown in Figure 8. R_Ω

represents the solution resistance. C_{dl} represents the double layer capacitance, which is the capacitance arising from rearrangement of ions in the electrolyte, in contact with a charged or polarized electrode, into an inner Helmholtz layer containing only specifically adsorbed ions or molecules, and a diffuse layer containing nonspecifically adsorbed species. A series of R_{ct} and W describes the Faradaic impedance. A Faradaic process is a type of electrode process in which charges or electrons are transferred across the electrode-electrolyte interface through chemical oxidation or reduction reactions. An electrode process is called non-faradaic, if it does not involve charge transfer. But processes such as adsorption and desorption can occur and the structure of the electrode-electrolyte interface can change with changing potential or solution composition. Although charge transfer does not occur in a non-faradaic process, a transient current flow is possible due to rearrangement of solution composition. This non-faradaic charging current is modeled by the C_{dl} in the equivalent circuit. Both faradaic and non-faradaic processes normally occur when electrode reaction takes place, therefore they are modeled as parallel elements in the equivalent circuit. R_{ct} is purely resistive and represents the charge transfer resistance in the faradaic process, and Z_W is the Warburg impedance that describes the impedance due to mass transfer. The total impedance of the equivalent circuit is measured as a function of frequency, and is usually plotted as a Bode plot (Figure 9) or Nyquist plot (Figure 10).

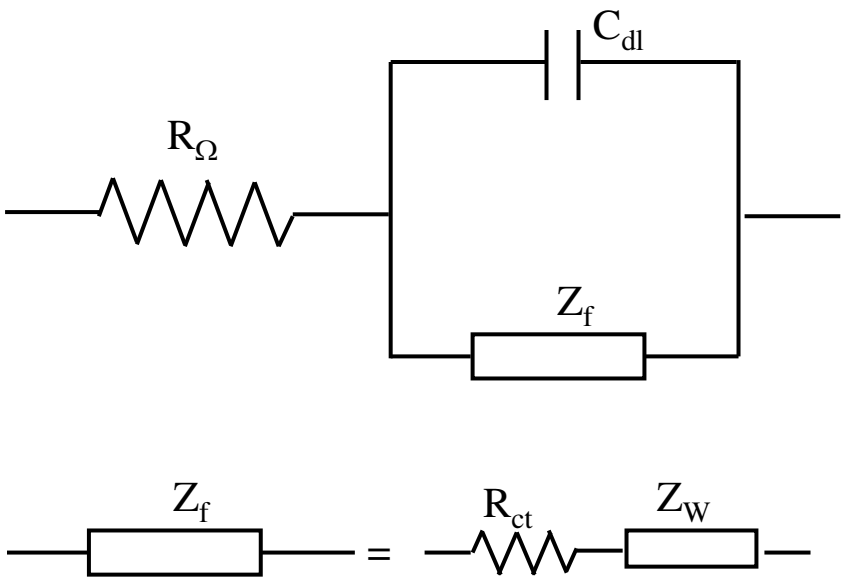

Figure 8 Randles equivalent circuit to model electrode-electrolyte interface.

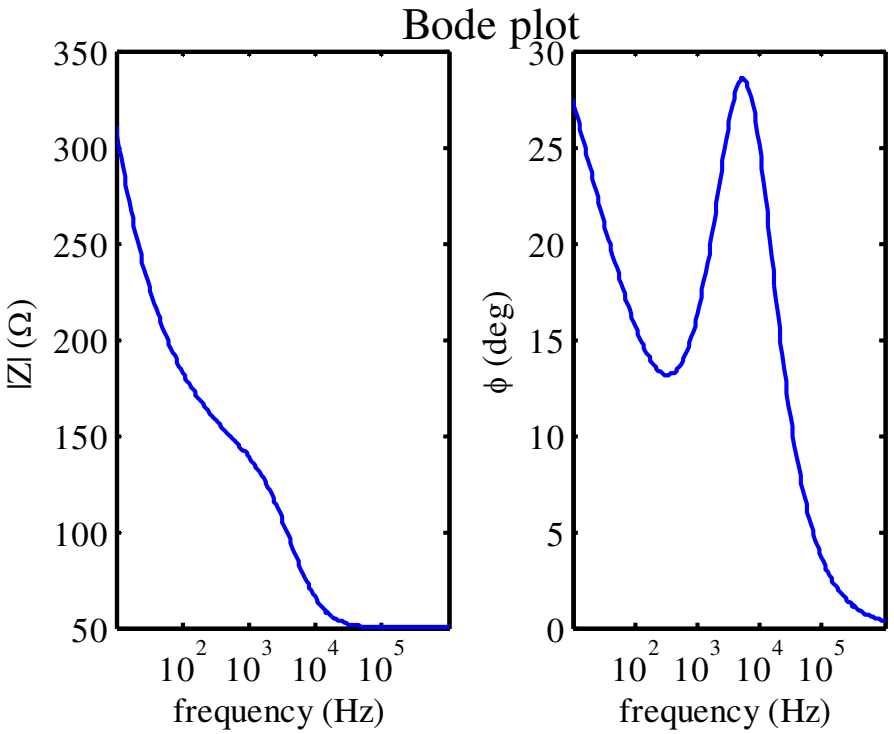

Figure 9 A Bode plot of the Randles equivalent circuit.

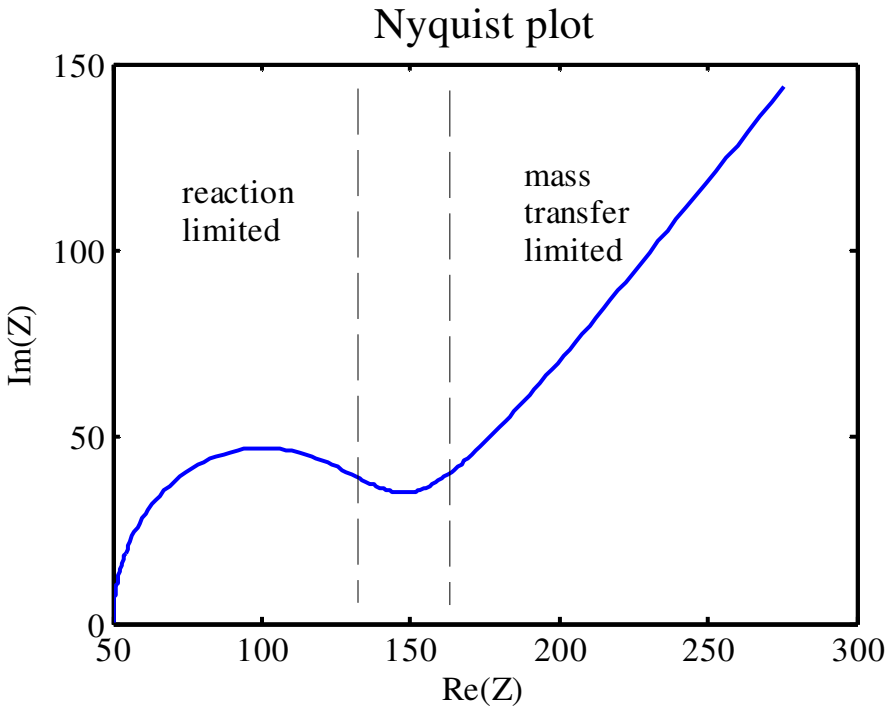

Figure 10 A Nyquist plot of the Randles equivalent circuit, showing both regimes of reaction limited at high frequency and mass transfer limited at low frequency.

3.3.2. Measurement techniques and detection schemes

Electrochemical DNA hybridization detection seeks for a signal of oxidation or reduction reaction happening on the functionalized electrode through electroanalytical measurements, such as impedance spectroscopy and AC voltammetry. A chemical oxidation or reduction reaction on an electrode leads to charge transfer on that electrode and the rate of the electrode reaction can be measured from the electric current flowing through the electrode. In general, the current or the overall reaction rate is governed by the rate of several processes: mass transfer of the species from the bulk solution to the electrode surface; chemical

reactions preceding or following the electron transfer; surface processes such as adsorption and desorption; and the actual electron transfer at the electrode surface. In an impedance spectroscopy measurement a small AC voltage excitation, which may sit on top of a DC voltage is applied to the load, while the response or current is analyzed through a lock-in amplifier. Both in-phase and out-of-phase components are obtained, and from which the impedance of the load can be extracted. (i.e. The real and imaginary parts of the impedance can be plotted as a function of frequency as in Bode plot, or plotted to each other as in Nyquist plot.) Components of the equivalent circuit model are extracted from the impedance spectroscopy measurement, and compared between before and after hybridization. In an AC voltammetry measurement, a fixed frequency is used, but the small AC voltage excitation is superimposed on top of a linearly swept voltage. Sometimes full information of frequency dependence and bias voltage dependence is desired, and both AC voltammetry and impedance spectroscopy are combined together.

DNA electrochemical detection schemes can be categorized into the following: detection of redox labels; detection of the direct or indirect oxidation of DNA bases; nanoparticle based electrochemistry amplification. Redox labels may include daunomycin, methylene blue, cobalt phenanthroline, ruthenium bipyridine, osmium bypyridine, ferrocene. Sensitivity of redox label detection has been demonstrated to 50 nM using AC voltammetry [15], and recently higher sensitivity up to 50 fM has been demonstrated upon signal amplification of the redox species through alkaline phosphatase catalyst, measured using impedance spectroscopy [16]. Colloidal gold nanoparticles have also been used to amplify the hybridization signal in

sandwich-based assays, in which the appearance of the characteristic gold-oxidation signal is sought. Using such a scheme, a sensitivity of 0.8 femtomoles of PCR amplicons (i.e. DNA products obtained from PCR amplification process) has been shown [17]. Detection schemes based on DNA bases oxidation, i.e. guanine, clearly destroy the sample and often suffer from high background redox current. Nevertheless sensitivity of 550 attomoles upon amplification of DNA has been demonstrated [18]. In short, despite high sensitivity, direct label-free electrochemical-based detection schemes are destructive since they look for guanine oxidation signal. Redox labeling works similarly as fluorescent labeling, and the techniques can be made label-free by opting to sandwich assays.

Figure 11 shows how the Nyquist plot changes upon hybridization. One feature to look at is the radius of the semicircle, which represents the R_{ct} in Randles

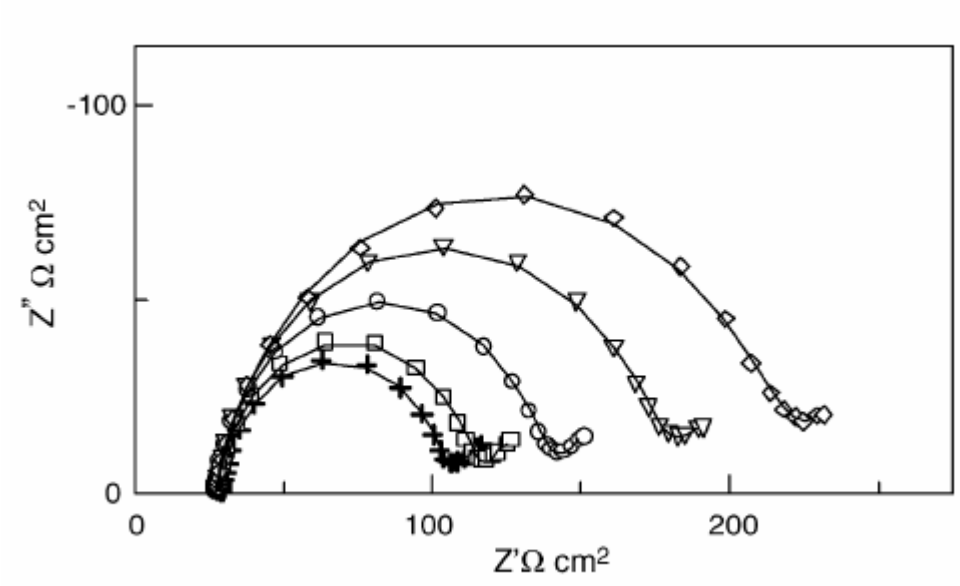

Figure 11 Nyquist plot of a polypyrrole-DNA films after hybridization with its complementary target: 0 μM (+), 0.5 μM (□), 2μM (○), 3.5 μM (∇), 5.5 μM (◊). Reprinted from [19].Copyright (2005) Elsevier.

equivalent circuit, and it is shown to be increasing upon target binding in. Figure 11. However, contradicting results have also been reported [20], which shows decreasing R_{ct} upon target binding. Although electrochemical redox detection has been around for a while, the complexity of the electrochemical processes prevents this technique to be mature enough to be commercialized, since results vary dependent upon a particular experimental setup. Nevertheless, Combimatrix™ has commercialized gene chips with its own proprietary protocols and measurements.

3.4. Label-free direct assays

To achieve label-free detection, one needs to exploit the intrinsic properties of the DNA target samples. Actually there is only a limited number of intrinsic physical properties that can be exploited: the dielectric constant, the negative charges from DNA phosphate backbone when ionized in a solution; and weight. The dielectric constant can be measured optically through refractive index measurement, or electronically through impedance or capacitance measurement. Electric charges can be detected through field effect using active semiconductor devices, and weight can be measured using a very sensitive spring. In the following, we will discuss each label free assay categorized upon the physical property it detects.

3.5. Label-free (1): dielectric constant

3.5.1. Refractive index measurement: Surface plasmon resonance

Surface plasmon resonance (SPR) is the resonant transfer of energy from an excitation source into a surface plasmon wave. Surface plasmon wave (SPW) is a charge-density wave, excited at the surface or boundary of plasma. Surface plasmon wave can be radiative or non-radiative [21]. The SPW excited in SPR biosensors is non-radiative. Non-radiative SPW requires an interface of two media with opposite sign dielectric constants, for example, a metal and a dielectric. The SPW excited is a TM-polarized wave and decays evanescently into both media. The condition for SPW excitation is governed by its dispersion relation which is a function of the dielectric constants of the two interfacing media. This gives rise to its sensitivity to changes in the dielectric constant or refractive index at the interface where the evanescent SPW is excited, a scenario occurring in most bioassays. The excitation of SPW results in a resonant transfer of energy into the SPW and can be detected as an energy loss of the excitation source.

3.5.1.1. Dispersion relations of SPW

As mentioned before , SPW can be radiative or non-radiative. Radiative SPW has a non-zero real wavevector. This means that the wave can propagate inside the plasma, which we assume to be a metal in our discussion. Non-radiative SPW has a purely imaginary wavevector, and the wave would decay evanescently. The dispersion relation for the radiative wave can be obtained by substituting the dielectric constant expression into the homogeneous vector wave equation [22]:

$$\nabla^2 \vec{E} - \mu\varepsilon \frac{\partial^2 \vec{E}}{\partial t^2} = 0 \tag{2}$$

From Drude model, dielectric constant for a metal can be written as [23]:

$$\varepsilon(\omega) = 1 - \frac{\omega_p^2}{\omega^2} \tag{3}$$

Therefore the dispersion relation will be:

$$-k^2 + \varepsilon(\omega)\varepsilon_0\mu_0\omega^2 = 0 \tag{4}$$

$$-\frac{k^2}{\varepsilon_0\mu_0} + \left(\omega^2 - \omega_p^2\right) = 0$$

$$\omega^2 = \omega_p^2 + c^2k^2 \tag{5}$$

The dispersion relation is depicted in Figure 12.

To obtain the dispersion relation of non-radiative SPW, which is the mode utilized in SPR biosensors, let us look at the interface of a metal and a dielectric, and assume an imaginary z wavevector, such that the wave decays as it moves away from the interface. If we write down a solution of TM- wave or p-polarized wave:

$$H_y = \text{const}_1 \exp\left(i\left(k_{x1}x - \omega t\right)\right)\exp\left(-\kappa_{z1}z\right), \quad \text{for } z > 0$$

$$H_y = \text{const}_2 \exp\left(i\left(k_{x2}x - \omega t\right)\right)\exp\left(\kappa_{z2}z\right), \quad \text{for } z < 0\,, \tag{6}$$

where

$-k_x^2 + \kappa_z^2 + \mu\varepsilon\omega^2 = 0$, or

$$\kappa_z^2 = k_x^2 - \varepsilon\omega^2 / c^2 = 0 \tag{7}$$

Also from

$$\nabla \times \vec{H} = \vec{J} + \frac{\partial \vec{D}}{\partial t} \tag{8}$$

$$\nabla \times \vec{H} = -i\omega\varepsilon\vec{E} \tag{9}$$

$$\vec{E} = -\frac{1}{i\omega\varepsilon}\nabla\times\vec{H} = -\frac{1}{i\omega\varepsilon}\left[-\frac{\partial H_y}{\partial z}\hat{x} + \frac{\partial H_y}{\partial x}\hat{z}\right] \tag{10}$$

We can write down the expressions for the electric field components:

$$E_x = -\frac{\kappa_{z1}}{i\omega\varepsilon_1}\text{const}_1 \exp\left(i\left(k_{x1}x - \omega t\right)\right)\exp\left(-\kappa_{z1}z\right), \quad \text{for } z > 0$$

$$E_x = -\frac{\kappa_{z2}}{i\omega\varepsilon_2}\text{const}_2 \exp\left(i\left(k_{x2}x - \omega t\right)\right)\exp\left(-\kappa_{z2}z\right), \quad \text{for } z > 0 \tag{11}$$

$$E_z = -\frac{k_{x1}}{\omega\varepsilon_1}\text{const}_1 \exp\left(i\left(k_{x1}x - \omega t\right)\right)\exp\left(-\kappa_{z1}z\right), \quad \text{for } z > 0$$

$$E_z = -\frac{k_{x2}}{\omega\varepsilon_2}\text{const}_2 \exp\left(i\left(k_{x2}x - \omega t\right)\right)\exp\left(-\kappa_{z2}z\right), \quad \text{for } z < 0 \tag{12}$$

Applying the boundary conditions, i.e., requires the tangential components of the electric field and the magnetic field to be continuous at $z = 0$, we obtain:

$$-\frac{\kappa_{z1}}{\varepsilon_1} = \frac{\kappa_{z2}}{\varepsilon_2} \tag{13}$$

And, $\text{const}_1 = \text{const}_2$, and $k_{x1} = k_{x2} = k$, where we have omitted the subscript x. k is the wavevector of the excited SPW.

Since both κ_{z1} and κ_{z2} are positive, then ε_1 and ε_2 should be of opposite signs for the solution to exist. Let us assume medium 1 is a dielectric and medium 2 is a metal whose dielectric constant as given by Drude model is negative for frequencies lower than the plasma frequency, such that $\varepsilon_1 > 0$ and $\varepsilon_2 < 0$.

$$\varepsilon_1\left(k^2 - \varepsilon_2\frac{\omega^2}{c^2}\right)^{1/2} = -\varepsilon_2\left(k^2 - \varepsilon_1\frac{\omega^2}{c^2}\right)^{1/2} \tag{14}$$

Rearranging for ω expression,

$$\omega^2 = c^2 k^2 \frac{\varepsilon_1 \varepsilon_2}{\varepsilon_1 + \varepsilon_2} \tag{15}$$

The dispersion relation for non-radiative SPW is depicted in Figure 12. We see that the requirement for the solution to exist is not only $\varepsilon_2 < 0$, but moreover – $\varepsilon_2 > \varepsilon_1$.

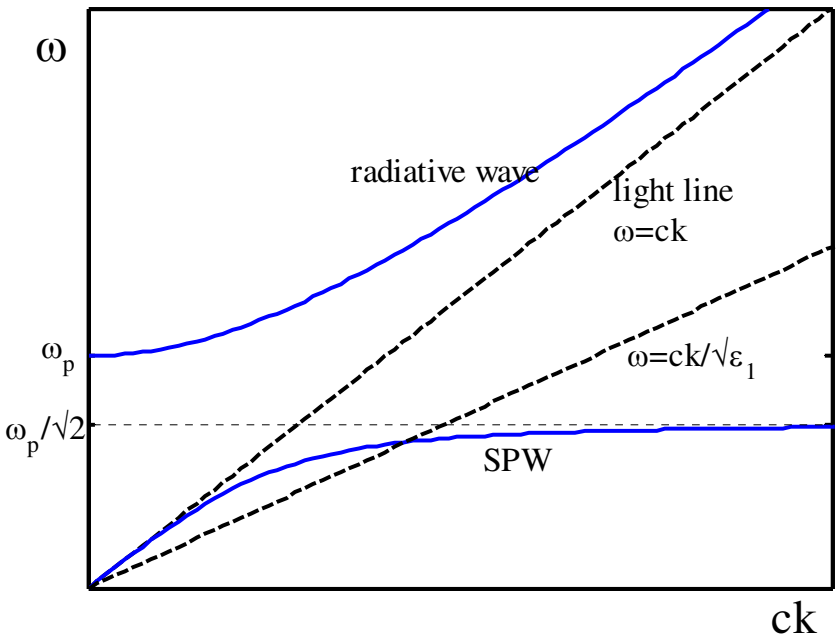

Figure 12 Dispersion relations of radiative plasmon wave and surface plasmon wave, also shown in dash are the light line in air and in glass prism medium having refractive index of $\sqrt{\varepsilon_1}$.

If we had written down a TE-wave or s-polarized solution, we would have ended up with:

$$\frac{\kappa_{z1}}{\mu_1} = -\frac{\kappa_{z2}}{\mu_2} \tag{16}$$

The solution exists only if the magnetic permeability can be negative. Unless the metal is replaced by a left-handed material [24] ,whose ε and μ are both negative, s-polarized SPW cannot exist.

From Figure 12, we see that the radiative plasmon wave can be excited directly by an incoming light, by having the light shine obliquely to the metal such that the wavevector is reduced by sin(θ). But non-radiative SPW cannot be excited directly because the wavevector of the incoming light is always shorter than that of the plasmon mode. Clever schemes to match the wavevectors utilize grating and prism. Corrugated metal surface can serve as a grating to increase the wavevector of the incident light by integer multiples of $2\pi/a$, where a is the corrugation constant. For a particular a, and a specific wavelength, SPW can be excited if the incident angle yields a matching SPW wavevector. In the case of prism method or attenuated total reflection (ATR) method, the metal is bounded by two different dielectrics. An incident light from medium 1 is able to excite a non-radiative SPW on the interface of metal and medium 2, because there are wavevectors of SPWs in metal-medium 2 interface that are shorter than those of the incident light. The tangential component of the wavevector of an incident light with frequency ω falling on the base of the prism at an angle θ is:

$$k_x = \sqrt{\varepsilon_1}(\omega / c)\sin(\theta). \qquad (17)$$

Because $\sqrt{\varepsilon_1}\cdot\sin(\theta) > 1$, an inhomogeneous wave propagates along the base with a phase velocity ω/k_x smaller than that of light. However, a dielectric in general is never lossless, therefore k_x may have an imaginary component, so the wave cannot propagate indefinitely. The plasma or metal film can now be positioned either in Otto

configuration or Kretschmann configuration. In Otto configuration the metal is placed at a distance comparable to the wavelength of light from the base of the prism. The inhomogeneous wave decays exponentially into this air gap and excites the SPW on the air-metal boundary. In Kretchsmann configuration, the metal is placed directly on the base of the prism. The inhomogeneous wave has to penetrate the metal to excite SPW on the metal-air boundary.

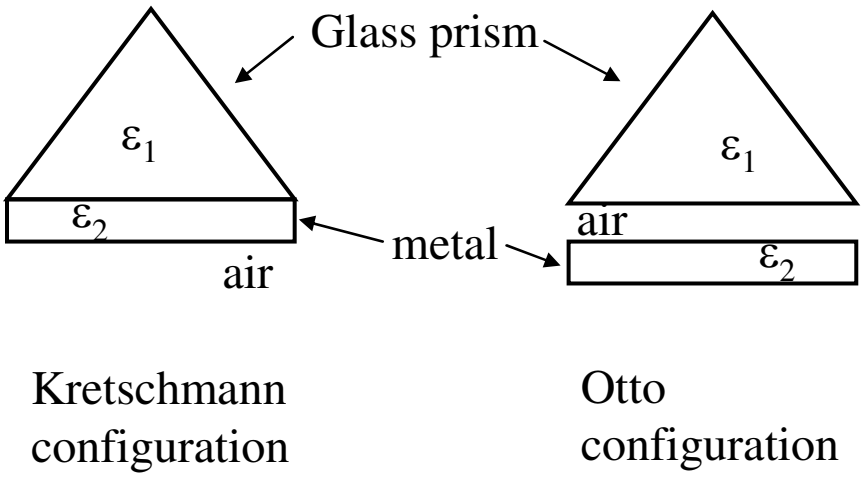

Figure 13 SPW excitation configuration: Kretschmann (left) and Otto (right) configurations.

3.5.1.2. The configuration of SPR sensors

From the above discussion, it is clear that the change in dielectric constant or refractive index ($n = \sqrt{\varepsilon}$) due to binding events of biomolecules on the surface leads to the change in resonant condition dictated by the dispersion relation. Most SPR sensors utilized the ATR method in prism configuration to achieve wavevector

matching. Kretschmann configuration is preferred due to ease of fabrication. To detect the change in refractive index, three major detection approaches have been widely used in prism-based SPR sensors: intensity measurement near the resonant wavelength; incident angle measurement while using a fixed wavelength; wavelength measurement while using a fixed incident angle. SPR sensors using grating couplers have also been demonstrated. Unlike prism-based system, grating-based SPR systems require the sample solution to be optically transparent enough for the incident beam to pass through. The review article by Homola et al. [25] and the references therein provide a relatively complete survey of various configurations of SPR sensors. These configurations include SPR sensors with integrated optical fibers and SPR sensors with integrated optical waveguides. Reported sensitivity varies widely depending on the system and instrumentation, and ranges from 5e-7 to 1e-5 refractive index unit (RIU).

SPR sensors utilizing ATR has been available commercially by BIAcore AB, and Texas Instruments (Spreeta™).

3.5.1.3. Sensitivity for bio-detection

Due to the fast response of SPR sensors they are capable of rapid and real-time analyses and acquisition of kinetic parameters such as dissociation and association constants and thermodynamic information. SPR biosensors can be used to study DNA hybridization, DNA-protein interactions and DNA-drug interactions. Although SPR is very sensitive to tiny changes in refractive index, the refractive index of the analyte does not change much upon target molecule binding because the refractive index of the buffer solution is already comparable to that of the target molecule. Nevertheless, direct assay detection of 10 nM target DNA oligonucleotide

was achieved [26]. Signal amplification through gold nanoparticle labeled DNA has been shown to be capable of sub-attomolar detection [27]. To conclude, the pros and cons of SPR biosensors are: pros, real-time assay is possible; cons, limited detection level in direct assays.

3.5.2. Refractive index and thickness: Ellipsometry

Ellipsometry is a technique to measure the refractive index and the thickness of a thin film. Due to the difference in reflection coefficient for different light polarization given by Fresnel equation, the reflected light will have a rotated polarization from the incoming light. From the amount of rotation, thickness and refractive index of the thin film can be deduced. Biodetection using ellipsometry generally depends on the thickness change upon target binding. However, it generally requires a large amount of target to induce thickness change. It is thus more suited for protein detection rather than DNA detection since protein molecules are inherently larger. Recently detection of herring DNA and salmon DNA was demonstrated using combined spectroscopic ellipsometry and SPR in total internal reflection configuration [28].

3.5.3. Vibrational mode resonance: THz-transmission analysis

Resonance in the terahertz (THz) frequency range associated with vibrational modes such as base twisting helix structure of the DNA molecule, which is reflected in the complex refractive index can in principle be detected using THz transmission analysis. Detection of the binding state (hybridized or denatured) of 5.4 kilo-basepair of vector DNA has been demonstrated using time-domain THz sensing [29]. The

drawbacks are requirement for dried or crystallized samples as humidity is known to drastically affect the refractive index in THz range, and requirement for large sample to generate enough resonant signal.

3.5.4. Dielectric constant: Capacitance measurement

The DNA hybridization detection using capacitance measurement exploits the fact that adsorption of a layer of target DNA, itself an insulating dielectric, decreases the capacitance due to the increase in distance between the charges in the polarized electrode and the ions in the electrolyte. The ions in the solution are pushed further away from the electrode upon formation of DNA duplex. A charging current will flow between the DNA functionalized electrode and an auxiliary electrode of the electrochemical cell when they are excited by a voltage step. The principle behind charge based capacitance measurement is to integrate the charging current, responding to a voltage step excitation, over one period. The result of charging current integration is essentially the charge on the capacitor, and the capacitance can be obtained by dividing this charge with the magnitude of the voltage step. The measured capacitance is basically the capacitive component of the total impedance, or C_{dl} in Figure 8, assuming negligible faradaic process occurs. It is obvious that the decrease in capacitance upon biomolecule adsorption would be more pronounced if the sensing area is larger. A detection level of 3μM of 26-mer DNA oligonucleotide has been shown [30], corresponding to a change in capacitance from 3 μF to 2 μF on 100 mm^2 sensing area.

3.6. Label-free (2): gravimetric

Acoustic waves are waves of stress and strain fields propagating in solids. Acoustic wave devices always involve piezoelectric crystals, since the electric field and the acoustic field are coupled in piezo materials. The analysis of acoustic wave is far more complicated than that of electromagnetic wave, because of the anisotropic nature of the crystal. Analogous to electromagnetic waves, there are many different modes of acoustic waves can be excited. The criteria to excite a certain mode depend on the boundary conditions, and certainly the mechanical properties of the solid, such as stiffness, elasticity etc.

One of the most widely used acoustic mode for sensor is the thickness shear mode, which is a bulk acoustic wave (BAW), i.e. the wave propagates through the crystal. It is the mode utilized in quartz crystal microbalance (QCM), which finds application in thickness monitor in thin film deposition. The relationship between the shift in resonant frequency upon adsorption of material or addition of mass onto the crystal is given by Sauerbrey [31]:

$$\Delta f = -\frac{2 f_0^2 \Delta m}{A\sqrt{\rho_q t_q}} \tag{18}$$

where f_o is the natural resonant frequency of the crystal, A is the area of the crystal, ρ_q is the density and t_q is the thickness of the crystal.

As can be seen in the above relation, the sensitivity would increase if the natural resonant frequency f_o is increased. However, higher f_o requires thinner crystal, and the brittleness of the crystal would practically set a lower limit of the usable thickness. Sullivan et al. [32]compiled a comparison of several commercial QCMs. f_o of

5 MHz and 10 MHz are commonly encountered, which yield sensitivity of ~ 1 ng/cm^2. Storri et al. [33] demonstrated sensitivity of 0.5 μM 23-mer DNA oligonucleotide hybridization using QCM.

A surface acoustic wave (SAW), which propagates only on the surface of the crystal may oscillate at several hundred MHz, and thus allows higher sensitivity. For a thin layer of analyte, the frequency change in BAW resonators is exactly proportional to the relative mass load, but the frequency change in SAW resonator depends on the mass load as well as other elastic constants. Hence the behavior of SAW resonator is even more difficult to model. Guided shear horizontal surface acoustic wave (SH-SAW) devices on $LiTaO_3$ has been demonstrated. The device consists of an interdigital transducer to generate an acoustic wave; a sensing layer, serving as the waveguide for the acoustic wave, and another interdigital transducer to detect the wave. As the part of the crystal underneath the waveguide is electrically shorted the velocity of the wave propagating underneath the waveguide is much less than the surrounding. It is well-known that if a region with low wave velocity is surrounded by faster regions, the wave is confined in the slower region. The transfer function of the device is proportional to $\exp(2\pi i(\Delta V/V)l_s/\lambda)$, where l_s is the length of the sensing layer or the waveguide, λ is the wavelength and $\Delta V/V$ is the fractional change in the wave velocity, which is given by:

$$\frac{\Delta V}{V} = -\frac{V_{SH}}{4}(\rho h)\left[1-\left(\frac{V_M}{V_{SH}}\right)^2\right]|U_2|^2, \qquad (19)$$

Where V_{SH} is the wave velocity in the substrate, V_M is the shear wave velocity in the sensing layer, ρ is the layer mass density, h is the layer thickness and U_2 is the

normalized particle velocity displacement amplitude at the surface, ρh represents the mass load per unit surface area. From the transfer function proportionality, one can also detect the frequency shift as a result of fractional change in the wave velocity due to mass loading. Hur et al. [34] projected a sensitivity of 1.55 ng/ml/Hz, and showed detection of 0.1μM or 0.46 μg/ml of 15-mer oligonucleotide.

3.7. Label-free (3): field-effect

Many biomolecules are ionized in solution and thus one can measure the charges they carry. Their existence can be detected by sensing the electric field generated by the charged biomolecules. In particular, each phosphate group that comprises the backbone of the DNA is ionized to carry one negative electronic charge. In general, many field effect based biomolecule detection schemes resemble the structure of ISFET (ion sensitive field effect transistor), which was first introduced by Bergveld in 1970 [35]. ISFET is similar to the conventional MOSFET (metal oxide semiconductor field effect transistor), except that the metal layer is replaced by an electrochemical reference electrode in contact with the electrolyte solution, in which the target molecules to be detected are dissolved. The drain-source current is modulated by the field-effect from the ions or molecules reaching the oxide. ISFET technology has been so well-developed, that it has made its way to the market as pH meters. The effect, which is proportional to the amount of charges adsorbed on the oxide, is essentially the flat-band voltage shift that can be measured by capacitance-voltage (CV) measurement of a MOS diode, or I_{DS}-V_{GS} transfer characteristic measurement of a MOSFET. The working principle will be described in

details in later chapter. Souteyrand et al. [36] is the first to demonstrate label-free homo-oligomer DNA (18-mer and 1000-mer of poly(dA) DNA) hybridization detection using silicon ISFET. Since then, numerous works using various materials to build the transistors emerge, and are summarized in the following table (Table 1).

There are two major factors to consider when looking at FET designs: (i) electric field distribution as one goes from 2D planar structures to novel 1D structures, such as silicon nanowires and carbon nanotubes; (ii) contact resistance at source and drain, as one leaves silicon technology and goes to new materials and novel nanostructures. As one goes from conventional silicon transistor to new 1D materials and nanostructures the transistor design has the advantage of electric field enhancement, shown in Figure 14. We can see qualitatively how the field lines are more condensed close to the 1D transistor channel, and the electric field distribution can easily be disturbed by local distribution of charges on the transistor gate. Therefore one may expect larger voltage shift or signal in 1D transistors than that in 2D planar transistors. But on the other hand the amount of shift is probably more unpredictable as the distribution of charges from the biomolecules cannot be controlled experimentally. Second, due to work function differences between the channel material and source-drain material there is always contact resistance or Schottky barrier in carbon nanotube transistors. However, it is well-known that the Schottky barrier thickness in a thin-film transistor is comparable to thickness of the body and not the doping of the body. And the body of single wall carbon nanotube is only one atomic layer, therefore the Schottky barrier thickness in the source-channel junction is also in the order of atomic distance, well within the regime of tunneling. It

is therefore theoretically still possible to control the contact resistance distribution in carbon nanotube transistor devices if one is able to control the size of carbon nanotube grown on the substrate.

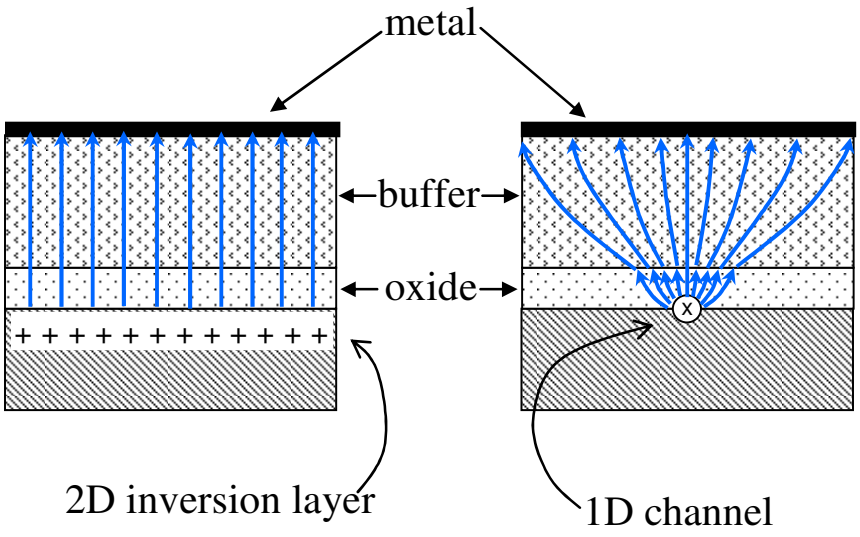

Figure 14 Illustration of electric field enhancement in 1D channel transistor as opposed to 2D planar transistor. The electric field is represented by the density of the field lines, shown in blue arrows.

Field effect devices	Mechanism	Sensitivity demonstrated	Note
MOS diode	Change in depletion width upon charged biomolecules adsorption	1 μM of poly(dA)20 [37]	2D planar structure
Silicon FET	Change in surface potential or flat-band potential in the transistors	1 mg/mL of poly(dA)18 [36]; 50 μM of 20-mer DNA	2D planar structure

		oligonucleotide [38]; 100 ng/mL of 19-mer DNA oligonucleotide [39]	
Polysilicon TFT	Change in surface potential or flat-band potential in the transistors	1 mM of penicillin G[40]	2D planar structure
Suspended gate silicon TFT	Change in surface potential or flat-band potential in the transistors	5 nM of 24-mer DNA oligonucleotide [41]	2D planar structure. Author [41] suggested, small gate gap enhances electric field and thus increases its sensitivity compared to conventional FET.
Silicon nanowire transistors	Conductance change	10 fM of wild-type DNA [42]	1D structure, application of gate voltage is not clearly indicated in the paper [42]
Carbon nanotube transistors	Change in surface potential or flat-band potential in the transistors	100 pM [43]	1D structure, CNT is directly functionalized with probe [43], target may stick also to uncovered CNT, compromising selectivity.
Carbon nanotube transistors (this work)	Change in surface potential or flat-band potential in the transistors	100 nM of 61-mer DNA oligonucleotide	1D structure, CNT only serves as charge sensor. All attachment chemistry is done on the oxide layer covering the CNT channel, thereby selectivity is comparable to other conventional glass-slide protocols

Table 1 Sensitivity comparison among field effect devices for biosensing application.

3.8. Summary of comparisons

We will carefully compare the pros and cons among the label free techniques:

Label-free techniques	Sensitivity and selectivity	Advantages	Limitations	Maturity and manufactura-bility
SPR	10 nM, attomolar sensitivity demonstrated using signal amplification through gold particle labeling;	Real-time monitoring is possible.	Refractive index of surrounding buffer is comparable to that needs to be detected, thus is difficult to improve signal to noise; Probe attachment is done on gold film, presents different protocols from those used in conventional glass-slide assays.	Commercial products are available, e.g. Biacore™, Spreeta™; Works toward miniaturization are in progress.
Ellipsometry		Real-time monitoring is possible	Requires large sample to induce thickness change	Research is ongoing.
THz time domain spectroscopy		Molecule vibration ,coiling structure can probably be studied	Requires large amount of sample, and drying of sample; Protocol is not compatible at all.	Research is ongoing.
Capacitance measurement	3 μM	Very simple device structure, and simple measurement system.	Signal is proportional to device area, thus is difficult to down scale the size.	Research is ongoing
Gravimetric/ BAW/ SAW devices	0.5 μM (using QCM); 0.1 μM (using SH-SAW)	Real-time monitoring is possible	Protocols may/may not be compatible, since probes need to be attached to piezo-crystal; Some acoustic modes are not compatible with liquid due to the tremendous damping.	SAW device technology itself is very mature, every cell phones would contain some form of SAW device. However,

				operating modes of certain SAW devices are not completely understood yet.
Field-effect devices	nM ranges; (see Table 1 for more details); Selectivity is comparable to glass-slide assays except for those utilizing direct functionalization.	Simple device structure; size-scalable; Protocols are entirely compatible, except for those using direct functionalization strategies.	Real-time measurement not possible, unless charge-less PNA probes are used.	So far which FET design has the most potential is still not clear yet. However, Nanomix is targeting to launch carbon nanotube transistor based genechip.

Table 2 Comparison among available label-free techniques.

We see here that field effect transistors have great potential to become the dominant genechip technology, because of scalability, compatibility with existing protocols and potential to achieve the sensitivity level of current DNA microarrrays without labels or amplifications, and simple enough for low-cost and high-volume production.

Chapter 4: Carbon nanotube basics

In this chapter we will start with the discussion of the band structure of graphene, and understand how the boundary condition imposed by rolling a graphene sheet into a carbon nanotube gives rise to the electronic properties of carbon nanotubes. The resulting carbon nanotube can either be metallic or semiconducting, depending on how it is rolled-up. The growth of carbon nanotubes used in our experiment is then discussed. And finally the transport or switching mechanism of the carbon nanotube field-effect transistor is presented.

4.1. Structure of a graphene sheet

It is helpful to think of the structure of a carbon nanotube as a hollow cylinder of a rolled-up 2D graphene sheet. In a graphene sheet, three outer-shell electrons of each carbon atom occupy the planar sp^2 hybrid orbital to form three in-plane σ bonds with an out-of-plane π orbital (bond) [44]. A graphene sheet, thus, has a hexagonal lattice structure as shown in Figure 15. The σ bond is 0.14 nm, which is the average distance between two in-plane carbon atoms. The π bond is 0.34 nm long, and is delocalized, contributing to the electrical conductivity of the graphene sheet.

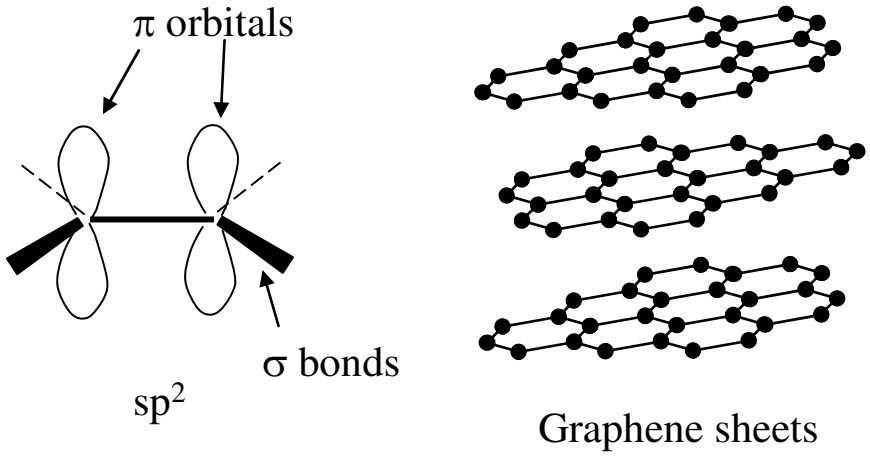

Figure 15 Illustration of sp^2 orbitals in the carbon bonds of graphene sheets.

The hexagonal structure is not really periodic, since adjacent carbon atoms do not have identical environments. But if two atoms are grouped together into a unit cell than the lattice of the unit cells is periodic, i.e. forming a Bravais lattice. In Figure 16, $\hat{a}_1$ and $\hat{a}_2$ are the primitive vectors of this Bravais lattice. We can construct its reciprocal lattice, and calculate the tight binding band structure. In a tight-binding approximation, the wavefunction satisfying the crystal Hamiltonian is approximated to be a linear combination of the orbitals of isolated atoms. The linear combination includes all orbitals of the atoms within the Bravais unit cell. Each carbon atom in the graphene sheet has four valence orbitals: $2s$, $2p_x$, $2p_y$, and $2p_z$. Since only the π bond or $2p_z$ orbital participate in the electrical conduction, The tight-binding wavefunction only needs to include two terms, i.e. one orbital from each atom in the unit cell, rather than eight terms, i.e. four orbitals from each atom in the

unit cell. Following the treatment described in standard textbook [45], we can write the crystal Hamitonian as:

$$H = H_{at} + \Delta U \,, \tag{20}$$

where H_{at} is the Hamiltonian of isolated atoms and ΔU contains all corrections to the atomic potential required to produce the full periodic potential of the crystal. The wavefunction that satisfies

$$H\psi = \left(H_{at} + \Delta U\right)\psi = E\psi \tag{21}$$

can be written as:

$$\psi(r) = \sum_{\vec{R}} e^{i\vec{k}\cdot\vec{R}}\phi\left(\vec{r} - \vec{R}\right) \tag{22}$$

$\phi\left(\vec{r} - \vec{R}\right)$ contains the orbitals within the unit cell, and as discussed before, it only needs to include two terms, so we can write:

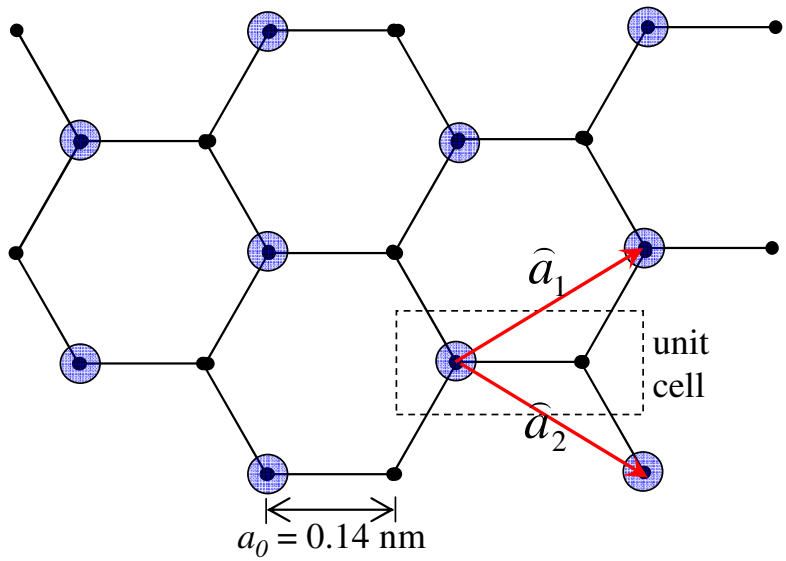

Figure 16 Hexagonal lattice structure of the carbon atoms in a graphene sheet. The Bravais unit cell is shown in a dashed rectangular box, which contains two atoms. The lattice points circled in blue show the periodicity of the unit cells. The primitive vectors are: $\hat{a}_1 = 3a_0/2\hat{x} + \sqrt{3}a_0/2\hat{y}$, and $\hat{a}_1 = 3a_0/2\hat{x} - \sqrt{3}a_0/2\hat{y}$

$$\phi\left(\vec{r}-\vec{R}\right)=b_1\phi_1+b_2\phi_2 \tag{23}$$

Substituting (23) to (22) yields

$$\psi(r)=\sum_{\vec{R}} e^{i\vec{k}\cdot\vec{R}}\left(b_1\phi_1\left(\vec{r}-\vec{R}\right)+b_2\phi_2\left(\vec{r}-\vec{R}\right)\right) \tag{24}$$

If we operate $\left\langle\phi_1\left(\vec{r}\right)\right|$ from the left to (21), then

$$\left\langle\phi_1\left|H_{at}\right|\psi\right\rangle+\left\langle\phi_1\left|\Delta U\right|\psi\right\rangle=E\left\langle\phi_1\left|\psi\right\rangle\right.=Eb_1 \tag{25}$$

$$\left\langle\phi_1\left|H_{at}\right|\psi\right\rangle=\left\langle H_{at}^{+}\phi_1\left|\psi\right\rangle\right.=E_1\left\langle\phi_1\left|\psi\right\rangle\right.=E_1b_1 \tag{26}$$

$$\left(E-E_1\right)b_1=\left\langle\phi_1\left|\Delta U\right|\psi\right\rangle \tag{27}$$

$$\begin{aligned}\left\langle\phi_1\left|\Delta U\right|\psi\right\rangle=&\,b_1\left(-\beta_1\right)+b_2\left\langle\phi_1\left|\Delta U\right|\phi_2\right\rangle+\\&\sum_{\vec{R}\neq 0}e^{i\vec{k}\cdot\vec{R}}\left(b_1\left\langle\phi_1\left(\vec{r}\right)\right|\Delta U\left|\phi_1\left(\vec{r}-\vec{R}\right)\right\rangle+b_2\left\langle\phi_1\left(\vec{r}\right)\right|\Delta U\left|\phi_2\left(\vec{r}-\vec{R}\right)\right\rangle\right)\end{aligned} \tag{28}$$

where $-\beta_1=\left\langle\phi_1\left|\Delta U\right|\phi_1\right\rangle$

Ignoring all the overlap integrals except those between two nearest neighbors as $-\gamma$ yields:

$$\begin{aligned}\left\langle\phi_1\left|\Delta U\right|\psi\right\rangle=&-\beta_1b_1+-b_2\left\langle\phi_1\left(\vec{r}\right)\right|\Delta U\left|\phi_2\left(\vec{r}\right)\right\rangle+\\&e^{-i\vec{k}\cdot\vec{a}_1}\left(b_1\left\langle\phi_1\left(\vec{r}\right)\right|\Delta U\left|\phi_1\left(\vec{r}+\vec{a}_1\right)\right\rangle+b_2\left\langle\phi_1\left(\vec{r}\right)\right|\Delta U\left|\phi_2\left(\vec{r}+\vec{a}_1\right)\right\rangle\right)+\\&e^{i\vec{k}\cdot\vec{a}_1}\left(b_1\left\langle\phi_1\left(\vec{r}\right)\right|\Delta U\left|\phi_1\left(\vec{r}-\vec{a}_1\right)\right\rangle+b_2\left\langle\phi_1\left(\vec{r}\right)\right|\Delta U\left|\phi_2\left(\vec{r}-\vec{a}_1\right)\right\rangle\right)+\\&e^{-i\vec{k}\cdot\vec{a}_2}\left(b_1\left\langle\phi_1\left(\vec{r}\right)\right|\Delta U\left|\phi_1\left(\vec{r}+\vec{a}_2\right)\right\rangle+b_2\left\langle\phi_1\left(\vec{r}\right)\right|\Delta U\left|\phi_2\left(\vec{r}+\vec{a}_2\right)\right\rangle\right)+\\&e^{i\vec{k}\cdot\vec{a}_1}\left(b_1\left\langle\phi_1\left(\vec{r}\right)\right|\Delta U\left|\phi_1\left(\vec{r}-\vec{a}_2\right)\right\rangle+b_2\left\langle\phi_1\left(\vec{r}\right)\right|\Delta U\left|\phi_2\left(\vec{r}-\vec{a}_2\right)\right\rangle\right)\end{aligned} \tag{29}$$

$$\begin{aligned}-\gamma&=\left\langle\phi_1\left(\vec{r}\right)\right|\Delta U\left|\phi_2\left(\vec{r}\right)\right\rangle\\&=\left\langle\phi_1\left(\vec{r}\right)\right|\Delta U\left|\phi_2\left(\vec{r}+\vec{a}_1\right)\right\rangle\\&=\left\langle\phi_1\left(\vec{r}\right)\right|\Delta U\left|\phi_2\left(\vec{r}+\vec{a}_2\right)\right\rangle\end{aligned} \tag{30}$$

$$\left\langle\phi_1\left|\Delta U\right|\psi\right\rangle=-\beta_1b_1-\gamma b_2-\gamma e^{-i\vec{k}\cdot\vec{a}_1}b_2-\gamma e^{-i\vec{k}\cdot\vec{a}_2}b_2 \tag{31}$$

Therefore (25) becomes

$$Eb_1=\left(E_1-\beta_1\right)b_1-\gamma b_2-\gamma e^{-i\vec{k}\cdot\vec{a}_1}b_2-\gamma e^{-i\vec{k}\cdot\vec{a}_2}b_2 \tag{32}$$

Likewise if we operate $\left\langle\phi_2\left(\vec{r}\right)\right|$ from the left to (21), then we will obtain

$$Eb_2 = -\gamma b_1 - \gamma e^{i\vec{k}\cdot\vec{a}_1} b_1 - \gamma e^{i\vec{k}\cdot\vec{a}_2} b_1 + (E_2 - \beta_2) b_2 \qquad (33)$$

For simplicity, we can put E_1-β_1 = E_2-β_2= E_0. Combining (32) and (33), we can construct the following matrix:

$$\begin{bmatrix} E_0 & -\gamma\left(1 + e^{-ik\cdot\vec{a}_1} + e^{-ik\cdot\vec{a}_2}\right) \\ -\gamma\left(1 + e^{ik\cdot\vec{a}_1} + e^{ik\cdot\vec{a}_2}\right) & E_0 \end{bmatrix} \begin{bmatrix} b_1 \\ b_2 \end{bmatrix} = E \begin{bmatrix} b_1 \\ b_2 \end{bmatrix} \qquad (34)$$

to solve for the eigen energy:

$$E = E_0 \pm \gamma \sqrt{1 + 4\cos\left(\sqrt{3}k_y a_0 / 2\right)\cos\left(3k_x a_0 / 2\right) + 4\cos^2\left(\sqrt{3}k_y a_0 / 2\right)}, \qquad (35)$$

where a_0 is the distance between two carbon atoms. This result was first derived by P. R. Wallace in 1947. [46] The band structure is plotted in Figure 17.

In Figure 17 one sees that there are two energy bands participating in the transport. Since each unit cell has two basis functions, the total number of states is 2 (spin) x 2 (atoms per basis) x N = 4N, where N is the number of unit cells. Each carbon atom provides one electron, giving a total of $2N$ electrons in the system. So the electrons will fill up half of the number of the states. This means that the electrons will fill up all of the states in the valence band up to $E = E_0$. Or in another word E_0 is the Fermi energy of the system. There are 6 points in the valence band that reach $E = E_0$:

$$\left(0, \frac{2\pi}{3b}\right); \left(-\frac{\pi}{a}, -\frac{\pi}{3b}\right); \left(\frac{\pi}{a}, -\frac{\pi}{3b}\right)$$
$$\left(0, -\frac{2\pi}{3b}\right); \left(-\frac{\pi}{a}, \frac{\pi}{3b}\right); \left(\frac{\pi}{a}, \frac{\pi}{3b}\right)$$

where $a = 3a_0 / 2$ and $b = \sqrt{3}a_0 / 2$. At these six wavevectors, the energy of the conduction band is also $E = E_0$ (the Fermi point), therefore the two bands coincide each other, forming zero bandgap. These six wavevectors can actually be grouped

into only two groups. Within each group, one can reach a second wavevector by translation of the primitive vector, $\hat{A}_1$ and $\hat{A}_2$, in reciprocal space. Therefore three points in each group are essentially equivalent to each other.

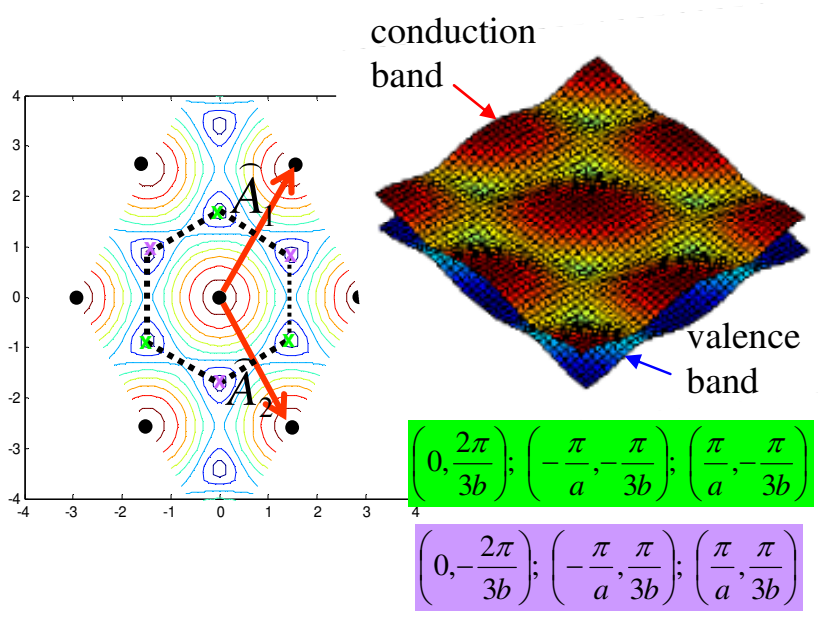

Figure 17 (left) Contour plot of the band structure in the reciprocal space. The area within the dashed hexagonal is the first Brillouin zone. $\hat{A}_1$ and $\hat{A}_2$ are the primitive vectors in the reciprocal lattice. (right) Tightbinding band structure of a graphene sheet. The two groups of six wavevector, at which the conduction and valence bands coincide are shown in green and purple boxes, with respective colors marked on the left figure as well.

4.2. Electronic properties of carbon nanotube

Carbon nanotubes are hollow cylinders composed of one or more concentric layers of carbon atoms. The following discussion assumes the carbon nanotubes are single walled. Unlike single-wall carbon nanotube, the electronic properties of multi-wall carbon nanotubes are not well studied, due to their complex structure. However, at low bias and when multi-wall carbon nanotubes were contacted to metal electrodes to form transistors, the carrier transport is dominated by outer shell conduction [47]. Rolling a graphene sheet means that we define a rolling vector such that a point in direct lattice will hit itself upon translation along that rolling vector:

$$\vec{c} = m\hat{a}_1 + n\hat{a}_2 = m(a\hat{x} + b\hat{y}) + n(a\hat{x} - b\hat{y}) \tag{36}$$

This imposes a boundary condition that will pick only certain wavevectors from the 2D graphene sheets that are allowed in the rolled up carbon nanotube.

$$\vec{k} \cdot \vec{c} = k_x a(m+n) + k_y b(m+n) = 2\pi\upsilon\,, \tag{37}$$

where all m,n,ν are arbitrary integers.

We would like to know what is the chance that those 6 zero bandgap wavevectors (Fermi points) will be allowed by this boundary condition, if one to pick an arbitrary rolling vector, $\vec{c}$, or the resulting carbon nanotube will exhibit metallic property. Substituting $\vec{k} = (0, \pm 2\pi / 3b)$ into (37), we arrive at the following expression:

$$(m-n)/3 = \upsilon \tag{38}$$

Since the integers are arbitrary, so one would most likely expect 1/3 of metallic tubes and 2/3 of semiconducting tubes from random growth of carbon nanotubes.

It has been shown that [48-50] the bandgap of a semiconducting carbon nanotube depends on its diameter:

$$E_{gap} = \frac{4\hbar v_F}{3d_{CNT}}, \tag{39}$$

where v_F is the Fermi velocity, and d_{CNT} is the diameter of the carbon nanotube. To get a feel of why the bandgap of semiconducting nanotubes, which depends on the chirality of the specific carbon nanotube, is inversely proportional to its diameter, we can first express the dispersion relation E - k, approximated by Taylor expansion around $E = E_0$, or $\vec{k} = (0, \pm 2\pi/3b)$ [51]:

$$E = \frac{3a_0}{2}\gamma\left(k_x^2 + \left(k_y - \frac{2\pi}{3b}\right)^2\right)^{1/2} \tag{40}$$

Then if we use the rolling vector of a zigzag nanotube,

$$\vec{c} = m(\hat{a}_1 - \hat{a}_2) = 2mb\hat{y}, \tag{41}$$

which by (37) leads to $k_y = 2\pi\upsilon/2mb$, which when substituted to (40) , we obtain

$$E_{gap} = E(k_x = 0) = \frac{3a_0}{2}\gamma\left(\frac{2\pi\upsilon}{2mb} - \frac{2\pi}{3b}\right) = \frac{3a_0}{2}\gamma\frac{2\pi}{2mb}\left(\upsilon - \frac{2m}{3}\right) \tag{42}$$

This has a minimum of zero, if $\upsilon = 2m/3$. But if m is not a multiple of three then the minimum value of $\upsilon - 2m/3$ is equal to 1/3. But the circumference $2mb$ is equal to πd, so the above expression can be simplified to be:

$$\therefore\ E_{gap} = \frac{3a_0}{2}\gamma\frac{2\pi}{\pi d}\left(\frac{1}{3}\right) = \frac{a_0\gamma}{d}, \tag{43}$$

which is inversely proportional to the diameter of the carbon nanotube.

4.3. Synthesis and growth

There are several methods known for growing carbon nanotubes: arc discharges [52], laser ablation [53], catalytic chemical vapor deposition [54]. In this experiment, we are using carbon nanotubes grown by chemical vapor deposition (CVD) in Prof. Fuhrer's lab. First, we evaporated sub-monolayer of iron film on a thermally oxidized silicon substrate in ultra high vacuum. This film will serve as the catalyst for the carbon nanotube growth. Upon heating in the CVD furnace, the iron film will ball up to form small iron particles, confirmed by my colleague, Konrad, who found the existence of iron particles on the substrate by atomic force microscope only after heat treatment. Initial attempts used ferric nitrate solution as the catalyst.

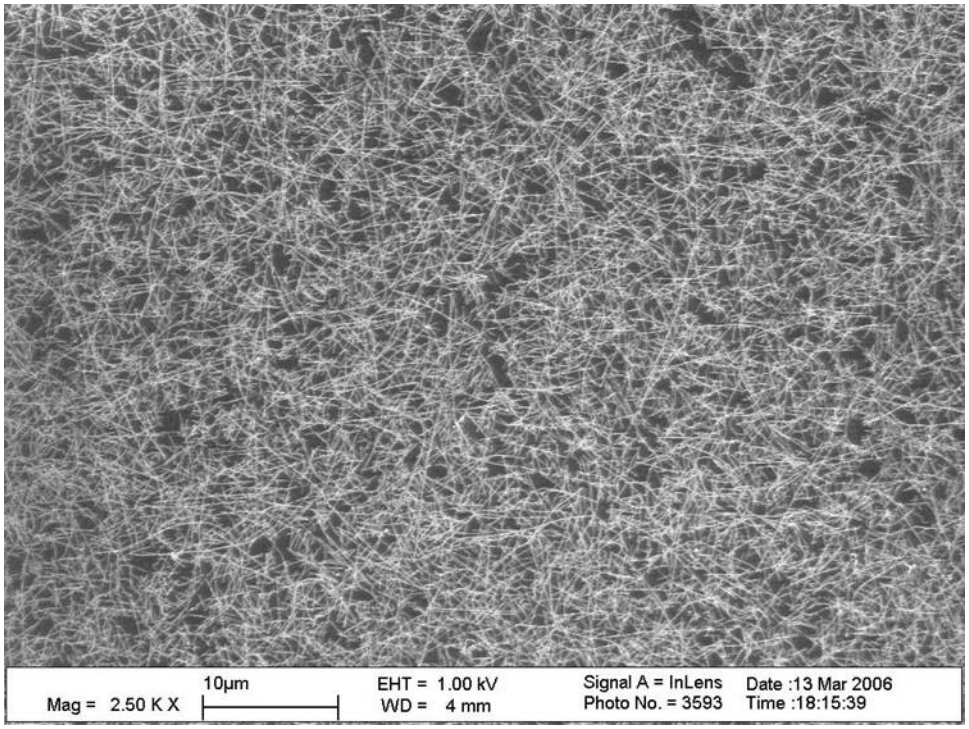

Figure 18 Scanning electron micrograph of the resulting carbon nanotube mats grown by catalytic chemical vapor deposition.

The solution was applied by dipping the substrate into the solution. The resulting carbon nanotubes tend to be denser at the edge of the substrate, due to lack of control of iron catalyst distribution. Therefore we opted to evaporate iron to obtain more uniformly distributed iron catalyst. To our knowledge, this is the first implementation of this approach using ultra high vacuum (UHV) iron evaporation.

Next, the substrate, containing sub-monolayer of iron film, was put in the CVD furnace. The temperature of CVD furnace was ramped up to 850 °C under argon flow. Then the argon was stopped, while the growth gas consisting of methane, ethylene, and hydrogen were flowed for 10 minutes, followed by temperature ramp down cyle. This process yields carbon nanotube mats on the substrate (Figure 18), whose density depends on the density of iron catalyst.

4.4. Carbon nanotube as field effect transistors

Having understood the electronic property band structure of carbon nanotubes, we will proceed to discuss the switching mechanisms or transport properties of the carbon nanotube (CNT) when being put in a field effect transistor (FET) configuration. It is as simple as depositing metal on both ends of CNTs to make CNTFETs. The gate can be applied from the back Si-substrate through the thermal oxide on which CNTs sit, or from the top after another oxide deposition on top of CNTs. A typical back-gated carbon nanotube field effect transistor (CNTFET) I_{DS}-V_{BS} transfer characteristics is shown in Figure 19. Despite strong resemblance in I_{DS}-V_{DS} plot (Figure 20) to that of silicon MOSFET, the switching mechanism of a CNTFET is different from that of a MOSFET. It has been shown [55] that the Schottky

barrier at the carbon nanotube and metal contact is responsible for a number of experimental observations that cannot be explained otherwise by the MOSFET mode, in which the drain-source current is determined by the carrier concentration modulation in the bulk of the transistor channel.

The transport properties of a CNTFET as a function of the gate voltage can be summarized as follow [56]: Due to its intrinsically high mobility [57, 58], the drain-source voltage drop almost entirely exists only at the source and drain interfaces forming Schottky barriers. The Schottky barrier is due to difference in work functions of the metal and the CNT. The channel conduction can occur through both the valence band (*p*-type conduction) and the conduction band (*n*-type conduction). For a given value of V_{DS}, increasing the gate voltage towards more negative values (*p*-type conduction) results in an exponential-like increase of I_{DS}, since the transmission probability for tunneling through the source Schottky barrier increases with decreasing barrier height and thickness. However, as the gate voltage is increased to reach the certain point such that the valence band of CNT coincides approximately with the Fermi level of the source electrode, charge starts to accumulate in the CNT. The movement of the bands, or equivalently the decrease of Schottky barrier thickness no longer changes as significantly as before, which leads to the saturation of I_{DS}. A similar situation happens for *n*-type conduction as the gate voltage is increased towards more positive values. This gives the ambipolar characteristic in the carbon nanotube transistor.

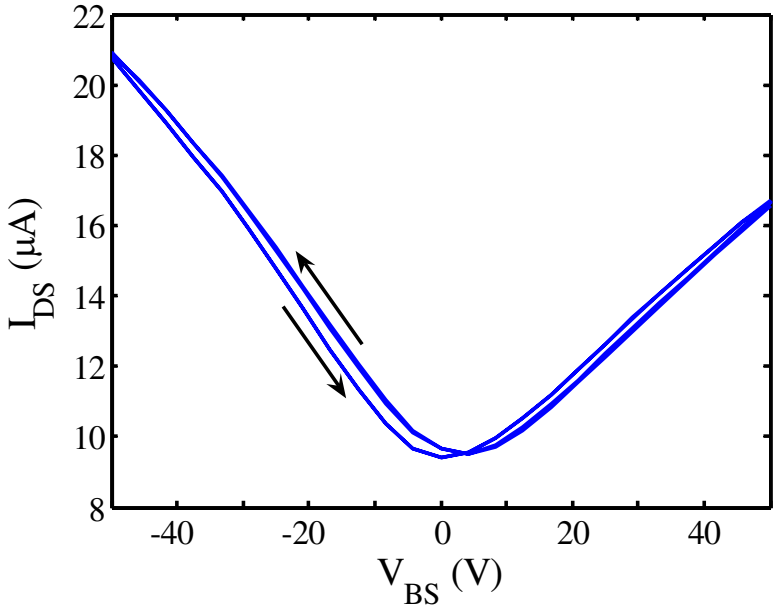

Figure 19 Back-gated transfer characteristic of Al_2O_3 passivated CNTFET (V_{DS} = 0.1 V). Two salient features are ambipolar characteristic, and much smaller hysteresis, compared to unprotected CNTFET characteristic.

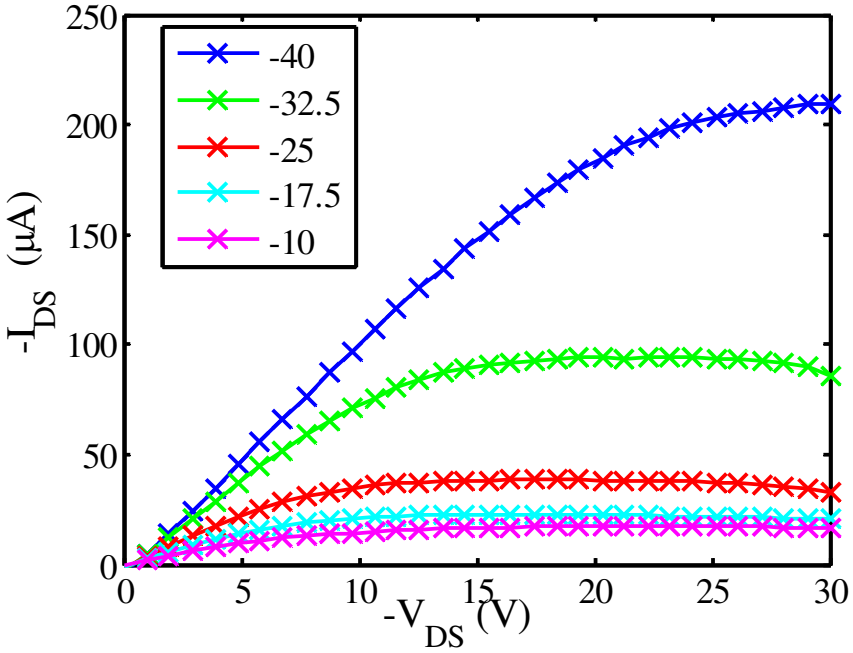

Figure 20 I_{DS}-V_{DS} characteristic of unprotected CNTFET for various back-gated voltages V_{BS}, shown in the legend in volts.

Although the transfer characteristic of CNTFET is controlled by the Schottky barrier (SB) at the source junction, the mechanism is different from that of the SB-MOSFET. It is understood that the carrier injection in SB-MOSFET is due to thermionic emission. But the thermionic picture changes drastically as the size of the transistor body is thinned down below the depletion length L_D of the semiconductor. In the case of an ultrathin body SB-MOSFET, the potential profile in the contact barrier is determined by both the L_D and the physical boundary. In the case of CNT, the actual body thickness is just ~ 1.4 nm, and consequently, the barrier is extremely thin. Thus tunneling is not only possible, but regarded as a dominant mechanism in transport rather than thermionic injection [59, 60]. One would argue that the thinness of the SB in CNTFET would blur the distinction between SB contact and ohmic contact at the source-channel interface. But the important point, however, is that the gate and drain fields in the CNT are in control of the thickness of the SB, and determine its I_{DS}. In contrast if the contacts were ohmic, I_{DS} of CNTFET will be solely determined by the property of the bulk channel.

Transfer characteristic of a CNTFET from as-grown CNTs usually shows *p*-type conduction behavior, as shown in Figure 20 and Figure 21. It has been demonstrated that *p*-type character is not an intrinsic property of the CNTs, but results from the interaction with atmospheric oxygen, inducing electron transfer, and thus causing the CNTs become doped with holes [61]. The large hysteresis in the transfer characteristic of unprotected CNTFET (Figure 21) is believed to be due to water molecule adsorption [62]. Upon passivation of CNTFET with atomic layer deposited (ALD) Al_2O_3, we find that CNTFET recovers its ambipolar characteristic and exhibits

much reduced hysteresis. Due to the growth mechanism and film quality of ALD, we think that ALD Al_2O_3 passivation of CNTFET achieves both removal of oxygen and water vapor from the CNTs.

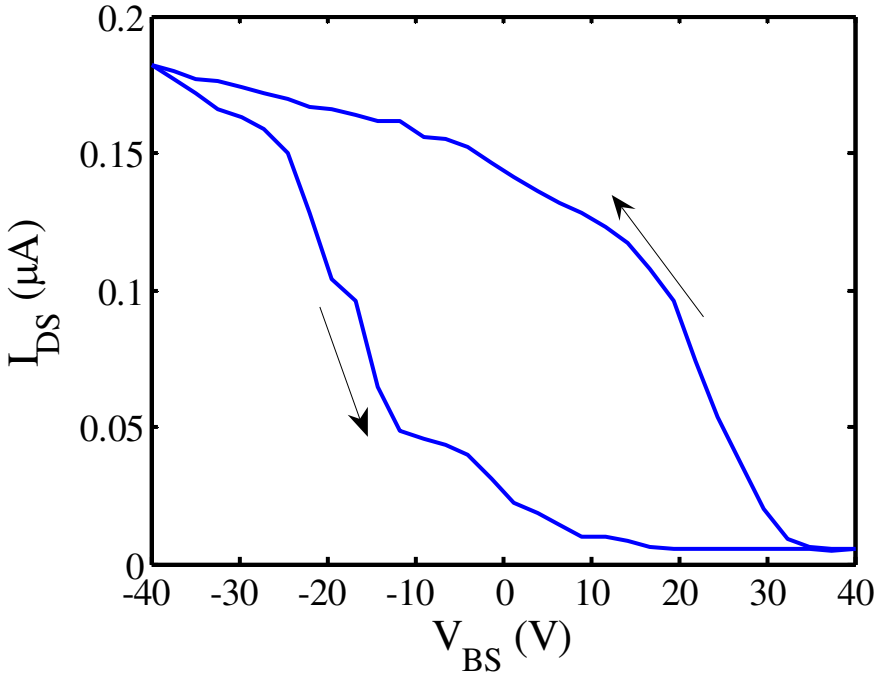

Figure 21 Back-gated transfer characteristic of unprotected CNTFET (V_{DS} = 0.1 V). It exhibits *p*-type conduction and large hysteresis.

Chapter 5: Electronic detection of DNA hybridization using carbon nanotube field effect transsistors

In this chapter, we will discuss how carbon nanotubes are made into field effect transistors (CNTFETs), and how the CNTFETs are used to electronically detect label-free and specific DNA hybridization. As noted before, the DNA carries negative charges along its phosphate backbone. Hybridization or binding of single stranded unknown target DNA to a pre-attached single stranded probe DNA through specific Watson-Crick base pairing leads to an increase in the amount of negative charges adsorbed at the gate of the transistors. The increase in charges induces a field effect that shifts the threshold voltages of the CNTFET toward more positive values as the presence of additional negative charges has to be compensated by the gate voltage. The amount of voltage shift reflects the amount of additional negative charges attached to the gate of the CNTFET upon DNA hybridization. Therefore, a signal for DNA hybridization is the shift in threshold voltages on the CNTFET array. With adequate modeling, this signal will allow quantitative determination of the amount of DNA present in an analyte solution. If different probe DNAs are pre-attached on various locations on the CNTFET arrays, then the threshold voltage shifts collected from different CNTFETs with different probe DNAs attachment may allow quantitative comparison of the amounts of different DNAs present in the analyte solution. This application is very relevant in the molecular biology known as

comparative gene expression assays. In the following, we will discuss the device fabrication, theory behind the working principle, measurement system, DNA attachment chemistry and finally present our results on electronic detection of label-free and specific DNA hybridization using CNTFET array.

5.1. Device fabrication

Having grown the carbon nanotubes on top of silicon oxide substrate, as described in section 4.3, we proceed with source and drain metal deposition. Prior to doing so, we briefly describe some precautions to be considered when working with CNT. All chemical bonds of the carbon atoms in graphitic form are filled, unlike silicon which possesses dangling bonds that need to be passivated. The positive implication is that CNT devices may have broader choice of oxide material than silicon devices, which have much limited choices in order to minimize the detrimental oxide interfacial states. This same reason is responsible for why CNTs do not stick well to a lot of materials. Since the final device needs to be connected to the measurement system through wire bonding to the package, we need to ensure that the bonding pad films adhere very well to the substrate. This means that there must be no CNTs trapped underneath the bonding pad films. The details of the fabrication steps will be discussed in the following.

5.1.1. Step 1: Bonding pad alignment marks

Figure 22 shows the mask for bonding pads. The substrate containing CNT mats is washed by standard acetone, methanol, isopropanol wash, but ultrasonic

cleaning is avoided at all costs because this procedure removes the CNTs. Pattern transfer is done using standard photolithography using a contact mask. First the BPRS-200, a novolak resin-based positive photoresist, was spun-on at 3000 rpm for 60 s. The photoresist is capable for a line resolution of around 1.5 μm. Pre-exposure bake was done in an oven at 105 °C for 10 minutes. Then the pattern in the mask was transferred by exposing the photoresist in a contact aligner for 6 s. No postbake was required. Pattern development was done by immersing the substrate in PLSI 3:1 for 90 s. The mask shown in Figure 22 is dark field clear feature, and since positive photoresist was used, there would be no photoresist on the area colored with blue and red in Figure 22 on the substrate after development.

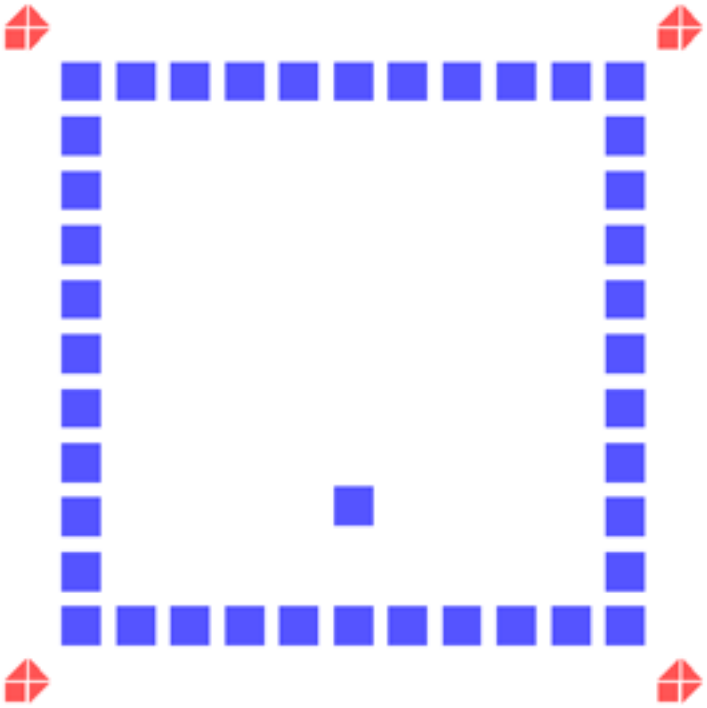

Figure 22 Mask for bonding pads.

To ensure strong adhesion, CNTs have to be removed prior to metal deposition. CNT removal is done by exposing substrate with patterned photoresist to

oxygen plasma. Then 5 nm of chromium and 45 nm of gold film were evaporated, followed by lift-off in acetone. This results in direct adhesion of the Cr/Au film on the area colored with blue and red, while CNT mats cover elsewhere. This first metal layer serves as an alignment mark for subsequent pattern transfers.

5.1.2. Step 2: Unwanted CNT removal

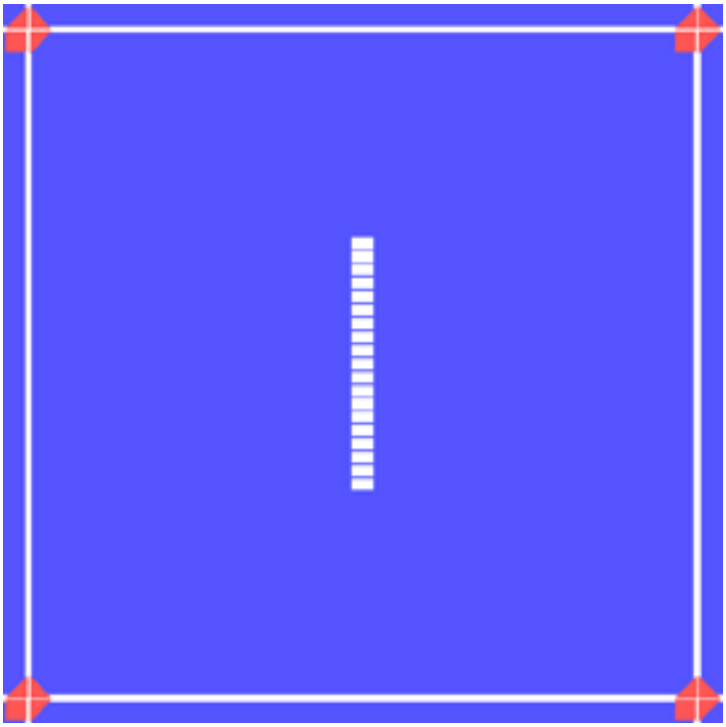

Figure 23 Mask for CNT removal.

Figure 23 shows the mask, which has a dark field clear feature used for this step. The goal is to wipe out all CNTs to ensure good metal film adhesion except only at the active area defined by the mask. Again, the same BPRS-200 coating, baking, exposure, development, described before were done and followed by oxygen plasma treatment to remove CNTs at areas unprotected by the photoresist. The end result left

us with the original Cr/Au alignment layer, and CNTs only at the white area in Figure 23.

5.1.3. Step 3: Actual metal electrodes patterning

Having wiped out unwanted CNTs, we are ready to deposit the actual metal electrodes for the drains and sources. BPRS-200 coating, baking, exposure, development, described before, were done to transfer the patterns in the mask shown in the Figure 24 to the substrate. 10 nm of chromium and 25 nm of aluminum were evaporated. At this stage, the CNTFETs are ready to be tested using back-gated transistor characteristics measurement.

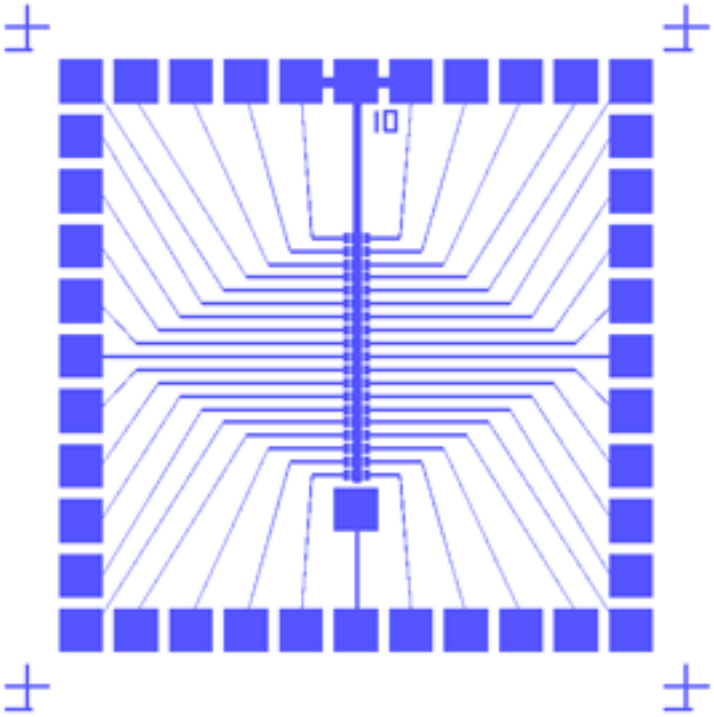

Figure 24 Mask for source drain electrodes.

5.1.4. Step 4: Al_2O_3 atomic layer deposition

We shipped out the samples to Cambridge Nanotech Inc. for deposition of 25 nm of Al_2O_3 using atomic layer deposition (ALD). The principle of ALD is based on sequential pulsing of chemical precursor vapors, both of which form about one atomic layer each pulse. This generates pinhole free coatings that are extremely uniform in thickness. For example, ALD of Al_2O_3 film requires cycles of tri-methyl aluminum (TMA) vapor pulse and water vapor pulse. During the TMA vapor pulse cycle the methyl groups of TMA is released, allowing the aluminum to bind with the oxygen from the hydroxyl groups on the surface. The methane by-product is pumped out on the subsequent cycle, along with the excess TMA. During the water vapor pulse cycle, the water vapor converts methyl groups of the bound TMA into fresh hydroxyl groups that are available for aluminum binding on the next TMA pulse cycle. In this manner, layer by layer of Al_2O_3 film is built up. Although Cambridge Nanotech claims that Al_2O_3 should stick to gold, we saw the contrary effect. This is the reason we used aluminum for the metal electrodes in Step 3. The Al_2O_3 will not stick to CNTs, instead it will just grow over the CNTs. When used for biosensors, the device needs to interface with wet buffer electrolyte. One of the most important reasons for the choice of Al_2O_3 is that Al_2O_3 is a good barrier against mobile alkali ion penetration, such as sodium. This is important to get stable enough device threshold voltages. The other reason is the high-k of Al_2O_3 film that will work in favor for us.

5.1.5. Step 5: Bonding pad oxide etch and gold film build-up

Aluminum oxide is covering the entire chip after Step 4. The aluminum oxide on top of the bonding pads has to be opened-up to gain access to the pads for wire-bonding to a mounting package. We have bad control over Al_2O_3 etch using wet chemicals, so we would like to stick with dry etch. Again, BPRS-200 coating, baking, exposure, development, described before, were done to transfer the pattern in Figure 22. We noted here that despite BPRS-200 being an old technology, its process is compatible with Al_2O_3, since the developer for BPRS-200, PLS1 3:1, does not contain tetramethylammonium hydroxide (TMAH), which dissolves aluminum, whereas the developers for most modern photoresist contain TMAH.

Having patterned the photoresist, we can etch down the aluminum oxide using reactive ion etcher (RIE). Unfortunately, the RIE system at the Laboratory for Physical Sciences (LPS) is fluorine based chemistry, and aluminum fluoride is non-volatile. Therefore, it is not the most ideal system for Al_2O_3 etching. Nevertheless, if we RIE (175 W, 40 mTorr, 18 sccm CHF_3, 2 sccm O_2) the Al2O3 film long enough, it will eventually give way due to ion bombardment. So the etching is done not by reactive gas chemistry, rather by physical ion bombardment to knock off the film. This gives rise to another problem, because in the process, the photoresist is being coated by non-volatile residues, which make the photoresist insoluble in acetone. Fortunately, BPRS-200 process is an old technology, and the industry has provided a solution for removing post-RIE polymer residue coated novolak resin based photoresist, i.e. Microstrip 5010. So we can get around the etching problem, even though the RIE system is not a suitable one. Since the etching happens because of

physical ion bombardment, the process is not selective at all. Also the etch rate is really slow, i.e. ~4 nm/min, as opposed to 50 nm/min in etching SiO_2 under fluorine based RIE. However, since we have the Cr/Au alignment layer beneath the Al_2O_3 on the bonding pads, the ion bombardment would stop at that layer. So Cr/Au alignment serves also as an etch-stop layer.

After Al_2O_3 etching, we can reserve the photoresist as the lift-off mask. Without removing the resist, we evaporated more Cr/Au (5 nm/ 150 nm) on the bonding pads. The reason for this is that the gold wire bonding may knock-off the film in the process, so it requires thick enough gold film to bond to. Having built up gold thickness on the bonding pads, we can then proceed with lift-off to remove the

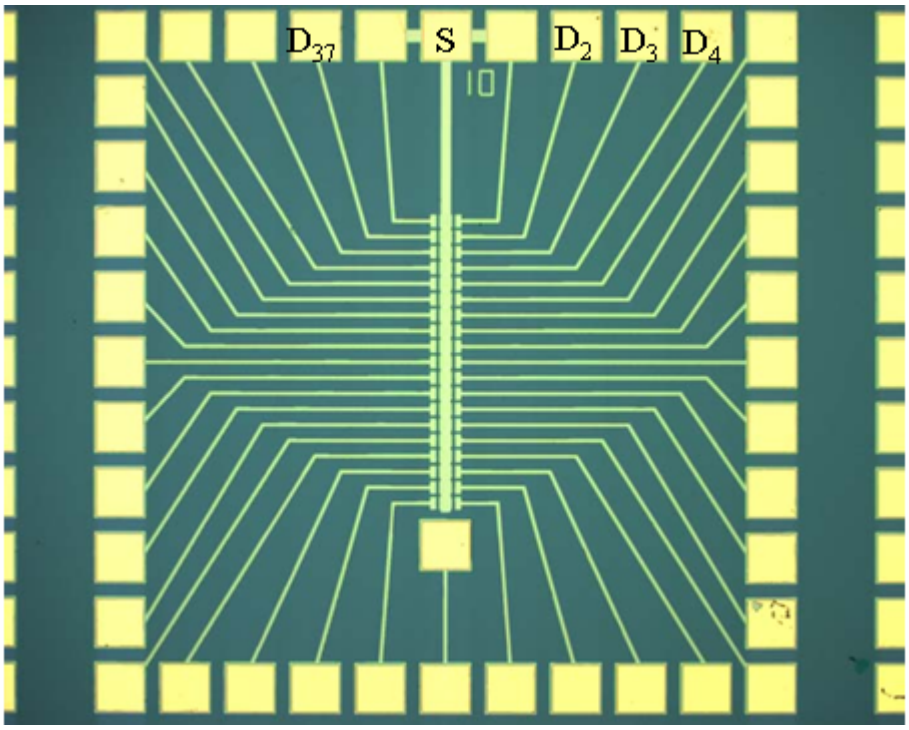

Figure 25 Layout of the CNTFET array. The center bar denoted by "S" is the common source electrode, shared by other drain electrodes, denoted by "D_2", "D_3", etc. Each source and drain pair comprise one transistor

photoresist, as well as the unwanted gold film, in Microstrip 5010. Figure 25 shows the end result of the fabricated chip.

5.2. Theory

Since the signal we are looking for is the voltage shift of the transistor, it is very important to understand the voltage drops that occur at interfaces. The gate source voltage, V_{GS}, will drop across the gate oxide, and two electrode-electrolyte interfaces, namely, the oxide-buffer interface and Ag/AgCl-buffer interface.

5.2.1. Electrode-electrolyte interface

In general, there are two processes that can happen at an electrode-electrolyte interface: Faradaic charge-transfer process, and non-Faradaic space charge build-up.

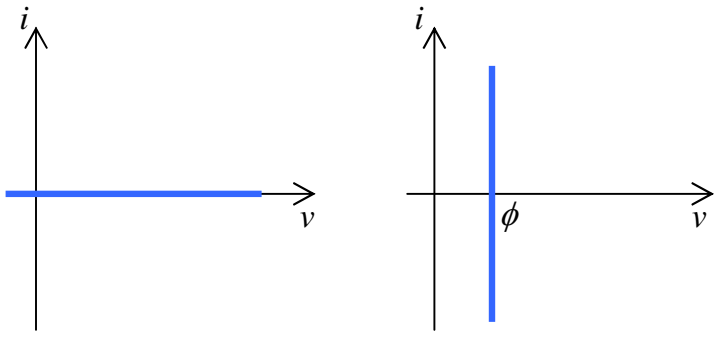

(a) (b)

Figure 26 (a) *I-V* characteristics of an ideal polarizable electrode, (b) *I-V* characteristics of an ideal non-polarizable electrode, the voltage ϕ is well-defined, and given by the Nernst equation.

Apart from the complication of electrochemical processes, an electrode in an idealized model can be classified as either a polarizable electrode, or a non-polarizable electrode, although an electrode in the real-world is never completely polarizable, nor non-polarizable.

An ideal polarizable electrode exhibits *I-V* characteristics shown in Figure 26(a). The interface can support any voltage drop without allowing current to pass through the interface, so it behaves very much like a capacitor. The process that happens at the interface is solely non-Faradaic space charge build-up.

An ideal non-polarizable electrode exhibits I-V characteristics shown in Figure 26(b). The interface will allow any current to pass through by chemical reduction and oxidation reactions happening at the interface. It behaves very much like a forward-biased diode. The voltage drop is very well-defined and given by the Nernst equation. The process that happens at the interface is only Faradaic charge transfer process.

Since no real-world electrodes behave solely as ideal polarizable or ideal non-polarizable, the Randles equivalent circuit (Figure 8 in chapter 3) is generally invoked to describe the electrochemical processes that happen at an interface. It basically consists of parallel connections of a capacitor to model the non-Faradaic process, and an impedance to model the Faradaic process. The Faradaic impedance takes into account both the charge transfer and the mass transfer mechanism that might limit the reaction rate. The equivalent circuit also includes the solution resistance in the model.

5.2.1.1. Nernstian equation for ideal non-polarizable electrodes

Consider the interface of an electrode and an electrolyte, which has a common species with the electrode, such as Ag/AgCl electrode and chloride containing solution. Both oxidation and reduction reactions can occur reversibly to establish an equilibrium chloride concentration.

Oxidation: $AgCl\ (s) + e^- \rightarrow Ag + Cl^-\ (aq)$

Reduction: $Ag + Cl^-\ (aq) \rightarrow AgCl\ (s) + e^-$

The chemical reaction happening at the interface provides a mechanism for charge transfer, since current is carried by ions in the solution, and by electrons in the electrode, the ions and electrons exchange at the interface through the chemical reduction and oxidation reactions. Once the equilibrium concentration is reached, the system is said to have reached thermal equilibrium, meaning that the rate of oxidation is the same as the rate of reduction. Therefore there is no net current flowing through the interface. Setting $j = 0$ in the Nernst-Planck drift diffusion equation we get,

$$j_i(x) = -\mu_i\left(k_B T\frac{dC_i}{dx} + ez_i C_i\frac{d\phi}{dx}\right) = 0, \tag{44}$$

where i indicate the species or ion being considered, z_i denotes the valence of that ion, e.g $z_{Na^+} = 1$, and $z_{Cl^-} = -1$, and C_i, is the concentration of that ion. One can recognize immediately the first term is the diffusion term, and the second term is the drift term. Integrating with respect to x, we get

$$\ln C_{Cl^-}(x_B) + \frac{e}{k_B T}\phi(x_B) = \ln C_{Cl^-}(x_S) + \frac{e}{k_B T}\phi(x_S) \tag{45}$$

$$\Delta\phi = \frac{k_B T}{e}\ln\left(\frac{C_{Cl^-}}{C_{eq}}\right) \tag{46}$$

which is known as the Nernst equation. The meanings of x_S and x_B are clarified in Figure 27. Since C_{eq} is a constant as long as the temperature is fixed, the voltage drop

across the electrode and electrolyte is a function of the chloride concentration used in the buffer electrolyte.

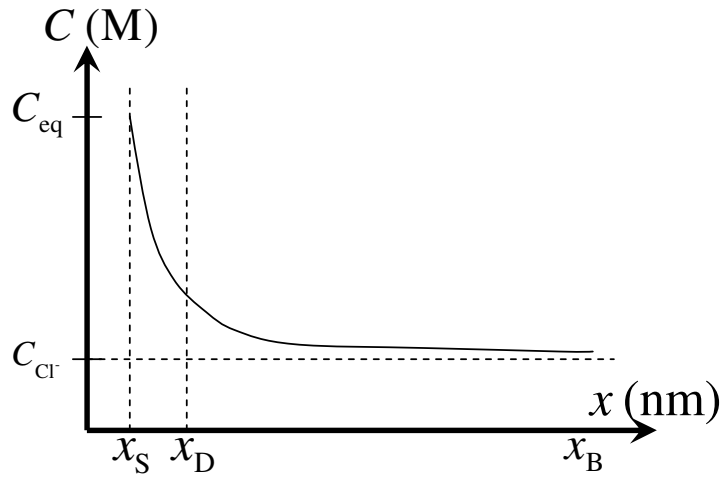

Figure 27 Illustration of the concentration profile at an electrode-electrolyte interface. The interface is at $x = 0$. x_S indicates the Stern layer or inner Helmholtz layer, within which only specific adsorbed ions can reach. x_D indicates the Debye length, within which most of the concentration change happens. x_B indicates a distance from the electrode where the concentration reaches the bulk concentration of the ions.

We saw that by starting with the drift-diffusion equation to arrive at the Nernst equation gives exactly the same the equation as is used to derive carrier concentration in semiconductor devices. Similarly the Nernst equation is also only accurate in the limit of low electrolyte concentration, the so called the ideal gas limit. Different fields may have different keywords, such as low injection in *p-n* junction. But they essentially mean the same thing, that is the interaction among ions or

carriers has been ignored. Anyhow this simple model can give us intuition on what is going on in our experiment.

An electrode, with a well-defined voltage drop, is desired as a reference electrode in an electrochemical cell, in which precise potentiometric measurement is required. Some examples of well-behaved reference electrodes are standard hydrogen electrode, which consists of a platinum wire and a constant flow of hydrogen gas; saturated calomel electrode, which consists of mercury; and Ag/AgCl, which is the easiest and widely used reference electrode.

5.2.1.2. Guoy-Chapman-Stern double layer model for ideal polarizable electrodes

Unlike an ideal non-polarizable electrode, which allows reversible oxidation

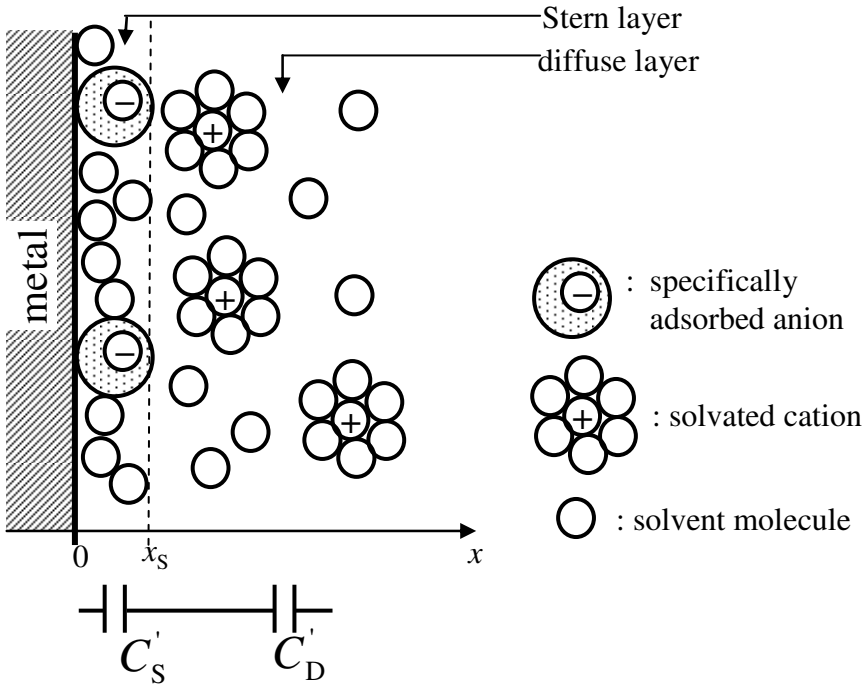

Figure 28 The model of the electrical double layer.

and reduction charge transfers to establish thermal equilibrium, and in effect, a well-defined voltage drop, governed by Nernst equation, develops across the interface, an ideal polarizable electrode does not allow any current or charge transfer to pass through the interface, instead space charges will build up at the interface, and it behaves like a capacitor.

The model for electrode-solution interface can thought to be made up of two layers. The closest layer to the electrode, the *inner* layer, contains solvent molecules or species that are said to be specifically adsorbed. This layer is also called the *compact*, *inner Helmholtz*, or *Stern* layer (Figure 28). Solvated ions can approach the electrode only to the outside layer, called the *outer Helmholtz* layer or *diffuse* layer. The whole array is called the *electrical double layer*. The charge profile is given by the Guoy-Chapman-Stern model. Putting $j = 0$ in the above Nernst-Planck drift-diffusion equation, (44), since no current is allowed to pass through the ideal polarized electrode interface, we can solve for C_i, which is no different from a Boltzmann factor:

$$C_i = C_i(\infty)\exp\left(-\frac{ez_i\phi(x)}{k_{\mathrm{B}}T}\right) \tag{47}$$

Solving the above equation simultaneously with the Poisson equation, we obtain:

$$\begin{aligned}\rho &= \sum_i z_i eC_i = \sum_i z_i eC_i(\infty)\exp\left(-\frac{ez_i\phi(x)}{k_{\mathrm{B}}T}\right)\\ \frac{d^2\phi}{dx^2} &= -\frac{\rho}{\varepsilon} = -\frac{e}{\varepsilon}\sum_{i=Na^+,Cl^-} z_i C\exp\left(-\frac{ez_i\phi(x)}{k_{\mathrm{B}}T}\right)\end{aligned} \tag{48}$$

We have assigned $C_{Na^+}(\infty) = C_{Cl^-}(\infty) = C$.

The end result is known as the Grahamme equation:

$$\sigma^M = -\sigma^S = -\varepsilon\left(\frac{d\phi}{dx}\right)_{x=x_S} = \sqrt{8k_B T\varepsilon C}\sinh\left(\frac{e\phi_0}{2k_B T}\right) \tag{49}$$

If the potential is small comparable to the $k_B T$, the potential profile can be linearized, and expressed as:

$$\phi = \phi_0 \exp\left(-\frac{x}{L_D}\right), \tag{50}$$

where $L_D = \sqrt{\frac{\varepsilon k_B T}{2e^2 C}}$ is known as Debye length, which is inversely proportional to the square root of the buffer concentration. Also $\sinh(x) \approx x$ in (49):

$$\phi_0 \approx \sigma\sqrt{\frac{k_B T}{2e^2\varepsilon C}} = \sigma\frac{L_D}{\varepsilon} \tag{51}$$

The small signal capacitance can be expressed as:

$$C_D^{'} = \frac{d\sigma^M}{d\phi_0} = \sqrt{\frac{2e^2\varepsilon C}{k_B T}}\cosh\left(\frac{e\phi_0}{2k_B T}\right) = \frac{\varepsilon}{L_D}\cosh\left(\frac{e\phi_0}{2k_B T}\right) \tag{52}$$

As noted before, that the solvated ions can not get inside the *inner Helmholtz* or *Stern* layer, the total capacitance is then a series of C'_D and a Stern capacitance, C'_S, which is independent of potential

$$C_S^{'} = \frac{\varepsilon}{x_S}, \tag{53}$$

$$\frac{1}{C_d^{'}} = \frac{1}{C_S^{'}} + \frac{1}{C_D^{'}} \tag{54}$$

5.2.2. Voltage shift upon hybridization

I do not intend to analyze the voltage shift signal in a rigorous manner, because this would require complete understanding of the switching mechanism of

carbon nanotube field effect transistors, while this mechanism is still an ongoing research topic. Nevertheless the following simplified analysis should be able to provide an intuition into what we expect to see in our experiment. As described before, the signal we are looking for is the voltage threshold shift after target DNA binding, since the amount of negative charges attached to the gate of the transistor will increase upon binding or hybridization.

Figure 29 shows a simplified scenario before and after addition of a layer of charges. If we assume that the transfer characteristics I_{DS}-V_{GS} curve, simply shift upon charge addition, then for the same I_{DS}, or the same number of carriers induced in the transistor channel, an extra ΔV_{GS} voltage needs to be applied to counter the additional charges. The voltage drop across the Ag/AgCl-buffer interface is well-defined, and depends only on the concentration of the chloride ions in the solution. The Ag/AgCl reference electrode behaves more like an ideal non-polarizable electrode. Since the gate current is very small, the voltage drop on the solution resistance is also negligible. Therefore ΔV_{GS} is the change of voltage drop across oxide-buffer interface, which behaves more like an ideal polarizable electrode. The relationship between the voltage drop and the amount of surface charge is given by (49), and an extra term arising from the Stern layer:

$$\Delta V_{GS} = \frac{2k_B T}{e}\left[\sinh^{-1}\left(\frac{-\varepsilon\left(d\phi/dx\right)_{after}}{\sqrt{8k_B T\varepsilon C}}\right) - \sinh^{-1}\left(\frac{-\varepsilon\left(d\phi/dx\right)_{before}}{\sqrt{8k_B T\varepsilon C}}\right)\right] - \left(\left.\frac{d\phi}{dx}\right|_{after} - \left.\frac{d\phi}{dx}\right|_{before}\right)x_S \quad (55)$$

At the oxide-buffer interface, the electric field is discontinuous by the amount of adsorbed charges:

$$\varepsilon_{ox}\left(-E_{ox}\right)+\varepsilon\left(d\phi/dx\right)=\sigma\,, \tag{56}$$

therefore the above ΔV_{GS} equation becomes:

$$\Delta V_{\mathrm{GS}}=\frac{2k_{\mathrm{B}}T}{e}\left[\sinh^{-1}\left(\frac{-\left(\sigma+\varepsilon_{ox}E_{ox}\right)_{\mathrm{after}}}{\sqrt{8k_{\mathrm{B}}T\varepsilon C}}\right)-\sinh^{-1}\left(\frac{-\left(\sigma+\varepsilon_{ox}E_{ox}\right)_{\mathrm{before}}}{\sqrt{8k_{\mathrm{B}}T\varepsilon C}}\right)\right]$$
$$-\left(\left(\sigma+\varepsilon_{ox}E_{ox}\right)_{\mathrm{after}}-\left(\sigma+\varepsilon_{ox}E_{ox}\right)_{\mathrm{before}}\right)\frac{x_{\mathrm{S}}}{\varepsilon} \tag{57}$$

For small voltage, and assuming E_{ox} does not change upon charge (σ) insertion, since the charges induced in the channel remain the same before and after charge insertion, the expression can be simplified as

$$\Delta V_{\mathrm{GS}}\approx-\Delta\sigma\frac{L_{\mathrm{D}}+x_{\mathrm{S}}}{\varepsilon}=-\frac{\Delta\sigma}{C_{\mathrm{d}}^{'}}=-\Delta\sigma\left(\frac{1}{C_{\mathrm{S}}^{'}}+\frac{1}{C_{\mathrm{D}}^{'}}\right), \tag{58}$$

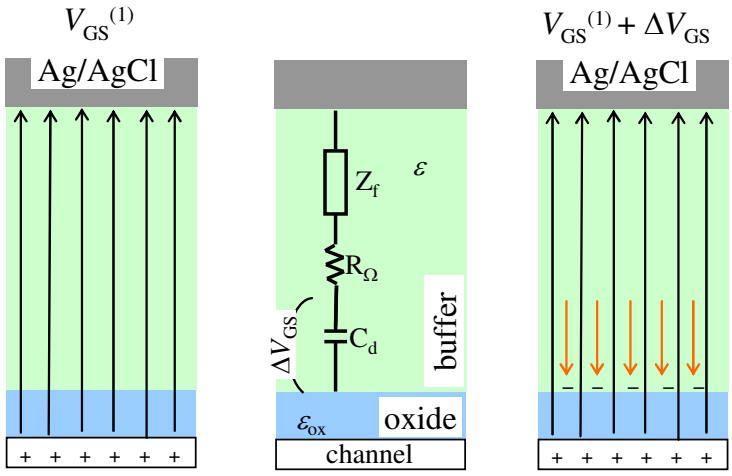

Figure 29 Illustration of how extra charges induce a voltage shift in the transistor: (a) field lines before charge addition. (b) the equivalent circuit, Z_f is the Faradaic impedance, R_Ω is the solution resistance, C_d is the double layer capacitance. ΔV_{GS} comes mainly from the voltage drop change across the double layer capacitance. (c) field lines after charge addition.

exactly as depicted in Figure 29, that the extra voltage ΔV_{GS} drops mainly across the double-layer capacitance.

Another device design consideration that can be gleaned from (57) is that we want to maximize the oxide capacitance and to minimize the double-layer capacitance in order to maximize the voltage shift, such that the term inside the $\sinh^{-1}$ bracket is maximized. Maximizing oxide capacitance is, in effect, increasing the $\varepsilon_{ox}E_{ox}$ term, while minimizing double-layer capacitance is, in effect, reducing the buffer concentration, C.

5.3. Measurements

Since the hybridization signal we were looking for is the threshold voltage shift of the transistor upon hybridization, we made top-gated I_D-V_{GS} transfer characteristics measurement before and after hybridization. Figure 30 shows the schematics for back-gated and top-gated transfer characteristics measurement. It was not possible to carry out real-time monitoring of the threshold voltage shift as the hybridization reaction was going on, because of the contradictory requirements for hybridization and detection.

As described before, the Debye length is a function of ionic concentration in the buffer solution. This Debye length is a screening length, within which the electric field from a charged body immersed in an ionic electrolyte can still be felt. The hybridization or binding of single-stranded target DNA with the single-stranded probe DNA pre-attached on the surface is essentially a competition between the hydrogen

bonds between the Watson-Crick complementarily matched bases that favor binding, and the electrostatic repulsion of like-charge from the phosphate backbone of the two DNA strands.

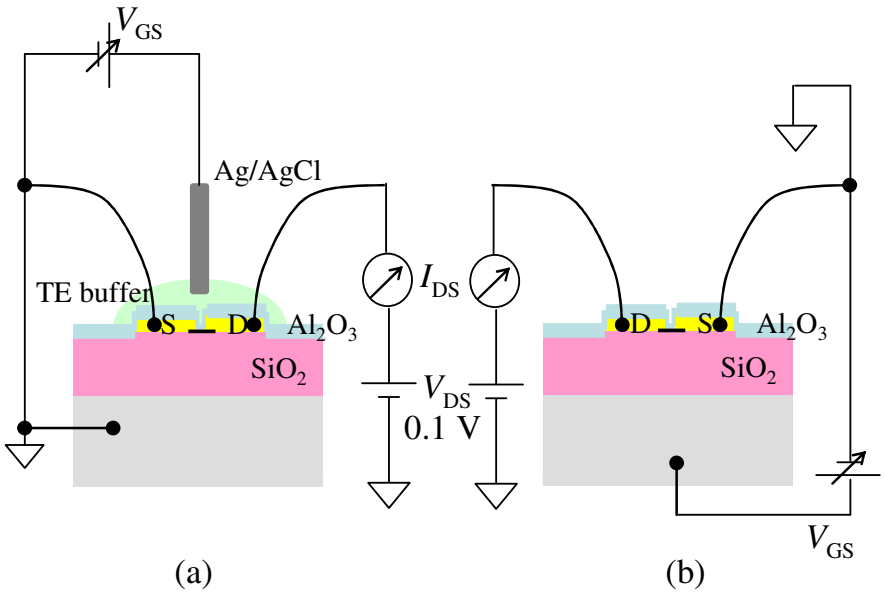

Figure 30 Schematics of the electrical measurement for (a) top-gated, (b) back-gated I_{DS}-V_{GS} transfer characteristics.

During hybridization, high salt or high ionic buffer is required to shorten the Debye length such that the electrostatic repulsion is screened, allowing the complementary bases to meet each other and to form hydrogen bonds. However, at the same time, the high salt solution also screens out the voltage shift signal we would like to detect. It is described in the previous section that for very simplified model, the voltage shift can be thought of due to an increase in the amount of charge at the double-layer capacitor, therefore the voltage shift is maximized when the double-

layer capacitance is minimized, which means that the Debye length should be as long as possible.

The other precaution to note is the sodium poisoning to the oxide layer. Al_2O_3 is a very good choice for the oxide layer, not too much because of its high permittivity, but more because it is a good barrier against mobile alkali ions. If alkali ions got into the oxide layer, they would move around with the applied gate voltage, creating unstable threshold voltage for the transistors.

Although the limitation of real-time monitoring may seem like a drawback, we pointed out that real-time monitoring is not required for gene identification and expression assays. We used 10 mM PBS (phosphate buffer saline) pH 7.0, 0.3M NaCl for hybridization and TE (Tris-EDTA) 1x pH 7.4 with no salt for electrolyte measurement. The hybridization took place no more than two hours at room temperature to prevent sodium poisoning to the oxide layer.

5.4. DNA attachment chemistry

Probe DNA was attached to the surface through silane coupling molecules. First the oxide surface has to be hydroxylated. There are several ways to do that. We used an oxygen plasma (100 W, 200 mTorr, 16 sccm O_2) treatment to generate hydroxyl terminated surface. Next, the surface is functionalized with MPTMS (3-mercaptopropyl-trymethoxysilane), by exposing the surface to MPTMS vapor. The chip was mounted to the lid of an enclosed jar, with the MPTMS solution sitting at the bottom of the jar. A temperature gradient was created by heating the bottom part

of the jar to 60 °C for about 10 minutes to induce flow of MPTMS vapor to the chip. The MPTMS vapor should condense and generate ideally a self-assembled monolayer on the chip. Then, the lid is heated and the bottom of the jar is cooled, to drive off excess vapor from the chip by temperature gradient. This last step took about 30 minutes, and we get an MPTMS-functionalized surface on the chip.

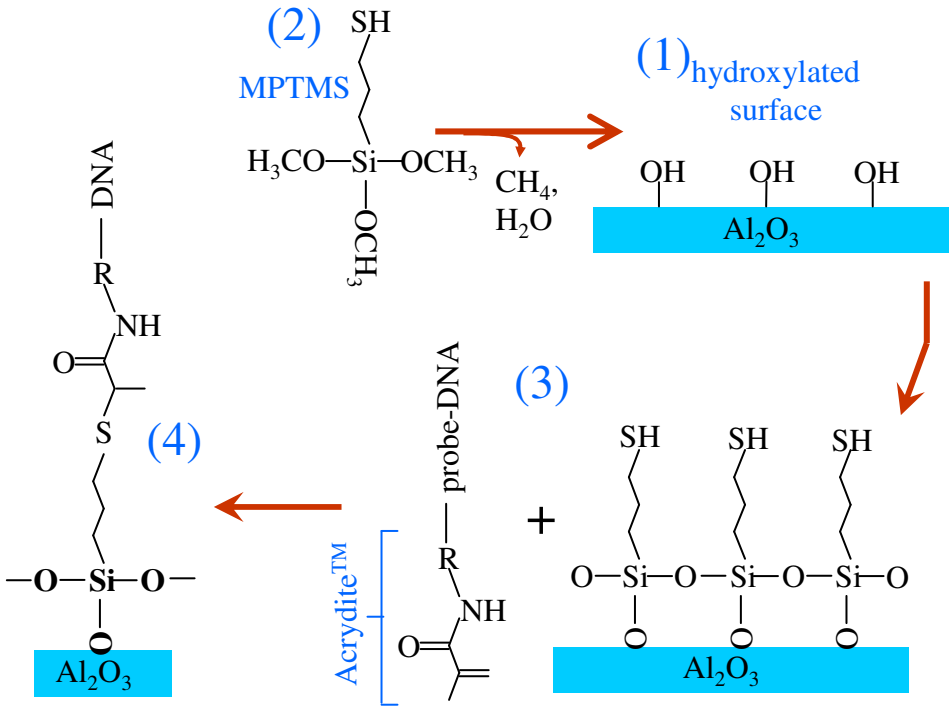

Figure 31 Steps for Acrydyte™ modified probe-DNA immobilization: (1) surface hydroxylation, (2) MPTMS exposure, (3) probe-DNA spotting.

The probe DNA is modified with Acrydite™ at the 5' terminus. This Acrydite™ molecule binds readily to the sulphur group of the MPTMS-functionalized surface. 10 μM of Acrydite™ modified probe DNA diluted in TE 1x pH 7.4 was pipetted to the MPTMS-functionalized surface. For complete binding of Acrydite™ to MPTMS, it was recommended to allow slow drying of the pipetted spot. To

achieve that, the chip was enclosed in a humidified container and allowed to dry overnight. It is crucial to ensure that the spot was dried eventually. This is also the reason we would like to dilute the probe DNA in non-sodium containing buffer. TE is an organic buffer that does not contain sodium.

After this stage, we mounted the chip and wire-bonded the source and drain electrodes to a package. I_{DS}-V_{GS} transfer characteristics were measured, and served as a reference for comparison with the transfer characteristics after target DNA hybridization.

Target DNA was diluted to the desired concentration with 10 mM PBS pH 7.0, 0.3 M NaCl. Hybridization took place by incubating the target DNA to the chip for 2 hours, followed by washing with TE 1x pH 8.0. I_{DS}-V_{GS} transfer characteristics were measured again, and a shift in threshold voltage was obtained. Table 3 shows the sequences of DNA used in this experiment.

Name	Sequence
Probe	5'-/Acrydite//CAG ATG CCA CAT AAG GGG TTT GCC ATT TGA TAC CCC TGG GGA ACA TTT CTG TAA ATA CCA T -3'
complementary target	5'-/ATG GTA TTT ACA GAA ATG TTC CCC AGG GGT ATC AAA TGG CAA ACC CCT TAT GTG GCA TCT G -3'
Non-complementary target	5'-/TTT TTT TTT TTT TTT TTT AGT CCG TGG TAG GGC AGG TTG GGG TGA CT-3'

Table 3 DNA oligonucleotide names and sequences. All oligonucleotides were ordered from Integrated DNA Technology, Inc.

Resuspending dry oligos:
1. Spin down briefly the vial to have the dried oligo at the bottom of the vial 2. Open the lid without tilting the vial and add the required amount of TE 1x pH 7.4 to a stock concentration of 0.1 mM, e.g. Look up "Amount of oligo" in the spec sheet for the number of nmoles, say x nmoles, then add add 10·x μL of TE 1x pH 7.4 to the corresponding vial 3. Vortex to ensure that the dried oligo is completely dissolved 4. Store in refrigerator (best in freezer, however frequent freeze-thaw cycle should be avoided) after usage.
Buffer preparation:
• TE (Tris-EDTA) 1x pH 7.4 can be purchased as is from Sigma. It contains 10 mM of trishydroxymethylaminomethane or more commonly referred as Tris, and 1 mM of ethylenediamine tetraacetic acid or EDTA.
• 0.2M PBS (phosphate buffer saline) pH 7.0: a) Prepare solution A: Add 40 mL water to 1.104 gram sodium dihydrogen phosphate monohydrate ($NaH_2PO_4 \cdot H_2O$) in the 50 mL centrifuge tube b) Prepare solution B: Add 40 mL water to 2.146 gram sodium phosphate dibasic heptahydrate ($Na_2HPO_4 \cdot 7H_2O$) in the 50 mL centrifuge tube c) Mix 15.6 mL of solution A and 24.4 mL of solution B to make 40 mL of 0.2 M sodium phosphate buffer
• 10 mM PBS (phosphate buffer saline) pH 7.0: Add 2 mL of 0.2 M sodium phosphate buffer to 38 mL of water to make 40 mL of 10 mM PBS
• 10 mM PBS, 0.3 M NaCl pH 7.0: Add 2 mL of 0.2 M sodium phosphate buffer and 2.4 mL of 5M NaCl to 35.6 mL of water to make 40 mL of 10 mM PBS, 0.3M NaCl

Probe DNA dilution:
Dilute probe DNA (Acrydite™ modified) to 10 μM from the stock concentration using TE 1x pH 7.4
Target DNA dilution:
Dilute target DNA to 1 mM, 100 nM, 10 nM, etc. from the stock concentration using 10 mM PBS, 0.3 M NaCl, pH 7.0
Probe DNA attachment:
1. Hydroxylate the oxide surface using oxygen plasma 2. Functionalize the hydroxylated surface with MPTMS using vapor deposition 3. Incubate Acrydite™ modified probe DNA to the surface, and ensure slow drying. The Acrydite™ modified probe DNA has to dry before passivation.
Passivation:
Incubate 50 mM of L-Histidine pH 7.0 for ~10 minutes then wash away with distilled water. No drying should occur.
Target DNA hybridization:
Incubate the desired target DNA concentration for ~ 2 hr, then wash away with TE.
Buffer used during electronic measurement:
TE 1x pH 7.4

Table 4 Summary of all of the chemical protocols encountered in the experiment.

5.5. Results

The major progress in this project is the use of Al_2O_3 ALD to passivate CNTs. Comparing Figure 19 and Figure 21, Al_2O_3 ALD passivation results in dramatic improvements of the electrical properties of CNTFETs. After passivation, the transfer characteristics of the CNTFETs exhibit very small hysteresis when back-gated, and even negligible hysteresis when top-gated through wet buffer electrolyte. This is very important since the sought after signal is the voltage shift. Moreover, ambipolar

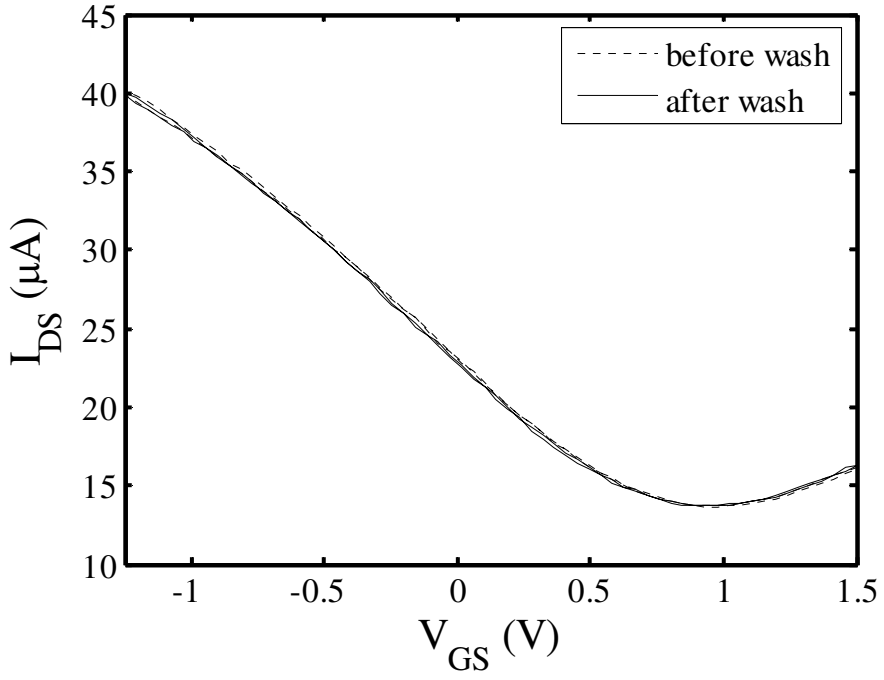

Figure 32 Top-gated transfer characteristic through Ag/AgCl reference electrode and electrolyte buffer. The plot shows very good repeatability of device behavior upon washing, blow-drying and buffer change. There are indeed 2 sweeps (forward and reverse) for both solid and dashed lines, but they are indistinguishable, therefore the hysteresis is negligible.

behavior is recovered after passivation, versus *p*-type conduction behavior before passivation. Also Al_2O_3 is a good barrier against alkali ion penetration.

Figure 32 shows a top-gated I_{DS}-V_{GS} transfer characteristic. The voltage was applied to the Ag/AgCl reference electrode, and the nanotube channel was gated through the 25 nm thick aluminum oxide. The plot shows a much reduced range of voltage needed to gate the channel. It also shows high repeatability upon device washing and change of buffer solution. The ambipolar characteristic is helpful in defining the threshold voltage. We define the threshold voltage as the voltage at which I_{DS} is minimum. The threshold voltage position was obtained by fitting a parabola around the minimum to the transfer characteristic curve

In order to verify that the threshold shift is indeed due to the target binding, we used fluorescently labeled target DNA to allow simultaneous electrical detection and fluorescent detection of the DNA hybridization. Figure 33 shows the transistor transfer characteristics for the cases of probe-DNA, target DNA hybridization, and denaturation/dehybridization wash to remove target DNA. The transistors showed a rightward or positive threshold voltage shift upon exposure of 1 μM of target DNA hybridization, as expected since more negative charges were adsorbed on the surface. To remove the target DNA, the transistors were washed with copious amounts of warm distilled water. After this procedure, which we refer as *dehybridization wash*, the threshold voltage reverted back to the values before hybridization. The success of hybridization and dehybridization are confirmed by the fluorescence image in Figure 34, which denotes the existence or removal of the target DNA.

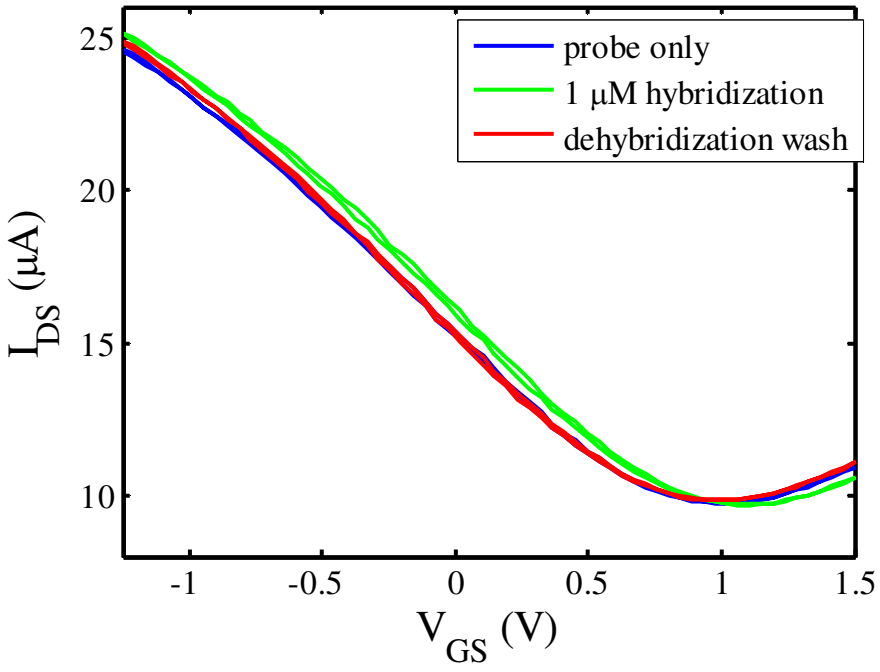

Figure 33 Transfer characteristic of CNTFET for probe-DNA only, 1 μM complementary target DNA hybridization, and subsequent dehybridization wash to remove the target DNA. The plot shows clear rightward (positive) shift in threshold voltage upon hybridization due to added negative surface charges from the target DNA, and a subsequent leftward shift after target DNA removal.

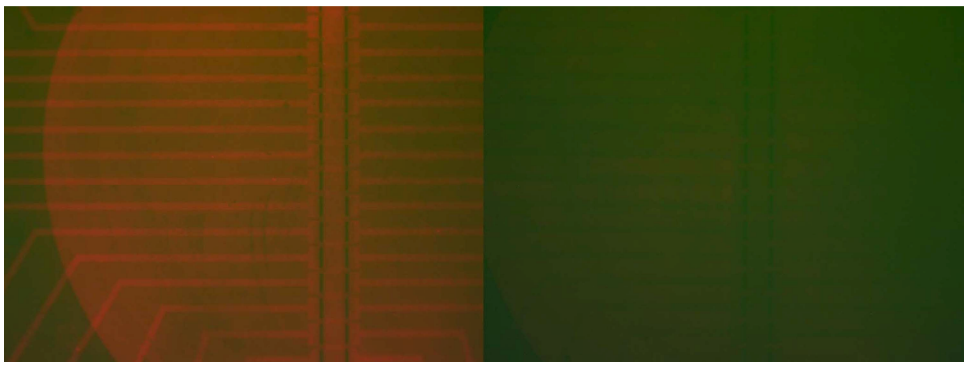

Figure 34 Fluorescent image taken after transfer characteristic measurement in Figure 33(*left*) fluorescent image of 1 μM complementary target hybridization, (*right*) fluorescent image after dehybridization wash to remove target DNA.

To further gain confidence in conclusions, we tested all of the transistors that were available in one array shown in Figure 25. Figure 35 summarizes the threshold voltage data of the transistor array upon DNA treatment. Since carbon nanotube mats were used to fabricate the device we cannot expect uniformity of threshold voltages

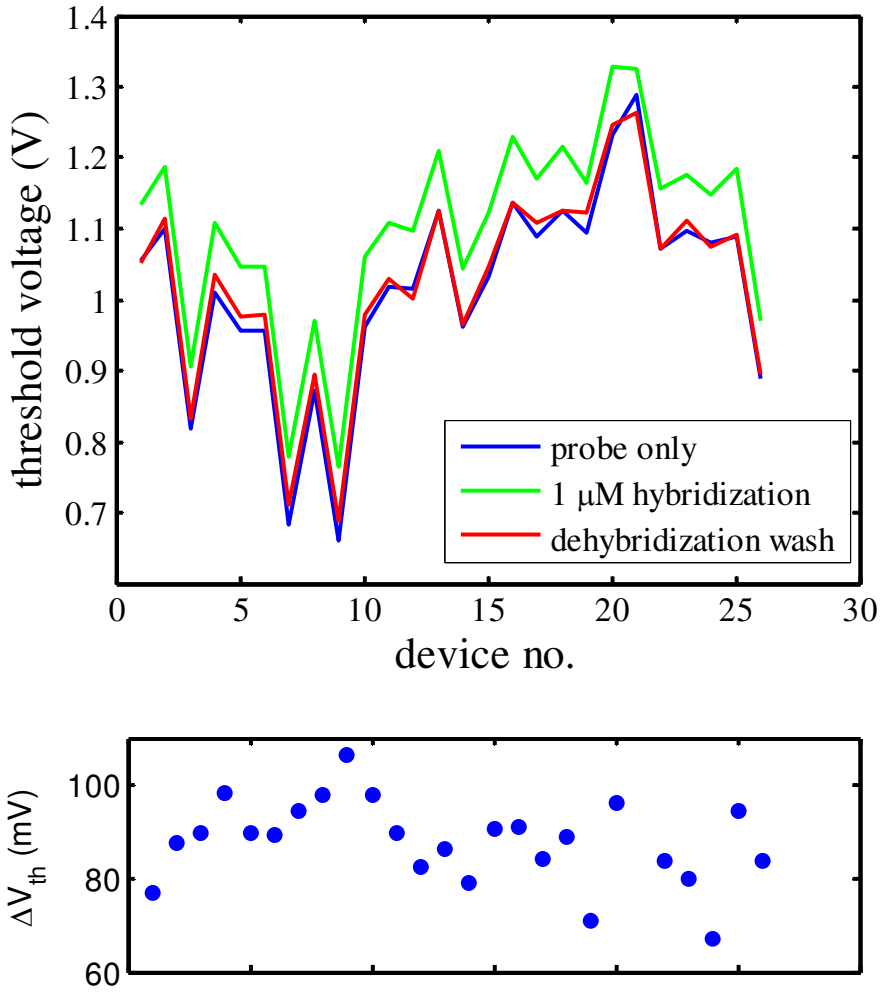

Figure 35 Threshold voltages of the transistors in the array upon DNA hybridization treatments. The plot shows universal positive shift in threshold voltage of all transistors upon complementary target hybridization, and recovery after target DNA removal through dehybridization wash. The bottom plot shows the spread of the voltage threshold shifts from the blue to the green curves.

across the array. The differences in the initial threshold voltage can be attributed to the uncontrolled variation in each of the transistor channel, such as number of nanotubes crossing the source and drain gap, chirality, and diameter of the nanotubes. However the plot shows a universal threshold voltage shift of all transistors to the positive (rightward) direction upon DNA hybridization, and universal recovery upon target DNA denaturation. The amount of shift is a function of the amount of added surface charges from the target DNA hybridization, and should not depend on the initial position of the transistor's threshold voltage. The data clearly shows this behavior. More importantly, using a simple model we can estimate how much DNA has bound to the surface. Using 10 mM for the concentration of the TE buffer being used during measurement, (58) gives an areal capacitance of 2.29×10^{-5} F/cm^2. A 60 mV voltage shift for the 1 μM target concentration as shown in Figure 36 corresponds to an additional surface charge of 1.37×10^{-6} C/cm^2, which means that the average surface density of the 61-mer target DNA is 1.4×10^{11} molecules/cm^2. Equivalently, the average spacing between target DNA is 27 nm. This number of course depends upon many factors including the probe loading and the efficiency of hybridization, and thus, we could expect improvement in sensitivity if the loading and hybridization conditions are optimized.

To address the issue of sensitivity and selectivity of our device, we measured the response at different target concentrations. Figure 36 shows the amount of threshold voltage shift at 10 nM, 100 nM and 1 μM target DNA concentrations. For this experiment, we used targets that are non labeled. We also examined the specificity of the assay by hybridizing 1 μM solution, a fairly high concentration, of

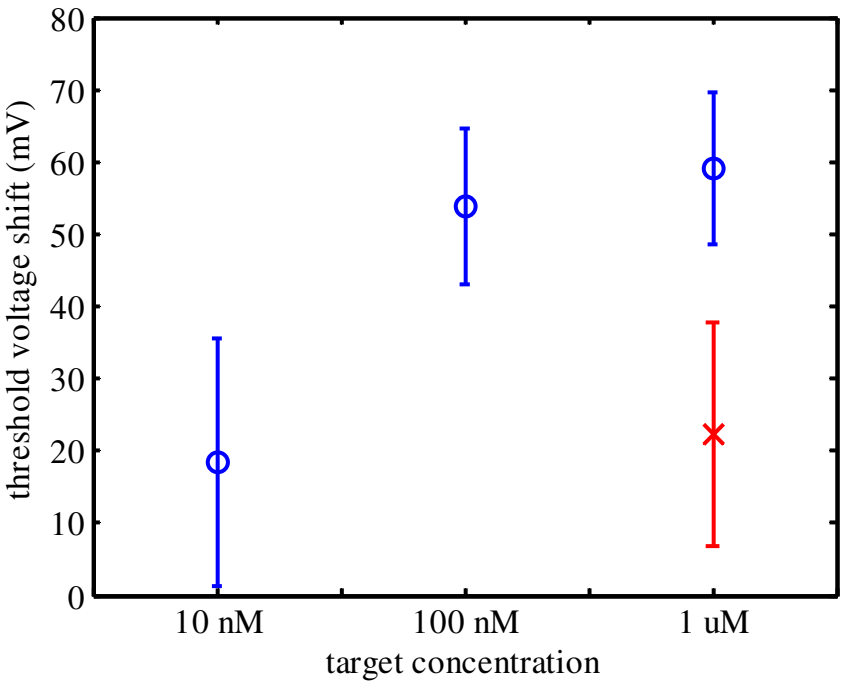

Figure 36 Titration curve shows sensitivity and specificity of the sensor. The sensitivity level is somewhere between 10 to 100 nM. The signal difference between 1 μM hybridization of complementary (blue) and that of non-complementary target (red) clearly shows the specificity of the sensor.

non-complementary target DNA. The non-complementary signal serves as the noise floor and therefore we conclude that the sensitivity of our assay is somewhere between 10 nM to 100 nM. This sensitivity is many orders of magnitude lower than the state of the art fluorescent techniques which can detect single atoms. However, to be useful for diagnostic applications the sensitivity of 1 pM or better is needed. Our system is far from being optimized but there are compelling estimates that suggest the feasilibity of achieving this level of detection through improved probe immobilization

chemistry, better hybridization protocols and improved performance by using single CNT transistors.

To conclude, the DNA-DNA detection demonstrated in this work can be extended to the detection of other biomolecules using artificial nucleic acids known as aptamers as probe molecules. These short (10 - 50 nucleotides) DNA-like sequences have been shown to bind to nucleosides, proteins, drugs and cells [63] so that our system can be generalized to detect these as well. The protocols and detection principles are the same, which imparts versatility to our CNT transistor sensing array. We provide an example of how an aptamer detects protein in the next chapter.

5.6. Analyses and discussions

5.6.1. Effective field effect mobility

The mobility of carbon nanotubes has been investigated extensively by Dürkop et al. [58]. In general, it is difficult to delineate the effects due to the contacts and those due to the channel itself. Dürkop et al. used long channel devices in order to eliminate or reduce the contribution by contacts (i.e. Schottky barriers at the source-channel contact and/or drain-channel contact) to the measured conductance. In this work, the contacts dominate the transport property, and thus we expect significantly less mobility than in the long channel measurements. We estimate the typical effective field effect mobility (μ_{FE}) from a transfer characteristic:

$$\mu_{\mathrm{FE}} = \frac{1}{C_{ox}} \frac{L}{W} \left| \frac{\partial G}{\partial v_G} \right| \tag{59}$$

For the back-gating transfer characteristic shown in Figure 19, L/W = 10/50, C_{ox} of the 500 nm SiO_2 = 7 x 10^{-9} F/cm^2, and $|\partial G/\partial v_G| \approx 2.5 \times 10^{-6}$ A/V^2, then:

(Back-gating): $\mu_{FE} \approx 71$ cm^2/V·s. (60)

For the top-gating transfer characteristic shown in Figure 32, L/W = 10/50, C_{ox} of the 25 nm Al_2O_3 = 3.54 x 10^{-7} F/cm^2, and $|\partial G/\partial v_G| \approx 1.4 \times 10^{-4}$ A/V^2, then:

(Top-gating): $\mu_{FE} \approx 79$ cm^2/V·s. (61)

These numbers, while respectable, are much smaller than the 300 – 1500 cm^2/V·s, typically found in doped silicon, and are significantly less than the mobility of the CNT channel itself, which is on the order of 10^5 cm^2/V·s. While beyond the scope of this thesis, it may nevertheless be possible to achieve the intrinsic high mobility of the carbon nanotube into a transistor, if the Schottky barrier is minimized (e.g. replace with ohmic contacts)

5.6.2. Scanning gate microscopy

To investigate the local sensitivity of our CNTFETs, we used scanning gate microscopy [64]. Briefly the I_{DS} is monitored, while a biased tip, placed in close vertical proximity to the CNT, is raster-scanned. The data in Figure 37 shows that the CNTFET is only sensitive to tip-gating at certain locations.

The top panel in Figure 37 refers to the topography. The important features are the CNT, the string-like object in the middle, and the metal source contact at the bottom of each image. The particulate matter is due to contamination, which does not affect the electrical property of the device. The lower panel shows the scanning gate image and the outline of the sensitive area is added digitally to the topographic image. It is evident that the sensitive area is dependent upon the magnitude of the gate

voltage. Specifically, for ± 3.2 volts, the most sensitive area is centered relatively far from the source contact. This implies that lower tip gate voltages (0.5 V or less) will be affected in actual experiments mostly by charges closer to the contacts. This is an important finding since are limited in the voltage we can apply to our electrolyte solution before redox reactions start to erode the electrodes.

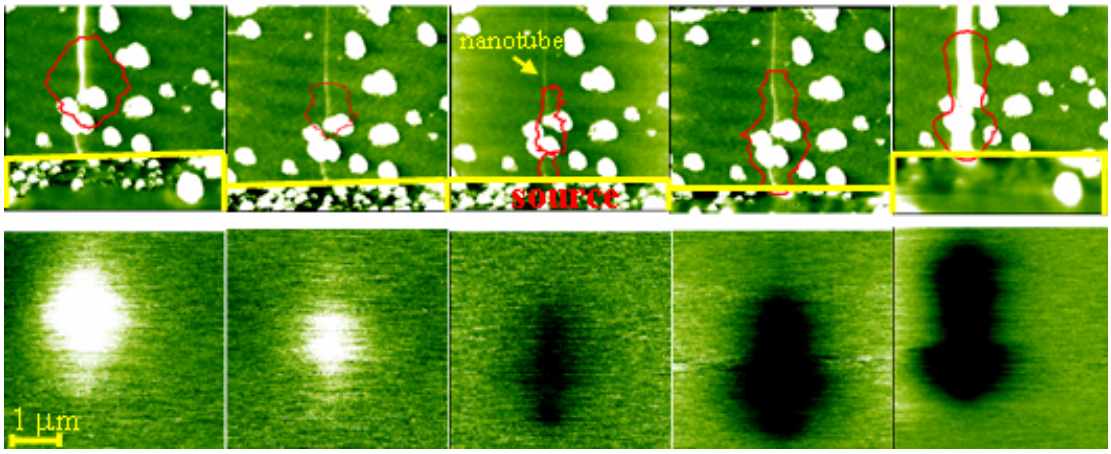

-3.2 V -1.6 V 0 V 1.6 V 3.2 V

Figure 37 Scanning gate microscopy of unprotected carbon nanotube transistor. The top images are topography images. The contrast in the bottom images represents the I_{DS} as a function of the tip position. The tip, which functions as the gate, was biased with the corresponding indicated voltages.

5.6.3. Measurement: data point acquisition

The threshold voltages (Figure 35) were obtained by fitting a parabolic curve around the minimum. The error associated with the threshold voltage is limited by the amount of voltage step. The voltage step is about 43 mV, therefore we can safely say that the error should not exceed one half of that value or 22 mV. Moreover, the curve is so smooth, which may be due to the averaging effect of the nanotube mats. In estimating the sensitivity in the titration curve (Figure 36), we are limited by the noise

from device to device variation, rather than the error in estimating individual threshold voltage.

Each I_{DS} datapoint was measured with a delay of 50 ms after the new V_{GS} was applied. The delay time was chosen such that the measured gate current, I_{GS}, was less than 1 nA. Ideally, there should be no gate current. A low I_{GS} is an indication that a steady state has been reached.

5.6.4. Gate dielectric consideration

It is well known that silicon oxide is particularly prone to alkali ion penetration. Aluminum oxide is known to offer better sodium resistance. However, if we insist in exposing the aluminum oxide to salt solution overnight, it also will eventually give way. Evidence for this effect is shown by the leftward threshold voltage shift in Figure 38 as expected for positive ion penetration for a sample exposed to salt overnight. The I_{DS} after salt exposure was much reduced, indicating that either the ions have reached the channel and act as scattering sources, or screen the applied gate source voltage, such that the field reaching the channel is reduced.

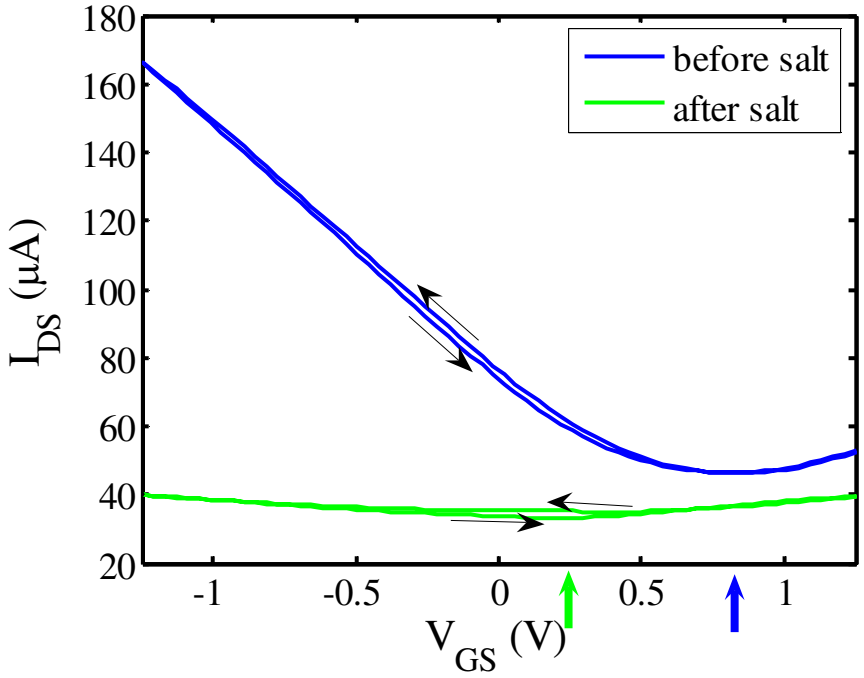

Figure 38 Transfer curve before (blue) and after (green) overnight salt exposure to aluminum oxide covered CNTFET. The threshold voltage positions indicated by the blue and green arrow clearly shifted to the left after positive ion penetration. Moreover the ions seem to either reach the channel to induce more scattering or screen the applied gate voltage.

5.6.5. DNA surface coverage

The probe DNA immobilized was 10 μM. We do not however have an independent means to estimate the surface density of the probe DNA. 10 μM is generally considered rather high concentration to achieve high density probe-DNA coverage. As described in 5.5, we can use the voltage shift and the capacitance of the electrolyte buffer to back-calculate the surface charge density added upon target DNA hybridization, i.e. 1.37 x 10^{-6} C/cm^2 or 1.4 x10^{11} molecules/cm^2 at 1 μM target hybridization, or equivalently, the average spacing between target DNA is 27 nm.

For an area of about 1 mm^2, the number of target DNA molecules bound to the surface is 1.4 x 10^9 molecules. A droplet of around 0.5 μL of 1μM target DNA contains 3 x 10^{12} molecules. It means that almost 1000× more molecules are actually floating in the solution, and far from reaching the limit that we completely deplete the target molecules in the solution.

The titration curve (Figure 36) looks as though a saturation was reached at 1 μM of target hybridization. While we do not know what the true probe DNA surface coverage is, it is very likely that the saturation is limited by the probe DNA coverage and steric hindrance, since it is well known that the hybridization efficiency would be reduced as the probe density is increased due to steric hindrance [65].

5.7. Future work

As mention in the introduction in Chapter 1, the goal of this project is to eventually develop an electronic device capable for testing dozens of genes with the sensitivity and specificity level comparable to the current fluorescent-based DNA microarray. With that in mind, we list several items to be accomplished along that line:

- To develop a more rigorous model to predict the hybridization signal and to compare the prediction with the actual experimental result.
- To attempt to improve the uniformity of the transistor characteristics or to come up with a clever scheme to calibrate the signals despite the transistors' non-uniformity

- To integrate the peripheral circuitry required for signal conditioning, calibration and multiplexing.
- To come up with a scheme such that the target DNA can be concentrated in the active area of the transistor
- To include a design of integrated system and fluidic channels to obviate manual pipetting, and to better control the liquid delivery of different type of genes.

Chapter 6: Other works on biosensors: gold nanoparticle colorimetry

In this chapter, I will discuss my other biosensing work on understanding thrombin aptamer binding using gold nanoparticle colorimetry. Gold nanoparticle colorimetry assay using aptamers is a low cost and a highly effective means for detecting a wide range of biomolecular targets. In this work, this technique is used to detect the protein thrombin as a model system for understanding the relationship between the aptamer-target binding properties and the optical colorimetric response as well as to gain insight on the secondary structures of the aptamers. Gold colorimetry technique itself has been demonstrated [66] and widely researched. The contribution of this work is in the understanding of the novel aptamer binding studied using gold colorimetry.

Aptamers are short artificial nucleic acid chains that bind to nucleosides, amino acids, peptides, viruses, drugs and even cells [63]. These molecules often exhibit secondary or higher order morphological structures which make them adhere to their targets with high specificity and affinity. The aptamers, or more precisely, the sequences that bind to a given target are found using a well established biochemical procedure known as SELEX (systematic evolution of ligands by exponential enrichment) [67]. Once the sequences are known, the preparation of the nucleic acid probe is straightforward and the protocols for immobilization are universal and

convenient. Indeed, it is expected that aptamers can rival antigens and antibodies in their use as targeting molecules in drug development and biosensing applications [68].

Hybrid systems, wherein an aptamer is tethered to a metallic nanoparticle, are effective, low cost and highly portable platforms for detecting biomolecules. In its simplest implementation [69-71], gold nanoparticles (GNPs) are functionalized with single stranded probe oligonucleotides and suspended in solution. A solution of well-dispersed GNPs exhibits a plasmon resonance absorption peak at the optical wavelength of 520 nm, which renders the solution reddish visible with the naked eye. Upon exposure of the probe to perfectly complementary single stranded DNAs, Watson-Crick base-pairing crosslinks the GNPs to form aggregates, and causes extinction of the absorption peak. The result is a clearly identifiable change in color. Thus far, a few target molecules including nucleic acids [70], nucleosides [72], small molecules [72], proteins [73] and metals [74], have been detected using clever variations of this principle. However, as more and more sequences are found and combined with the unprecedented ease by which aptamer probes can be prepared and used, it is only a matter of time before this system becomes a workhorse in biochemical detection.

In this work, we are interested in how aptamers detect proteins using colorimetry as an indicator. Specifically, we would like to understand how different aptamers of a given target protein behave during binding. Since, in general, multiple sequences may bind to a given target, this issue arises in all aptamer-GNP assays, and learning their characteristics is key in advancing this technique. As we shall see, the optical response is not the same for all aptamers but is highly dependent upon the number of available sites that a given aptamer can bind on. Similarly, systematic

substitution of single nucleotides can reveal interesting and potentially useful characteristics of the structure of the aptamer probes. These issues, along with experiments to establish the mechanism of color change and limits of detectable target concentration, are discussed in this paper.

Thrombin was chosen as the case model because of its ideal characteristics. It is a blood clotting factor that only has two known aptamer sequences, i.e. 15-mer BOCK [75] (5'-GGT TGG TGT GGT TGG-3'), and 29-mer TASSET [76] (5'-AGT CCG TGG TAG GGC AGG TTG GGG TGA CT-3'). There is abundant information on the interaction between thrombin and BOCK, the structure [77] of BOCK both in solution [78], and the BOCK-thrombin complex [79, 80]. The fibrinogen recognition exosites involved in binding [81, 82] are also known. The symmetrical structure of the BOCK relative to its center guanine (G) is also compelling.

6.1. Experiments

Colloidal gold, with a mean diameter of 10 nm and concentration of 5.7 x 10^{12} particles/mL or 9.5 nM, was purchased from Ted Pella (www.tedpella.com). The oligonucleotide sequences, all including an 18-carbon spacer and thiol modifier at the 5' terminus, were purchased from IDT (www.idtdna.com). Table 5 shows all oligonucleotide sequences used in this experiment and their corresponding names referred in this chapter.

Name	Sequence
BOCK	5'-GGT TGG TGT GGT TGG-3'

G1X	5'-TGT TGG TGT GGT TGG-3'
G2X	5'-GTT TGG TGT GGT TGG-3'
G8X	5'-GGT TGG TTT GGT TGG-3'
G15X	5'-GGT TGG TGT GGT TGT-3'
TASSET	5'-AGT CCG TGG TAG GGC AGG TTG GGG TGA CT -3'

Table 5 Oligonucleotide names and sequences. The underlined base is one base mistake away from otherwise correct BOCK sequence.

The oligonucleotide to gold particle conjugation is based on thiol-Au bonding. The as-purchased thiol modified oligonucleotides came in disulfide form which had to be cleaved using a reducing agent, DTT (dithiothreitol, purchased from Sigma-Aldrich, Prod. No. D9779). 10 μL of 1 mM thiol modified oligonucleotide was added to 1.54 mg of DTT in 10 mM phosphate buffer (PBS) pH 7 to make a 500 μL solution. DTT was removed prior to the conjugation by passing the solution through a gel filtration column (NAP-5, from Amersham Bioscience). Gold colloid was added to the oligonucleotide solution with the reduced disulfide. The mixture, containing 5 μM of thiol modified oligonucleotide and 4.75 nM of gold colloid, was held at 60 °C overnight to ensure optimum conjugation. To remove unconjugated oligonucleotides, the solution was centrifuged followed by removal of the supernatant, and redispersion of the gold-oligo conjugate in 10 mM PBS pH 7. The final concentrations of gold and oligonucleotide in the solution were 3.4 nM and 350 nM, respectively. The aptamer-conjugated gold-nanoparticle solution is stable for months, as far as no precipitation or any apparent color change was observed. The gold particles remained well-dispersed in the solution.

All thrombin concentrations for titration were prepared by resuspending the as-purchased lyophilized thrombin in 10 mM phosphate buffer solution at pH 7 to desired concentrations ranging from pM to μM. The thrombin solution was then mixed with the gold oligonucleotide conjugated solution without the addition of salt.

6.2. Results

All UV-Vis spectra were measured at room temperature using a Nanodrop™ ND-1000 spectrophotometer. The instrument has a path length of 1 mm, and is capable of scanning wavelengths ranging from 220 to 750 nm with 3 nm resolution, and measuring absorbance with 0.003 precision. It requires only 1-2 μL of sample volume per absorbance measurement.

All UV-Vis spectra are normalized against the spectrum of distilled water since water is the major solvent in all of the solutions used in this experiment. A typical UV-Vis spectrum of aptamer-GNP complex is shown in Figure 39. The surface plasmon resonance absorption of the gold nanoparticles is clearly evident from the curve and peaks at 520 nm. This absorption spectrum is responsible for the reddish color of the gold colloid. In addition, the weak peak at 260 nm corresponds to the absorption from nucleic acid bases. From the data, after appropriate curve fitting and subtraction of the spectrum from the gold absorption, we deduce the concentrations of the aptamers and the gold particles from the absorbance using the Beer-Lambert law,

$$Absorbance = Ecl \tag{62}$$

where E is molar extinction coefficient, c is molar concentration and l is path length. Given E_{BOCK} = 143300 $M^{-1}cm^{-1}$ and E_{gold} = 105614000 M^{-1} cm^{-1}, from the spec sheet, the aptamer and gold concentrations are 355 nM and 3.4 nM respectively. Assuming that the number of unbound oligo is negligible, we deduce that there are 104 aptamer molecules per gold particle. This is a somewhat high coverage, considering the diameter of the gold particle is only 10 nm, but is nevertheless consistent with the values in the literature [71].

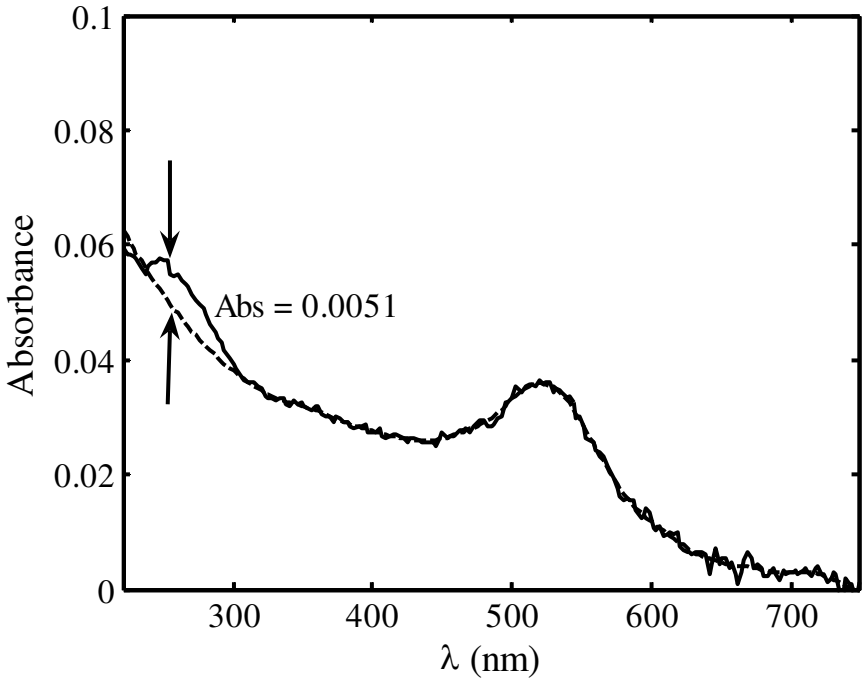

Figure 39 UV-Vis absorption spectrum of BOCK conjugated gold nanoparticle solutions. The peak around 520 nm is due to plasmon resonance absorption of the 10 nm gold nanoparticles, the peak around 260 nm is due to the absorption by the conjugated nucleic acid aptamers. The dashed line is a fitted curve to determine the 260 nm absorbance contributed by the nucleic acid aptamers.

6.2.1. Mechanism of resonance extinction

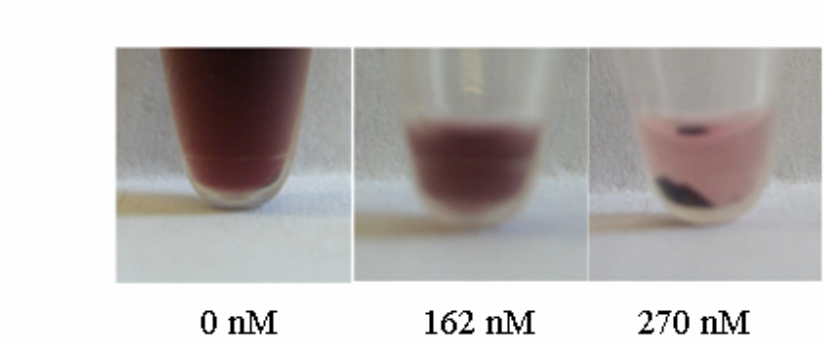

Figure 40 The color of BOCK conjugated gold nanoparticles with incremental addition of thrombin. The thrombin concentration is indicated by the label beneath each picture. The concentration of the gold nanoparticle is 20x more than that used in the rest of the aggregation assay, in order to emphasize the reddish color. The rightmost picture shows clear precipitation due to gold aggregation.

Figure 40 shows the appearance of the solution as a function of target concentration. The left vial contains only the BOCK-GNP complex. The GNPs are well dispersed so that each of them can be considered as a scatterer of size much smaller than the wavelength of the incident light. The collective electronic oscillation of the gold nanoparticles leads to very strong absorption signal, and renders the solution reddish/pink [83]. The middle and right vials show the result of adding thrombin. Note that the optical change does not exhibit a color change toward purple per se, but instead the transparency of the solution improves as thrombin is added. A quantitative measurement of this effect is summarized in Figure 41, where the UV-Vis spectra for increasing amounts of thrombin concentration are plotted. It is evident that increasing thrombin reduces the 520 nm absorbance peak but does not induce a shift in the absorbance peak. This is quite different from other colorimetry results [84],

which show absorption peak red shift. Thus, the mechanism of signal extinction in this case is different from the previous reports in which the color change attributed to the change in interparticle distance induced by binding [70]. Similarly, one can also rule out that binding profoundly changes the dielectric constant around the surrounding medium or the shell of the gold particle as this also produce red shift and broadening of absorption peak. The optical properties of a system of small metallic particles due to collective inter-particle interactions has been studied [85], and it was shown that increasing gold particles clustering broadens and suppresses the resonance absorption peak. We strongly suspect that the mechanism is that aptamer-thrombin

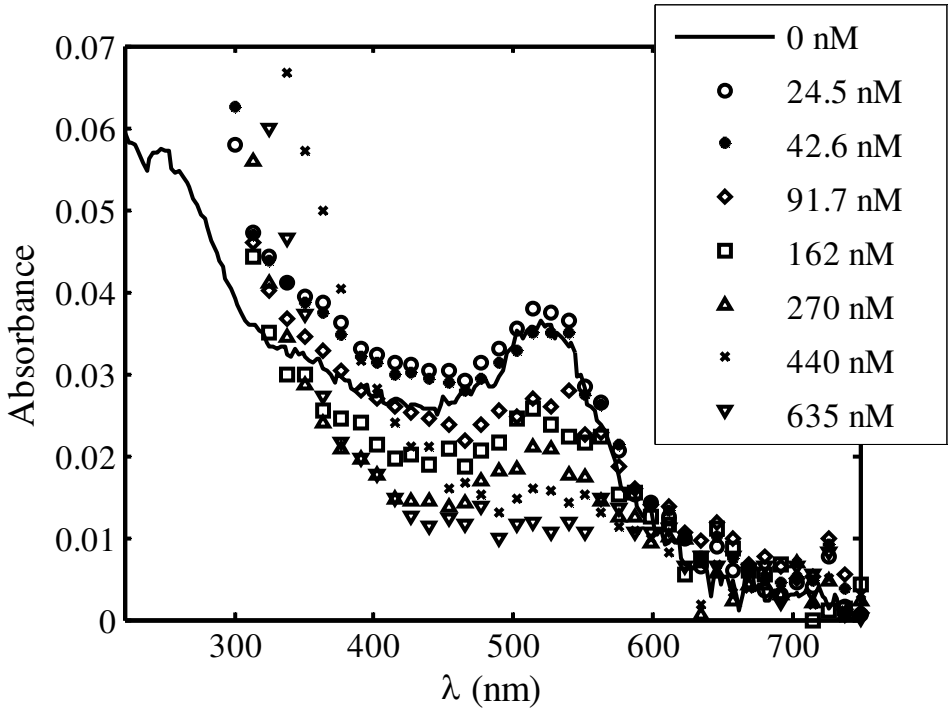

Figure 41 UV-Vis spectra of BOCK conjugated gold nanoparticles upon addition of thrombin. The added thrombin concentration is denoted in the legend. We observed that the 520 nm peak is gradually suppressed as more thrombin is added, without significant red shift in peak position.

binding causes the aggregation of the GNPs into large clusters which precipitate out of the solution and thereby reduce scattering. This conclusion is supported by the right vial in Figure 40, which shows the dark precipitates of GNP that formed by exposing the aptamer-GNP complex to a highly concentrated (270 nM) thrombin target.

6.2.2. Number of binding sites on thrombin for the specific aptamer

Having established that thrombin causes GNP aggregation, we will now explore the binding mechanisms leading to GNP aggregation. GNP clustering occurs because BOCK has more than one binding site on the thrombin. From the X-ray

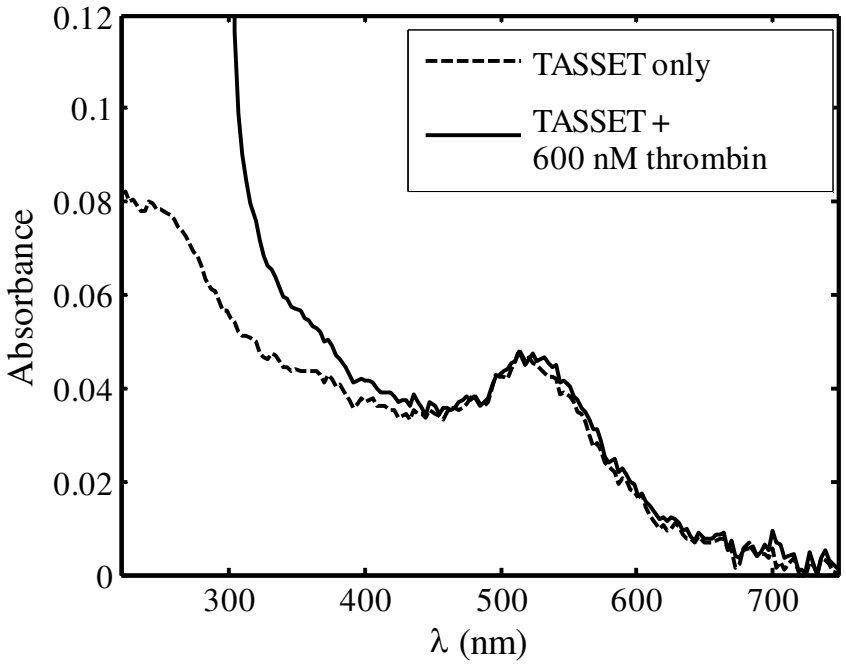

Figure 42 UV-Vis spectrum of TASSET conjugated gold nanoparticles and that with added thrombin. The 520 nm peak is not suppressed upon thrombin addition, indicating that gold particles do not aggregate.

crystallography studies of the BOCK-thrombin complex, Padmanabhan et al. [79, 80] showed that BOCK interacts with two distinct regions of the thrombin molecule, namely the fibrinogen exosite and the heparin binding site. These binding sites are almost at opposite ends of the molecule so that steric hindrance is not a factor. Hence, each thrombin links two aptamer-GNP complexes using both binding sites, which leads to GNP clustering.

We now compare the results using a second thrombin binding aptamer identified by Tasset et al. in 1997 [76]. Interestingly, while it was shown to exhibit a much higher (20 x – 50 x) binding affinity to thrombin than BOCK, it did not inhibit the clotting mechanism of thrombin. Figure 42 shows the UV-Vis spectra of this probe before and after addition of thrombin. Apart from the increase in absorption below 400 nm, it is clear that the plasmon absorption peaks of the TASSET-GNPs are not altered by the addition of thrombin, signifying that the GNP aggregation does not occur. The data suggests that there is only one accessible binding site for TASSET, which Tasset et al. [76] indicated to be the heparin binding exosite (exosite II). From a practical perspective, this result underscores an important cautionary consideration in colorimetric assays: the absence of color change in the assay is not a sufficient condition for the absence of the target molecule.

6.2.3. Secondary structure of BOCK aptamer

It is well known that the G-quadruplex secondary structure plays an important role for the aptamer-thrombin binding [77]. We want to understand the effect of single base alterations in BOCK on its secondary structure. We prepared oligo sequences similar to BOCK by substitution of a T in the G1, G2, G8 and G15 locations. We

point out that G1 is the guanine base closest to the 5' end which is tethered to the gold nanoparticle. The UV-Vis spectra shown in Figure 43 reveal that oligos with substitutions at the G1 and G2 locations showed the same GNP aggregation as the unmodified BOCK, whereas those with substitution at the center (G8) and the far end (G15) do not lead to aggregation.

Structural NMR [78] and X-ray [80] studies show that the BOCK forms two G-quadruplex planes linked by TGT loop and two TT loops unimolecularly. Wu et al. [81], and Padmanabhan et al. [80] suggested that the dominant interaction of BOCK with the fibrinogen recognition site of thrombin involves the TGT loop of the aptamer at the center of the sequence. And indeed we found that substituting a T in place of G8 destroys the TGT loop and hence it does not bind with the thrombin (Figure 43c)

Closer inspection of the BOCK sequence shows a beautiful symmetry about the central G8. In other words, the sequence to the right and left of the central guanine is symmetric. At first glance, one would suspect that substitution of G1 and G15 would have identical results in so far as the disruption of the G-quadruplex structure. But our results indicate that the G1 (and G2) substitution preserves the binding property whereas G15 does not.

We observed GNP aggregation in G1X and G2X (Figure 43 a, b). Because of the proximity to the nanoparticle, it is possible that bases 1 and 2 are inaccessible due to steric effects and do not participate in the binding event. We believe that the G-quadruplex structure must be retained even by BOCK variations G1X and G2X. Since G-quadruplex requires eight G's, which are not provided by a single molecule of G1X or G2X, we propose that the eight G's are contributed by two adjacent

molecules on the same GNP. This is consistent with the recent results by Fialová et al. [86], which suggest that the G-quadruplex is bimolecular, formed by two aptamer molecules, rather than unimolecular as previously reported by Macaya et al. [78].

We also invoke this bimolecular structure as a reason why substitution of the last guanine, G15, does not lead to GNP aggregation (Figure 43d). Apparently, the G-quadruplex formation is thwarted by a substitution of the last guanine (G15), because G15 participates in the bimolecular G-quadruplex. This implies that bases in the second half of the symmetric sequence (G10G11T12T13G14G15) are responsible for formation of a bimolecular G-quadruplex structure.

We note that since we observed no GNP aggregation in the absence of thrombin, we rule out the possibility that the bimolecular G-quadruplex is formed by two aptamer molecules on two different GNPs.

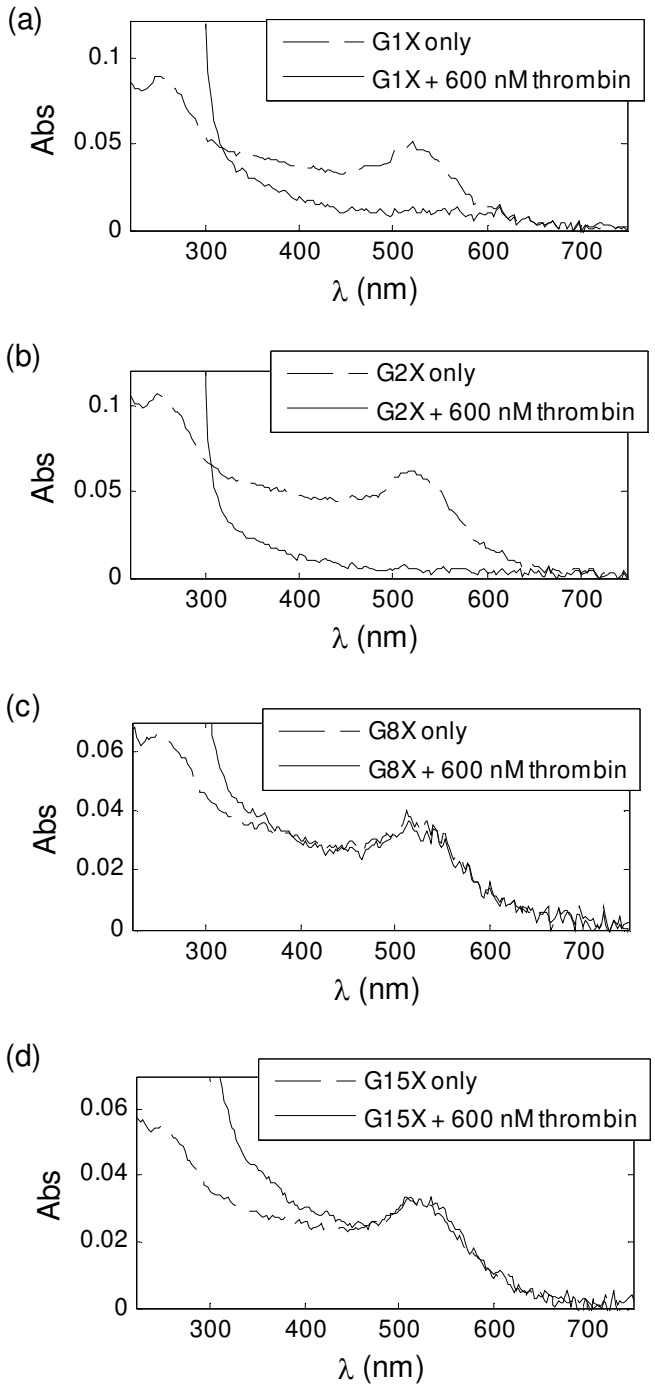

Figure 43 UV-Vis spectra of one base mistake sequences from BOCK, and those with added thrombin. Sequences with mistake located close to the gold nanoparticle behave as if they were correct BOCK sequence.

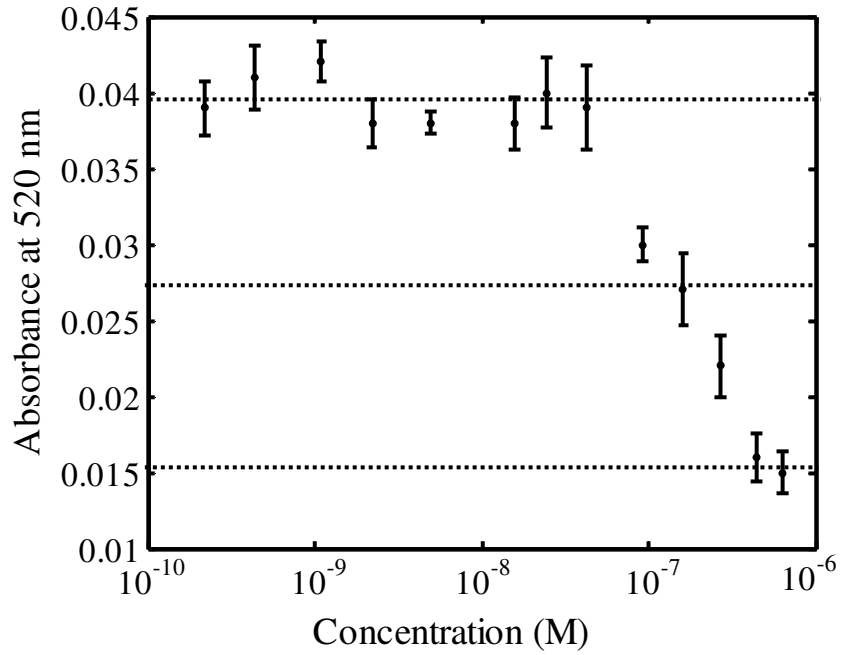

Figure 44 Absorbance at 520 nm of BOCK conjugated gold nanoparticle as a function of titrated thrombin concentration. An apparent K_d is extracted by looking up the needed thrombin concentration to suppress the absorbance half way between zero suppression and total suppression.

6.2.4. Thrombin titration

As mentioned before, Figure 41 shows the UV-Vis absorbance spectra for various concentration of thrombin added to the BOCK conjugated gold colloid. One feature shown in Figure 41 is that the absorbance in the UV region increased as more thrombin was added. This increase is attributed to the increase of general protein content in the sample, resulting in a large increase in the 280 nm absorbance. Unfortunately we cannot use this to determine the amount of added thrombin since a

large amount of bovine serum albumin (BSA), itself a protein, was added as stabilizer in the preparation of thrombin. The change in height of the 520 nm absorbance peak as a function of thrombin titration is plotted in Figure 44. The absorbance stayed more or less constant for low concentrations of thrombin, but started to drop at concentration >91.7 nM of thrombin. The data suggests that our GNP assay is sensitive to thrombin concentration down to about 90 nM.

Given the mechanisms for the observed color change, we can roughly correlate the color change to the concentration of bound thrombin to the aptamer conjugated GNPs. Obviously this correlation may not be as simple as linear, and its details should take into account detailed understanding of the kinetics of thrombin binding to aptamers, size distribution of the aggregates as a function of added thrombin concentration. In the framework of the mass action law in ligand binding, the dissociation constant, K_d, is the concentration of the ligand required to occupy 50% of the binding sites. We can derive an "apparent" K_d from the saturation-curve-like plot (Figure 44) of absorbance at 520 nm as the thrombin concentration that suppresses the absorbance halfway. Figure 44 yields an "apparent" K_d of 270 nM. The reported values of K_d are 75 to 100 nM. The mechanism to induce color change or gold aggregation is certainly more involved than the simple model of free ligand-receptor binding. It is then not so surprising that the apparent K_d is larger than the reported K_d, because there might be a portion of thrombin that binds to a BOCK, but fails to link to a second BOCK. We conclude that the smallest detectable thrombin concentration using GNP calorimetry without additional amplification as exemplified in [87] is about 100 nM.

6.3. Conclusions and future work

To realize a practical GNP-based sensor, it is important to form a thorough understanding of the effects of the various biomolecular interactions on the optical processes. Techniques that use antibody-fluorescent dye probes are much better understood, leading to their widespread adoption and commercialization. DNA-GNP complexes have yet to reach this level of maturity [88]. In this paper, we provided details for detecting thrombin using two distinct aptamer sequences. The binding is consistent with a model in which the GNP aggregates into very large clusters, which completely destroys the condition for plasmon resonance. The 15-mer BOCK, which is known to bind to both heparin and fibrinogen exosites of thrombin, serves to link individual GNPs, causing aggregation. In contrast, the 29-mer TASSET only binds to the heparin site of thrombin. Although the affinity is very strong, there is no mechanism to link the GNPs and the optical spectrum is unchanged. Similarly, our results suggest that the G-quadruplex secondary structure is formed by two BOCK aptamer molecules, and that the central TGT loop is essential in thrombin binding. Despite the symmetric structure, single base substitution of the last two bases farthest from the GNP appears to frustrate G-quartet formation and thus prevent binding; whereas the substitution on equivalent sites close to the GNP does not. Finally, using a low cost spectrometer, the detection limit for thrombin detection has been determined to be at the 100 nM concentration, which is sufficient for thrombin generation detection.

The understanding of aptamer-binding is important to evaluate the extensibility of the planar devices exemplified in Chapter 5 for detection of biomolecules other than nucleic acids. The aptamer may serve as the probe tethered on the device surface to capture certain target molecules. Future work includes the study of the feasibility of charge-based detection of non-nucleic acid biomolecules. Many proteins are ionized in different manners depending on the secondary structure and pH of the environment. That is why SDS is used in protein electrophoresis. While not impossible, charge-based detection of protein is clearly more complicated than DNA detection, and requires deeper research.

Chapter 7: Main conclusions

We have demonstrated label-free electronic DNA hybridization detection in the range of 10 – 100 nM using carbon nanotube field effect transistor arrays. The sensitivity is limited by the noise from device to device variations. However, the transfer characteristic curve of an individual transistor is very clean and smooth, which is very likely due to the averaging effect from the nanotube mats. The selectivity or specificity is limited by the surface chemistry.

The uniqueness of this work is the use of gate dielectric quality of atomic layer deposited-aluminum oxide to cover the carbon nanotube mats. While sensitivity is traded for selectivity, the aluminum oxide offers several extra benefits: small hysteresis in the transfer characteristic of the CNTFET compared to that of an unprotected CNTFET; recovery to the intrinsic ambipolar characteristic; and better resistance against sodium penetration compared to silicon oxide.

To further push down the sensitivity, so that this technique may compete with the current DNA microarray, we need (i) to improve the device to device variation or to develop a calibration scheme to overcome this non-uniformity, (ii) to improve the probe loading and hybridization efficiency through optimal surface chemistry, or perhaps (iii) to device a scheme to concentrate target DNAs towards the probe DNAs. We believe that we have laid down the foundation for the development of charge based biodetection using carbon nanotube field effect transistor.

In the second part, we demonstrated protein detection using gold colorimetry. While gold colorimetry is a well-know technique, the contribution of this work is in exploring the binding mechanism of the new class of biomolecules, namely aptamers. Aptamers, which exhibit certain secondary structure, offer a new extension of using nucleic acids to capture other specific non-nucleic acid target biomolecules. We imagine that protein detection in the CNTFET platform as demonstrated for DNA detection must be much more difficult and challenging, since the requirement of preserving the secondary structure presents more restriction to the dilution buffer being used.

List of Publications

1. H. Pandana, K. H. Aschenbach, D. R. Lenski, M. S. Fuhrer, J. Khan, and R. D. Gomez, ”A versatile biomolecular charge based sensor using oxide gated carbon nanotube transistor arrays”, *accepted for publication in IEEE Sensors Journal.* (October, 2007)

2. H. Pandana, K. H. Aschenbach, and R. D. Gomez, “Systematic aptamer-gold nanoparticle colorimetry for protein detection: thrombin”, *submitted to IEEE Sensors Journal.* (August 1, 2007)

3. H.Pandana, L. Gan, M. Dreyer, C. Krafft, and R. D. Gomez, “Magnetoresistance of ferromagnetic point junctions from tunneling to direct contact regimes”, *IEEE Transactions on Magnetics*, vol. 40, pp.2266-2268, July 2004.

4. M. Dreyer, H. Pandana, and R. D. Gomez, “Scanning tunneling spectroscopy of individual iron atoms on a permalloy surface”, *IEEE Transactions on Magnetics*, vol. 39, pp.3459-3461, Sep 2003.

Bibliography

1. Weaver R, F. Molecular biology. 3th ed. McGraw-Hill; 2004. .

2. Alberts B, Johnson A, Raff L, Martin, Roberts K, Walter P. Molecular biology of the cell. 4th ed. Garland Publishing; 2002. .

3. Pandana H, Gan L, Dreyer M, Krafft C, Gomez RD. Magnetoresistance of ferromagnetic point junctions from tunneling to direct contact regimes. Magnetics, IEEE Transactions on 2004;40(4):2266-8.

4. Dreyer M, Pandana H, Gomez RD. Scanning tunneling spectroscopy of individual iron atoms on a permalloy surface. Magnetics, IEEE Transactions on 2003;39(5):3459-61.

5. Bader D, E., Gray D. Evaluation of a sandwich gene probe assay for newcastle disease virus. ; 1996 February 1996. Report nr X5XD (X5XD).

6. Bally M, Halter M, Voros J, Grandin HM. Optical microarray biosensing techniques. Surf Interface Anal 2006 NOV;38(11):1442-58.

7. Epstein JR, Biran I, Walt DR. Fluorescence-based nucleic acid detection and microarrays. Anal Chim Acta 2002 SEP 26;469(1):3-36.

8. Fouque B, Schaack B, Obeid P, Combe S, Getin S, Barritault P, Chaton P, Chatelain F. Multiple wavelength fluorescence enhancement on glass substrates for biochip and cell analyses. Biosensors & Bioelectronics 0515;20(11):2335-40.

9. Schaferling M, Nagl S. Optical technologies for the read out and quality control of DNA and protein microarrays. Anal Bioanal Chem 2006 JUN;385(3):500-17.

10. Axelrod D. Total internal reflection fluorescence microscopy in cell biology. Traffic 2001 11;2(11):764-74.

11. Clegg RM, Holub O, Gohlke C. Fluorescence lifetime-resolved imaging: Measuring lifetimes in an image. Methods Enzymol 2003;360:509-42.

12. Rech I, Cova S, Restelli A, Ghioni M, Chiari M, Cretich M. Microchips and single-photon avalanche diodes for DNA separation with high sensitivity. Electrophoresis 2006;27(19):3797-804.

13. Ho HA, Dore K, Boissinot M, Bergeron MG, Tanguay RM, Boudreau D, Leclerc M. Direct molecular detection of nucleic acids by fluorescence signal amplification. J Am Chem Soc 2005;127(36):12673-6.

14. What is the sensitivity of the GeneChip® expression assay? [Internet]. Available from: http://www.affymetrix.com/support/help/faqs/ge_assays/faq_5.jsp.

15. Yu CJ, Wan Y, Yowanto H, Li J, Tao C, James MD, Tan CL, Blackburn GF, Meade TJ. Electronic detection of single-base mismatches in DNA with ferrocene-modified probes. J Am Chem Soc 2001;123(45):11155-61.

16. Patolsky F, Lichtenstein A, Willner I. Highly sensitive amplified electronic detection of DNA by biocatalyzed precipitation of an insoluble product onto electrodes. Chemistry - A European Journal 2003;9(5):1137-45.

17. Ozsoz M, Erdem A, Kerman K, Ozkan D, Tugrul B, Topcuoglu N, Ekren H, Taylan M. Electrochemical genosensor based on colloidal gold nanoparticles for the detection of factor V leiden mutation using disposable pencil graphite electrodes. Anal Chem 2003;75(9):2181-7.

18. Armistead PM, Thorp HH. Electrochemical detection of gene expression in tumor samples: Overexpression of rak nuclear tyrosine kinase. Bioconjugate Chem 2002;13(2):172-6.

19. Tlili C, Korri-Youssoufi H, Ponsonnet L, Martelet C, Jaffrezic-Renault N. Electrochemical impedance probing of DNA hybridisation on oligonucleotide-functionalised polypyrrole. Talanta 2005 11/15;68(1):131-7.

20. Gautier C, Cougnon C, Pilard J, Casse N. Label-free detection of DNA hybridization based on EIS investigation of conducting properties of functionalized polythiophene matrix. Journal of Electroanalytical Chemistry 2006 2/15;587(2):276-83.

21. Raether H. Surface plasma oscillations and their applications. In: Georg Hass, Maurice Francombe H., Richard Hoffman W., editors. Physics of thin films. Academic Press; 1977. .

22. Cheng D, K. Field and wave electromagnetics. 2nd ed. Addison-Wesley; 1989. .

23. Kittel C. Introduction to solid state physics. 7th ed. Wiley; 1996. .

24. Ruppin R. Surface polaritons of a left-handed medium. Physics Letters A 2000 11/13;277(1):61-4.

25. Homola J, Yee S, Gauglitz G. Surface plasmon resonance sensors: Review. Sensors and Actuators B: Chemical 1999 1/25;54(1-2):3-15.

26. Nelson BP, Grimsrud TE, Liles MR, Goodman RM, Corn RM. Surface plasmon resonance imaging measurements of DNA and RNA hybridization adsorption onto DNA microarrays. Anal Chem 2001;73(1):1-7.

27. Yao X, Li X, Toledo F, Zurita-Lopez C, Gutova M, Momand J, Zhou F. Sub-attomole oligonucleotide and p53 cDNA determinations via a high-resolution surface plasmon resonance combined with oligonucleotide-capped gold nanoparticle signal amplification. Analytical Biochemistry 2006 7/15;354(2):220-8.

28. Nabok A, Tsargorodskaya A, Davis F, Higson SJ. The study of genomic DNA adsorption and subsequent interactions using total internal reflection ellipsometry. Biosensors and Bioelectronics;In Press, Corrected Proof.

29. Brucherseifer M, Nagel M, Bolivar PH, Kurz H, Bosserhoff A, Buttner R. Label-free probing of the binding state of DNA by time-domain terahertz sensing. Appl Phys Lett 2000 DEC 11;77(24):4049-51.

30. Guiducci C, Stagni C, Zuccheri G, Bogliolo A, Benini L, Samorì B, Riccò B. DNA detection by integrable electronics. Biosensors and Bioelectronics 2004 3/15;19(8):781-7.

31. Sauerbrey G. Verwendung von schwingquarzen zur wagung dunner schichten und zur mikrowagung. Zeitschrift Fur Physik 1959;155(2):206-22.

32. O'Sullivan CK, Guilbault GG. Commercial quartz crystal microbalances-theory and applications. Biosensors & Bioelectronics 1201;14(8):663-70.

33. Storri S, Santoni T, Mascini M. A piezoelectric biosensor for DNA hybridisation detection. Anal Lett 1998;31(11):1795-808.

34. Hur Y, Han J, Seon J, Pak YE, Roh Y. Development of an SH-SAW sensor for the detection of DNA hybridization. Sens Actuator A-Phys 2005 MAY 17;120(2):462-7.

35. Bergveld P. Development, operation, and application of ion-sensitive field-effect transistor as a tool for electrophysiology. IEEE Trans Biomed Eng 1972;BM19(5):342,&.

36. Souteyrand E, Cloarec JP, Martin JR, Wilson C, Lawrence I, Mikkelsen S, Lawrence MF. Direct detection of the hybridization of synthetic homo-oligomer DNA sequences by field effect. J Phys Chem B 1997 APR 10;101(15):2980-5.

37. Estrela P, Migliorato P, Takiguchi H, Fukushima H, Nebashi S. Electrical detection of biomolecular interactions with metal-insulator-semiconductor diodes. Biosensors and Bioelectronics 2005 2/15;20(8):1580-6.

38. Pouthas F, Gentil C, Cote D, Zeck G, Straub B, Bockelmann U. Spatially resolved electronic detection of biopolymers. Phys Rev E 2004 SEP;70(3):031906.

39. Uslu F, Ingebrandt S, Mayer D, Böcker-Meffert S, Odenthal M, Offenhäusser A. Labelfree fully electronic nucleic acid detection system based on a field-effect transistor device. Biosensors and Bioelectronics 2004 7/15;19(12):1723-31.

40. Yan F, Estrela P, Mo Y, Migliorato P, Maeda H, Inoue S, Shimoda T. Polycrystalline silicon ion sensitive field effect transistors. Appl Phys Lett 2005 JAN 31;86(5):053901.

41. Bendriaa F, Le-Bihan F, Salaun AC, Mohammed-Brahim T, Tlili C, Jaffrezic N, Korri-Youssoufi H. DNA detection by suspended gate polysilicon thin film transisitor. Sensors, 2005 IEEE Conference Proceedings; 2005. .

42. Hahm J, Lieber CM. Direct ultrasensitive electrical detection of DNA and DNA sequence variations using nanowire nanosensors. Nano Lett 2004 JAN;4(1):51-4.

43. Star A, Tu E, Niemann J, Gabriel JCP, Joiner CS, Valcke C. Label-free detection of DNA hybridization using carbon nanotube network field-effect transistors. Proc Natl Acad Sci U S A 2006 JAN 24;103(4):921-6.

44. Meyyappan M, editor. Carbon nanotubes: Science and applications. CRC Press; 2004. .

45. Ashcroft N, W., Mermin D, N., editors. Solid state physics. 1st ed. Harcourt; 1976. .

46. Wallace PR. The band theory of graphite. Phys Rev 1947 05/01;71(9):622.

47. Frank S, Poncharal P, Wang ZL, Heer Wd. Carbon nanotube quantum resistors. Science 1998 June 12;280(5370):1744-6.

48. Dresselhaus MS, Dresselhaus G, Saito R. Carbon fibers based on C_{60} and their symmetry. Phys Rev B 1992 03/15;45(11):6234.

49. Ouyang M, Huang J, Cheung C, Lieber C. Energy gaps in "metallic" single-walled carbon nanotubes. Science 2001 April 27;292(5517):702-5.

50. Wilder JWG, Venema LC, Rinzler AG, Smalley RE, Dekker C. Electronic structure of atomically resolved carbon nanotubes. Nature 1998 01/01;391(6662):59-62.

51. Datta S. Quantum transport: Atom to transistor. Cambridge University Press; 2005. .

52. Bethune DS, Kiang CH, Devries MS, Gorman G, Savoy R, Vazquez J, Beyers R. Cobalt-catalyzed growth of carbon nanotubes with single-atomic-layerwalls. Nature 1993 JUN 17;363(6430):605-7.

53. Thess A, Lee R, Nikolaev P, Dai HJ, Petit P, Robert J, Xu CH, Lee YH, Kim SG, Rinzler AG, Colbert DT, Scuseria GE, Tomanek D, Fischer JE, Smalley RE. Crystalline ropes of metallic carbon nanotubes. Science 1996 JUL 26;273(5274):483-7.

54. Cassell AM, Raymakers JA, Kong J, Dai HJ. Large scale CVD synthesis of single-walled carbon nanotubes. J Phys Chem B 1999 AUG 5;103(31):6484-92.

55. Avouris P, Appenzeller J, Martel R, Wind SJ. Carbon nanotube electronics. Proceedings of the IEEE 2003;91(11):1772-84.

56. Appenzeller J, Knoch J, Derycke V, Martel R, Wind S, Avouris P. Field-modulated carrier transport in carbon nanotube transistors. Phys Rev Lett 2002 08/29;89(12):126801.

57. Fuhrer MS, Kim BM, Durkop T, Brintlinger T. High-mobility nanotube transistor memory. Nano Lett 2002;2(7):755-9.

58. Durkop T, Getty SA, Cobas E, Fuhrer MS. Extraordinary mobility in semiconducting carbon nanotubes. Nano Lett 2004;4(1):35-9.

59. Appenzeller J, Knoch J, Martel R, Derycke V, Wind SJ, Avouris P. Carbon nanotube electronics. Nanotechnology, IEEE Transactions on 2002;1(4):184-9.

60. Léonard F, Tersoff J. Novel length scales in nanotube devices. Phys Rev Lett 1999 12/13;83(24):5174.

61. Jhi S, Louie SG, Cohen ML. Electronic properties of oxidized carbon nanotubes. Phys Rev Lett 2000 08/21;85(8):1710.

62. Kim W, Javey A, Vermesh O, Wang Q, Li Y, Dai H. Hysteresis caused by water molecules in carbon nanotube field-effect transistors. Nano Lett 2003;3(2):193-8.

63. Ellington AD, Szostak JW. Invitro selection of rna molecules that bind specific ligands. Nature 1990 AUG 30;346(6287):818-22.

64. Bachtold A, Fuhrer MS, Plyasunov S, Forero M, Anderson EH, Zettl A, McEuen PL. Scanned probe microscopy of electronic transport in carbon nanotubes. Phys Rev Lett 2000 06/26;84(26):6082.

65. Peterson AW, Heaton RJ, Georgiadis RM. The effect of surface probe density on DNA hybridization. Nucl Acids Res 2001 12/15;29(24):5163-8.

66. Elghanian R, Storhoff JJ, Mucic RC, Letsinger RL, Mirkin CA. Selective colorimetric detection of polynucleotides based on the distance-dependent optical properties of gold nanoparticles. Science 1997 AUG 22;277(5329):1078-81.

67. Tuerk C, Gold L. Systematic evolution of ligands by exponential enrichment - rna ligands to bacteriophage-T4 dna-polymerase. Science 1990 AUG 3;249(4968):505-10.

68. Jayasena SD. Aptamers: An emerging class of molecules that rival antibodies in diagnostics. Clin Chem 1999 SEP;45(9):1628-50.

69. Sonnichsen C, Reinhard BM, Liphardt J, Alivisatos AP. A molecular ruler based on plasmon coupling of single gold and silver nanoparticles. Nat Biotechnol 2005 JUN;23(6):741-5.

70. Elghanian R, Storhoff JJ, Mucic RC, Letsinger RL, Mirkin CA. Selective colorimetric detection of polynucleotides based on the distance-dependent optical properties of gold nanoparticles. Science 1997 AUG 22;277(5329):1078-81.

71. Sato K, Hosokawa K, Maeda M. Rapid aggregation of gold nanoparticles induced by non-cross-linking DNA hybridization. J Am Chem Soc 2003 JUL 9;125(27):8102-3.

72. Liu JW, Lu Y. Fast colorimetric sensing of adenosine and cocaine based on a general sensor design involving aptamers and nanoparticles. Angewandte Chemie-International Edition 2006;45(1):90-4.

73. Yamamoto R, Katahira M, Nishikawa S, Baba T, Taira K, Kumar PKR. A novel RNA motif that binds efficiently and specifically to the tat protein of HIV and inhibits the trans-activation by tat of transcription in vitro and in vivo. Genes Cells 2000 MAY;5(5):371-88.

74. Kim YJ, Johnson RC, Hupp JT. Gold nanoparticle-based sensing of "spectroscopically silent" heavy metal ions. Nano Letters 2001 APR;1(4):165-7.

75. Bock LC, Griffin LC, Latham JA, Vermaas EH, Toole JJ. Selection of single-stranded-dna molecules that bind and inhibit human thrombin. Nature 1992 FEB 6;355(6360):564-6.

76. Tasset DM, Kubik MF, Steiner W. Oligonucleotide inhibitors of human thrombin that bind distinct epitopes. J Mol Biol 1997 OCT 10;272(5):688-98.

77. Wang KY, Mccurdy S, Shea RG, Swaminathan S, Bolton PH. A dna aptamer which binds to and inhibits thrombin exhibits a new structural motif for dna. Biochemistry (N Y) 1993 MAR 2;32(8):1899-904.

78. Macaya RF, Schultze P, Smith FW, Roe JA, Feigon J. Thrombin-binding dna aptamer forms a unimolecular quadruplex structure in solution. Proc Natl Acad Sci U S A 1993 APR 15;90(8):3745-9.

79. Padmanabhan K, Padmanabhan KP, Ferrara JD, Sadler JE, Tulinsky A. The structure of alpha-thrombin inhibited by a 15-mer single-stranded-dna aptamer. J Biol Chem 1993 AUG 25;268(24):17651-4.

80. Padmanabhan K, Tulinsky A. An ambiguous structure of a DNA 15-mer thrombin complex. Acta Crystallogr Sect D-Biol Crystallogr 1996 MAR 1;52:272-82.

81. Wu QY, Tsiang M, Sadler JE. Localization of the single-stranded-dna binding-site in the thrombin anion-binding exosite. J Biol Chem 1992 DEC 5;267(34):24408-12.

82. Paborsky LR, Mccurdy SN, Griffin LC, Toole JJ, Leung LLK. The single-stranded-dna aptamer-binding site of human thrombin. J Biol Chem 1993 OCT 5;268(28):20808-11.

83. Kreibig U, Genzel L. Optical-absorption of small metallic particles. Surf Sci 1985;156(JUN):678-700.

84. Storhoff JJ, Lazarides AA, Mucic RC, Mirkin CA, Letsinger RL, Schatz GC. What controls the optical properties of DNA-linked gold nanoparticle assemblies? J Am Chem Soc 2000 MAY 17;122(19):4640-50.

85. Kreibig U, Quinten M, Schoenauer D. Optical-properties of many-particle systems. Phys Scripta 1986;T13:84-92.

86. Fialova M, Kypr J, Vorlickova M. The thrombin binding aptamer GGTTGGTGTGGTTGG forms a bimolecular guanine tetraplex. Biochem Biophys Res Commun 2006 MAY 26;344(1):50-4.

87. Pavlov V, Xiao Y, Shlyahovsky B, Willner I. Aptamer-functionalized au nanoparticles for the amplified optical detection of thrombin. J Am Chem Soc 2004 SEP 29;126(38):11768-9.

88. Sato K, Hosokawa K, Maeda M. Colorimetric biosensors based on DNA-nanoparticle conjugates. Analytical Sciences 2007 JAN;23(1):17-20.